Investigation of a Micromachined Electric Field Mill to Maximize the Electrostatic Field Sensitivity

By Yu Zhou

A THESIS SUBMITTED TO THE FACULTY OF GRADUATE STUDIES OF
THE UNIVERSITY OF MANITOBA
IN PARTIAL FULFILLMENT OF THE REQUIREMENTS FOR THE DEGREE OF
MASTER OF SCIENCE

Department of Electrical and Computer Engineering
University of Manitoba
Winnipeg, Manitoba

© Copyright by Yu Zhou, 2012

for my parents

and

for those who guide me

Abstract

This thesis includes the modification and optimization to an electric field mill based on micromachining technology. The sensor was originally designed to overcome the disadvantages of the conventional macroscopic field mill. Although it achieved all these listed above with a minimum detectable field strength at 42 V/m, some drawbacks are yet to be settled. In order to overcome these drawbacks, modifications are studied and put forward. Metal coating of the sensor surface could lead to a good electrical grounding that addresses the charging problem. Non-resonant working design was established with a shutter displacement around 5μm. Finite element simulations were set up to look into the optimizations of the structure parameters of the sensor, focusing on the shutter and electrodes. Moreover, the fabrication process was also studied with attempts of each step carried out in the NSFL of University of Manitoba.

Acknowledgements

First and foremost, I would like to thank my advisor, Dr. Cyrus Shafai, for his support, patience and trust in me. Without his guidance, I would not be able to find a right path through all these years of study and research. Without his motivation, I might not be courageous enough to overcome difficulties encountered in the research. I really appreciate all the help that he provided and enjoy the time being his student.

I would also like to thank Dwayne Chrusch from Department of Electrical and Computer Engineering, University of Manitoba for his patience and care. Details and training of running the NSFL that he provided with turned out to be really important for the project that I was working on. Besides, his experiences on practical fabrication process did aid us a lot and I really appreciate that.

I wish to express my gratitude to Dr. Joe LoVetri for his suggestions and advices on the electromagnetic analysis of the project and set-up of the simulations. Thanks to the discuss with him, I could have a clear view of how the sensor works in terms of electrically and better understanding of the theory that involved in the project.

I learned quite a bit from my group mate Mark Roy. His knowledge in coding, electric circuits and software benefited me greatly. He played an important role in the project and would usually give me a hand when I faced any problems. Moreover, the way he works stimulated me so much and changed my understanding of being a graduate student.

I am thankful to Amy Dario from the Department of Electrical and Computer Engineering for patient help from her either academic or nonacademic. That really made my life on campus much easier as an international student.

I should also give my special thanks to Dr. Jason Zhu and Mrs. Jenny Zhou for their patience and care. It would be hard for me to establish my life here without their guidance and support.

I would like to thank all my friends in Canada for they really made everyday more colorful.

The guidance, encouragement and support from my parents are always what I cherished. Their love has always been my greatest motivation to do my best no matter where I am. I hope that one day I could be the one they could both be proud of and rely on.

Table of Contents

Abstract i

Acknowledgements ii

Table of Contents iv

Table of Figures vi

List of Tables ix

Chapter 1 Introduction 1

1.1 Electric Field Measurement 1
1.2 DC Electric Field Measurement 2
1.3 Micromachined Field Mill Sensors 4
1.4 Document Layout 5

Chapter 2 Electric Field Measuring Technology 6

2.1 The Electro-Optic Meter 6
2.2 The Free-Body Meter [27] 8
The Working Principle of the Free-Body Meter: 8
Free-Body Meter Example: 10
2.3 The Ground Reference Meter 10
2.3.1 Ground Reference Meter Example 12
2.4 Electric Field Mill 13
2.5 E-field measurement based on Lyman-α radiation of metastable hydrogen beam: 15
2.6 Micromachined Electric Field Sensors 16
Micromachined E-field sensor using electrostatic force: 18
2.7 Comparison of different techniques 19

Chapter 3 Sensor Design and Fabrication 21

3.1 Conventional MEFM 21
3.1.1 Fabrication of the Sensor 22
3.2 In- House Fabrication Process 24
3.2.1 Lithography 24
3.2.2 Plasma Etching 26

Chapter 4 Simulation Settings 39

4.1 Optimization of the Shutter Structure 39
4.2 Simulation 41
4.2.1 3-D Simulations Set-up 42
4.2.2 Results of 3-D simulations 47
4.2.3 Difficulties of 3-D simulations 49
4.2.4 2-D Simulation 50

4.2.5 2-D Simulation Set-up 52
4.2.6 Simulation parameters 56
4.2.7 2-D Results 61

Chapter 5 2-D Result Analysis 62

5.1 Grounded Shutter Design 62
5.2 Floating Shutter Design 69
5.3 Trapezoidal Shutter Cross-section 77
5.3.1 Design with Electrically Grounded Shutter 77
5.3.2 Floating shutter design with Trapezoidal Shutter Cross-section 91
5.4 Parameter Comparison 103
5.4.1 Width of Slit (S_w) 103
5.4.2 Electrodes Width (E_w) 104
5.4.3 Shutter Thickness (t_s) 106
5.4.4 Gap between Shutter and Electrodes (G) 107
5.5 Guard Ring 108
5.5.1 Grounded Shutter Design with Rectangular Shutter Cross-section 108
5.5.2 Grounded Shutter Design with Trapezoidal Cross-section 110
5.5.3 Floating Shutter Design with Rectangular Cross-section 112
5.5.4 Floating Shutter Design with Trapezoidal Cross-section 113
5.5.5 Comparing between different designs 114
5.6 Conclusion from the Simulation Results 114

Chapter 6 Fabrication through PolyMUMPs Process 116

6.1 PolyMUMPs Fabrication Process 118
6.2 Motion test of the fabricated sensors 120
6.2.1 Reason of reduced horizontal displacement 125
6.3 Summary 131

Chapter 7 Conclusion 132

7.1 What has been done 132
7.2 Future Work 135

References 136

Appendix A: Code of COMSOL with MATLAB Interface 143

Appendix B: Plasma Etch Attempts 163

Appendix C: Measurements of Motion Test on Sensors Fabricated Through PolyMUMPs 164

Table of Figures

Figure 1.1. Typical structure of a field mill. 3
Figure 1.2. Micromachined sensor fabricated by Wijeweera [20] 4

Figure 2.1. An Example of Electro-Optic sensor system [30]. 7
Figure 2.2. Working principle of the Free-Body Meter. 9
Figure 2.3. An example of a Free-Body Meter [32]. 10
Figure 2.4. Schematic view of a ground reference sensor. 11
Figure 2.5. A snapshot of the ground reference sensor designed by Charles J. Miller [33]. 12
Figure 2.6. Field mill with its electronic circuit 13
Figure 2.7 (a). Field mill with compensation for rotor voltage; (b). Field mill with constant-capacitance rotor. [34] 14
Figure 2.8. MEFM with thermal actuator [24]. 17
Figure 2.9. MEFM with comb drive and comb-shaped electrodes 18
Figure 2.10. Schematic view of sensor developed by A. Roncin et al. [40]. 19

Figure 3.1. MicraGEM fabrication process 23
Figure 3.2. Demonstration of resist spinning. 24
Figure 3.3. Results of the lithography 26
Figure 3.4. Examples of non-anisotropic etching. 27
Figure 3.5. Schematic view of the SF_6 /O_2 /CHF_3 etch. 28
Figure 3.6. Schematic of how surface turns to black. 31
Figure 3.7. Effect of adding CHF_3 into the etchant. 33
Figure 3.8. Illustration of the profile after etching 35
Figure 3.9. Anisotropy against flow rate of CHF_3 for 36

Figure 4.1. The MEFM fabricated by Wijeweera [20] and its cross-section. 40
Figure 4.2. Air Chamber. 43
Figure 4.3. Structure with artificial air chamber on the top. 44
Figure 4.4. Shutter in 3-D simulation. 45
Figure 4.5. Electrodes beneath the shutter. 46
Figure 4.6. High mesh density area. 47
Figure 4.7. Results of 3-D simulations and the results from Chao et al. [54] 49
Figure 4.8. Results of 2-D and 3-D simulations. 51
Figure 4.9. Chamber where the sensor was placed. 52
Figure 4.10. Chamber filled with artificial air. 53
Figure 4.11. Shutter with rectangular cross-section 53
Figure 4.12. Electrodes 54
Figure 4.13. Pyrex substrate 55
Figure 4.14. Large mesh density area. 55
Figure 4.15. Number of slits vs. simulation time. 56

Figure 4.16. Field strength beneath the shutter. 57
Figure 4.17. Time of each simulation vs. mesh density 59
Figure 4.18. Induced charge on the electrodes vs. mesh density. 59

Figure 5.1. Effects of width of slit. E_w = 4 µm, t_s = 4 µm, G = 4 µm. (Grounded shutter design with a rectangular cross-section) 63
Figure 5.2. Effects of electrodes width on induced charge. S_w = 6 µm, t_s = 4 µm, G = 4 µm. (Grounded shutter design with a rectangular cross-section) 64
Figure 5.3. Shutter thickness vs. induced charge. S_w = 6 µm, E_w = 4 µm, G = 4 µm. (Grounded shutter design with a rectangular cross-section) 66
Figure 5.4. Gap vs. induced charge. S_w = 6 µm, E_w = 4 µm, t_s = 4 µm. (Grounded shutter design with a rectangular cross-section) 68
Figure 5.5. Schematic view of the floating shutter design. 69
Figure 5.6. Width of slit vs. induced charge. E_w = 4 µm, t_s = 4 µm, G = 4 µm. (Floating shutter design with a rectangular cross-section) 71
Figure 5.7. Width of electrode vs. induced charge. S_w = 6 µm, t_s = 4 µm, G = 4 µm. (Floating shutter design with a rectangular cross-section) 73
Figure 5.8. Shutter thickness vs. induced charge. S_w = 6 µm, E_w = 4 µm, G = 4 µm. (Floating shutter design with a rectangular cross-section) 74
Figure 5.9. Gap vs. induced charge. S_w = 6 µm, E_w = 4 µm, t_s = 4 µm. (Floating shutter design with a rectangular cross-section) 76
Figure 5.10. Schematic view of the trapezoidal shutter cross-section. 77
Figure 5.11. Width of slit vs. induced charge, A equals 0.8. E_w = 4 µm, t_s = 4 µm, G = 4 µm. (Grounded shutter design with a trapezoidal cross-section) 79
Figure 5.12. Width of slit vs. induced charge, A equals 0.6. E_w = 4 µm, t_s = 4 µm, G = 4 µm. (Grounded shutter design with a trapezoidal cross-section) 80
Figure 5.13. Electrodes width vs. induced charge, A equals 0.8. S_w = 4 µm, t_s = 4 µm, G = 4 µm. (Grounded shutter design with a trapezoidal cross-section) 82
Figure 5.14. Electrodes width vs. induced charge, A equals 0.6. S_w = 4 µm, t_s = 4 µm, G = 4 µm. (Grounded shutter design with a trapezoidal cross-section) 83
Figure 5.15. Shutter thickness vs. induced charge, A equals 0.8. S_w = 4 µm, E_w = 4 µm, G = 4 µm. (Grounded shutter design with a trapezoidal cross-section) 85
Figure 5.16. Shutter thickness vs. induced charge, A equals 0.6. S_w = 4 µm, E_w = 4 µm, G = 4 µm. (Grounded shutter design with a trapezoidal cross-section) 86
Figure 5.17. Gap vs. induced charge, A equals 0.8. S_w = 4 µm, E_w = 4 µm, t_s = 4 µm. (Grounded shutter design with a trapezoidal cross-section) 87
Figure 5.18. Gap vs. induced charge, A equals 0.6. S_w = 4 µm, E_w = 4 µm, t_s = 4 µm. (Grounded shutter design with a trapezoidal cross-section) 89
Figure 5.19 Guessing of the reason of the abnormal result of close gap with trapezoidal shutter cross-section (a) Gap is small; (b) Gap is large 90
Figure 5.20. Width of slit vs. induced charge, A equals 0.8. E_w = 4 µm, t_s = 4 µm, t_s = 4 µm. (Floating shutter design with trapezoidal cross-section) 92
Figure 5.21. Width of slit vs. induced charge, A equals 0.6. E_w = 4 µm, t_s = 4 µm, t_s = 4 µm. (Floating shutter design with trapezoidal cross-section) 93
Figure 5.22. Electrode width vs. induced charge, A equals 0.8. S_w = 6 µm, t_s = 4 µm, t_s = 4 µm. (Floating shutter design with trapezoidal cross-section) 95

Figure 5.23. Electrode width vs. induced charge, A equals 0.6. S_w = 6 μm, t_s = 4 μm, t_s = 4 μm. (Floating shutter design with trapezoidal cross-section) 96
Figure 5.24. Shutter thickness vs. induced charge, A equals 0.8. S_w = 6 μm, E_w = 4 μm, G = 4 μm. (Floating shutter design with trapezoidal cross-section)............................ 98
Figure 5.25. Shutter thickness vs. induced charge, A equals 0.6. S_w = 6 μm, E_w = 4 μm, G = 4 μm. (Floating shutter design with trapezoidal cross-section)............................ 99
Figure 5.26. Gap vs. induced charge, A equals 0.8. S_w = 6 μm, E_w = 4 μm, t_s = 4 μm. (Floating shutter design with trapezoidal cross-section) 101
Figure 5.27. Gap vs. induced charge, A equals 0.6. S_w = 6 μm, E_w = 4 μm, t_s = 4 μm. (Floating shutter design with trapezoidal cross-section) 102
Figure 5.28. Results of different designs in terms of width of slit................................ 104
Figure 5.29. Result of different designs in terms of electrode width............................. 105
Figure 5.30. Results of different designs in terms of shutter thickness. 106
Figure 5.31. Results of different designs in terms of gap. 107
Figure 5.32. Schematic of guard ring... 108
Figure 5.33. Guard ring on grounded shutter design with rectangular cross-section. 110
Figure 5.34. Guard ring on electrically grounded shutter design with trapezoidal cross-section. 111
Figure 5.35. Guard ring on floating shutter design with rectangular cross-section........ 112
Figure 5.36. Guard ring on floating shutter design with trapezoidal cross-section. 113
Figure 5.37. Comparing of different designs with guard ring. 114

Figure 6.1. Microscopic view of the part of the sensor 117
Figure 6.2. Microscopic view of the fabricated sensors 117
Figure 6.3. PolyMUMPs fabrication process.. 120
Figure 6.4. (a) Testing chamber. (b) Sensor with package. (c) Fixture. (d) Circuit. 121
Figure 6.5.Working principle of the optical interferometer.. 122
Figure 6.6. Result of the motion test on shutter and connecting beam (a) with actuator unbiased; (b) with actuator biased. 123
Figure 6.7. 3-D view of the shutter structure. (a) with actuator unbiased. (b) with actuator biased. 124
Figure 6.8. Result of the motion test on the thermal actuator. (a) when not biased. (b) when 0.7 V dc voltage applied.. 125
Figure 6.9. 3-D view of the actuator (a) not biased. (b) biased. 126
Figure 6.10. Displacement of the thermal actuator from simulations. (a) when unbiased. (b) when biased.. 127
Figure 6.11. Suspension of the sensor. (a) Lever system with actuator unbiased. (b) Lever system with actuator biased. (c) Springs with actuator unbiased. (d) Springs with actuator biased. 128
Figure 6.12. Structure of the actuator and lever under microscope. (a) before testing. (b) after testing.. 130

List of Tables

Table 2-1. Comparison of different e-field measurement technology. 20
Table 3-1. Etching experiments. 34
Table 4-1. Definition of the MEFM design parameters and the simulated range of each parameters. 41
Table 4-2. Correspondence of parameters. 48
Table 4-3. Mesh density and difference in the amount of induced charge 60
Table 4-4. Refine rate and difference in the amount of induced charge. 61
Table 5-1. Conclusion from the results of simulations. 115
Table 6-1. Main structure parameters of the new design and the original design 116
Table 7-1. Plasma etch recipe and result 132

Chapter 1 Introduction

1.1 Electric Field Measurement

Electric field measurement is employed in various industries, using various technologies. In the area of power systems, electric field measurement is involved in several sub-domains such as the monitoring of transmission lines [1], detection and diagnosis of faulty suspension insulators [2,3,4] and the monitoring HVDC transformers [5]. All of them are critical to the function of modern power systems. An appropriate and effective measurement technology would reduce the cost by predicting system failure, and potentially save lives as well.

Electric field measurement technology is also applied in the detection and control of electrostatics [6,7,8]. The main purpose is to prevent uncontrolled electrostatic discharge. Research has shown that uncontrolled electrostatic charge could cause ignition if some specific conditions are met [9,10], especially in cases of storage and transportation of flammable material. Measuring the electric field generated by accumulated charges could indicate when a controlled discharged should be carried out, therefore reducing the possibility of ignition.

Another important utilization happens in the area of medical and biological science. The working principle of the electrocardiography (ECG) measurement is basically a measurement of the changing electric field generated by the heart beat [11]. More recently, electric field measurement technology has been used to investigate the biological effect of high voltage transmission lines on humans [12]. Research suggests a possible association among brain cancer and other diseases and exposure to extremely low-frequency electric fields [13,14,15]. Furthermore, health criteria for exposure to extremely low-frequency electric fields have also been published by the World Health Organization (WHO) [16] to attract the public attention to this issue.

Electric field measurement technologies are also useful tools for atmospheric science. Sensors employing different techniques are used to record, study and predict weather phenomena. According to the studies [17,18,19], daily weather phenomena, especially the incidents of lightning and thunderstorms, may cause an alternation in charge distribution in the atmosphere and therefore a gradient in electrical potential is generated. By measuring the change of the electric field above the ground, weather phenomena could be tracked and predicted. For example, the prediction of thunderstorm can save billions dollars all around the world [19].

1.2 DC Electric Field Measurement

Electric field measurement technology could be categorized by whether it is an ac or dc field that is being measured. While ac electric field measurement is comparatively easy, dc electric field measurement is complicated because of no cyclic variation with respect to time. As a result, the solution requires either employing sensors that do not rely the cyclic variation of the field strength, such as electro-optical sensors; or elaborately generate an alternating field whose amplitude corresponds to the incident dc field strength. This alternating electric field could be realized by periodically shielding and unshielding the sensing part of the sensors, and a field mill is a good example for this mechanism.

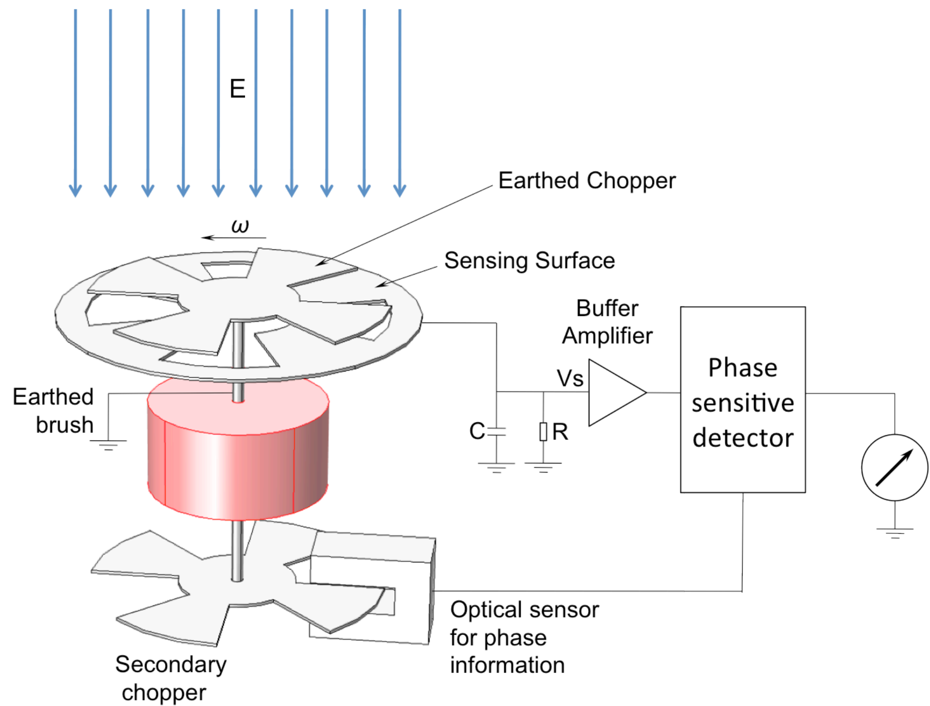

Figure 1.1. Typical structure of a field mill.

Figure 1.1 gives a typical structure of a field mill. An electrically grounded chopper is powered by the motor and rotates above the sensing surface to generate an alternating field. The field causes a time varing induced charge on the surface, which leads to a current in the sensing circuit. The amplitude of the current is proportional to the incident field strength so that the field strength could be determined.

Details of different electric field sensor designs are covered in Chapter 2. Other difficulties (e.g. charging problems) also occur in the dc field measurements. Any sensor placed in a dc electric field will be gradually charged up and eventually form an equipotential, as a result the output signal simply drops to zero. This could be overcome by a good electrical grounding of sensor components.

In Manitoba, HVDC transmission lines are used to transmit electricity from the northern part of the province to the south. Manitoba Hydro uses field mills to monitor the

transmission system. However, the field mills now in use require frequent maintenance. Because of the harsh winter in Manitoba, this might not be available year-round. A new field mill with a long life span and stronger mechanical structure is required and it could be achieved with micromachining technology.

1.3 Micromachined Field Mill Sensors

Several groups have researched micromachined electric field mills (MEFMs). This is discussed in detail in Chapter 2. Wijeweera [20] introduced a MEFM based on a resonant shutter moved by thermal actuators in his thesis, shown in Figure 1.2.

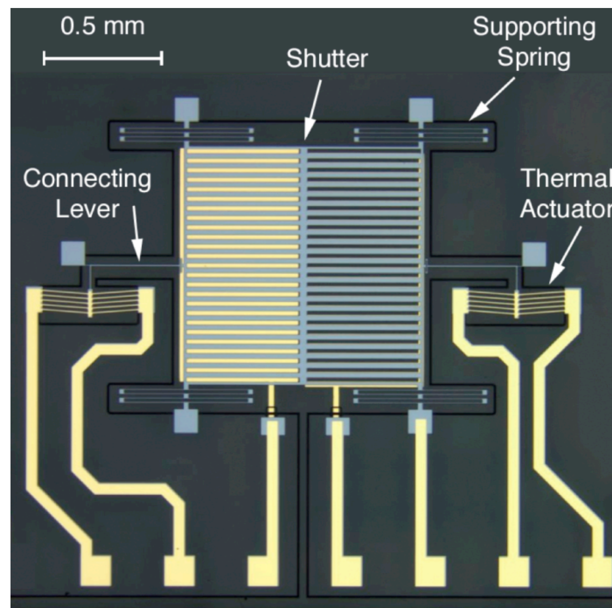

Figure 1.2. Micromachined sensor fabricated by Wijeweera [20].

The sensor has a single crystal silicon shutter of area 1mm×1mm and gold electrodes at the bottom of a 10 μm deep cavity beneath. The electrode arrays are positioned so that when one is shielded by the shutter, the other is exposed to the electric field through slits in the shutter, enabling a difference field measurement without a ground reference. The shutter is actuated by two thermal actuators, with a lever system to amplify the displacement. Designed to work at its resonant frequency, the maximum shutter displacement is around 20 μm, matching the widths of the slits in the shutter.

Tests showed that the sensor design outperformed almost every other MEFM reported [21,22,23,24,25,26], and demonstrated a minimum detectable field strength at 42 V/m. However, this resonant working sensor design has a few drawbacks.

First, the MEFM charges over time when the sensor is placed in the dc field, which leads to a complete loss of the output signal. Second, strong fields pull the shutter and so shift the resonant frequency of the sensor by changing the spring constant of the suspension springs. This complicates the sensor design, as it would require a resonant tracking circuit to control the shutter motion.

My research includes modifications to the original design [20] to overcome the drawbacks. Some of my thesis studies have focused on:

- Gold coatings elements to mitigate charging;
- Non-resonant MEFM design based on the optimization of the sensor structure to enhance the sensitivity;
- In-house fabrication process.

Discussion of these topics forms this thesis.

1.4 Document Layout

Chapter 2 presents a brief introduction of different electric field measurement technology and corresponding sensors. Chapter 3 provides details of the MEFM sensor design along with knowledge of the fabrication process. Chapter 4 describes the numerical simulations. And Chapter 5 describes the analyses of the results from the simulation together with conclusions derived from the simulations.

Chapter 2 Electric Field Measuring Technology

This chapter will discuss several available electric field measuring methods and instruments for measuring electric field. The available electric field meters can be generally categorized into three types below [27]:

a. Electro-optic Meters
b. Free-Body Meters
c. Ground Reference Meters

Each type of meter has its own theory of operation and set-up, which are discussed below. Besides those three main types, few other kinds of electric field measuring technologies are also presented.

2.1 The Electro-Optic Meter

Electro-Optic Meters rely on the fact that the optical properties of certain materials are altered by a change of the electromagnetic field. This type of field meter does not require a ground reference and is generally passive while ideally no metal is needed [28], therefore minimizing any perturbation to the measured electric field.

The Working Principle of the Electro-Optic Meter:

The velocity of light in materials is decided by the refractive index of the material. In some materials, when an electromagnetic field is applied, birefringence appears as refractive indexes in different directions are altered. This causes a variation in the velocity of orthogonal components of polarization of light. For each orthogonal component, the refractive index follows the equation [29]:

$$n = n_0 + aE + bE^2 + \ldots\ldots , \qquad (2.1)$$

where n is the refractive index, n_0 is the normal refractive index without applying an electromagnetic field, E is the electric field, a is the coefficient of Pockels effect and b is

the coefficient corresponding to the Kerr effect. Higher orders of E have less effect on the refractive index, therefore can be neglected.

An Electro-Optic electric field sensor with light modulator was reported by I.Zaldívar-Huerta et al. [30] (see Figure 2.1).

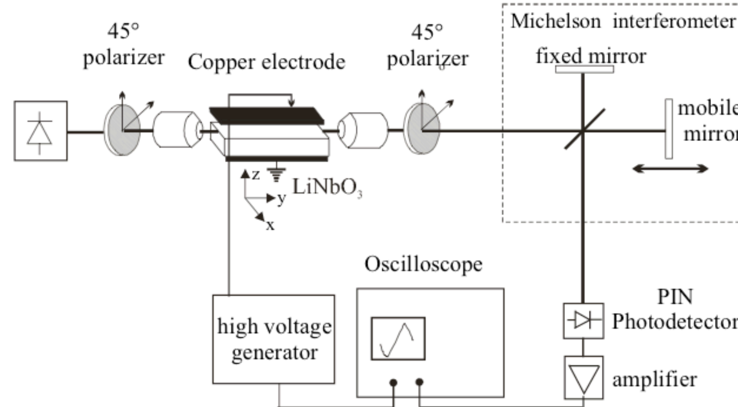

I. Zaldívar-Huerta, J. Rodríguez-Asomoza, 'Electro-Optic E-field Sensor Using an Optical Modulator', Electronics, 14th International Conference on Communications and Computers, 16-18 Feb. 2004, pp. 220-222.
© 2004, IEEE.

Figure 2.1. An Example of Electro-Optic sensor system [30].

The sensor is based on optical coherence modulation, while the optical delay is introduced by the electro-optic property of the lithium niobate ($LiNbO_3$) crystal. The sensor is designed so that orthogonal components of polarized light, emitted by a broadband LED, are launched into the modulator. When an ambient electric field is applied across the $LiNbO_3$ crystal, the refractive indexes within alter differently for the orthogonal light components, which results in a difference in their propagation speed. Therefore, an optical delay is generated between the orthogonal components. The length of the modulator is designed such that the static optical delay is larger than the coherence length. Therefore, no interference appears at the end of the modulator. The optical delay at the modulator follows the equation:

$$D(t) = d_0 + \Delta d(t) \tag{2.2}$$

where d_0 is the static delay, $\Delta d(t)$ is the time-depended delay. After the modulator, a Michelson interferometer works as the optical demodulator to measure the autocorrelation, which is the cross-correlation of the light signal with itself. The intensity detected is given by the equation:

$$I(d) = \frac{I_0}{4}[1 + g(d) + \frac{1}{2}g(d - d_0) + \frac{1}{2}g(d + d_0)] \tag{2.3}$$

where I is the received power, I_0 is the average emit power of source, and $g(d)$ is the normalized autocorrelation received corresponding to the optical delay d. In their experiment, the optical path-difference of the Michelson interferometer is set to be $d=d_0-\lambda/4$, which gives a I corresponding to the E_z by:

$$I(t) = \frac{I_0}{4}\left(1 + \frac{\pi}{2}\frac{E_Z(t)}{E_\pi}\right) \tag{2.4}$$

From the equation above, the E could be derived from the detected optical power.

Despite its merits, the electro-optic e-field sensor is less sensitive to the field strength, with the average sensitivity of an electro-optic e-field sensor is around 5 kV/M [27].

2.2 The Free-Body Meter [27]

The Free-Body Meter is another type of electric field meter, which doesn't need a ground reference, therefore could be used to measure the field strength at an arbitrary point of the field. However, because of the working principle, the sensor of the free-body meter should be relatively small to reduce perturbation of the electric field generated.

The Working Principle of the Free-Body Meter:

The Free-Body Meter usually consists of two conducting surfaces as shown in Figure 2.2. The two surfaces are connected with low impedance conductor or wire.

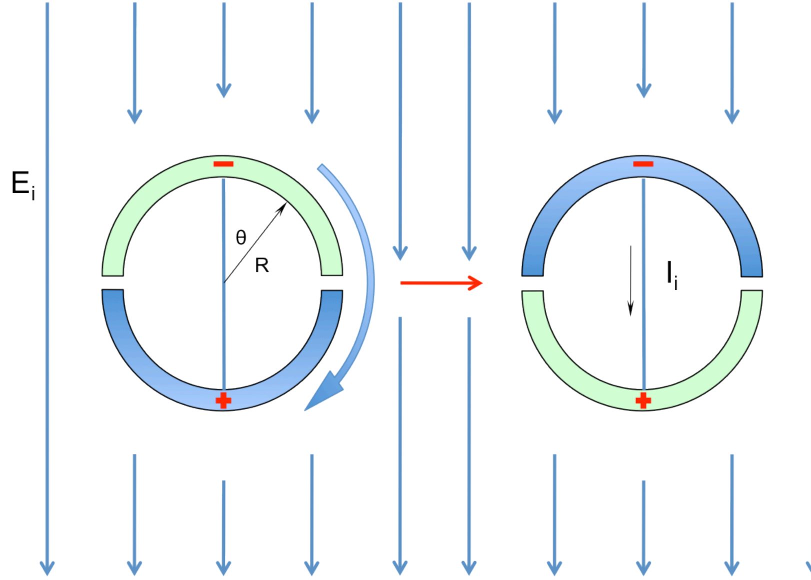

Figure 2.2. Working principle of the Free-Body Meter.

When an incident electric field is applied, charge will be displaced from one surface to the other. The displaced charge density on the surfaces is given by the following equation when the incident electric field is homogeneous [31]:

$$\sigma(\theta) = 3\varepsilon_0 E_i \cos\theta \tag{2.5}$$

where σ is the displaced charge density over each surface, and ε_0 is the permittivity of free space. Thus, for each surface the total amount of displaced charge could be derived by integration over each surface:

$$Q = \int_0^{\pi} R^2 \cdot 3\varepsilon_0 E_i \cos\theta d\theta \tag{2.6}$$

$$Q = 3\pi R^2 \varepsilon_0 E_i \tag{2.7}$$

When the sensor is rotating at an angular speed of ω within a homogeneous electric field, the time varying displaced charge on each surface can be expressed as:

$$\Delta Q = -3\pi R^2 \varepsilon_0 E_i \cos\omega t \tag{2.8}$$

Therefore, the current in the wire joining the two surfaces is:

$$I = \frac{dQ}{dt} = 3\omega\pi R^2 \varepsilon_0 E_i \sin\omega t \tag{2.9}$$

From the above equation, it is apparent that the amplitude of the current I is proportional to the incident electric field E_i and the rotating angular speed ω.

Free-Body Meter Example:

A Free-Body meter based on the principle above has been fabricated and tested by K. Johansson et al. [32]. Figure 2.3 is a snapshot of the probe measuring 26 mm in length and 12 mm in diameter.

K. Johansson, L. Walfridsson, U. Gäfvert, B. Källstrand, S. Hörnfeldt, 'Probe for measurements of the DC electric field in air around high voltage apparatus', 2010 Annual Report Conference on Electrical Insulation and Dielectric Phenomena, 17-20 Oct. 2010, pp. 1-4.
© 2010, IEEE

Figure 2.3. An example of a Free-Body Meter [32].

The sensor has two electrodes mounted on both sides and when rotating in the electric field, the current between two electrodes is measured by an electrometer powered by a battery. The electric output signal is sent through an optical fiber. The sensor has a resolution at 100 V/m and a maximum measuring limit at 500 kV/m when rotating at 1500 rpm. Though initially designed to be a dc electric field sensor, the sensor could also measure ac electric fields with low frequency compared to the rotational speed of the sensor.

2.3 The Ground Reference Meter

The ground reference meter is usually used to measure the field strength at the ground level [27]. The field strength is generally determined by measuring the current or the induced charge on the surface of the probe. Figure 2.4 illustrates the working principle of a ground reference meter.

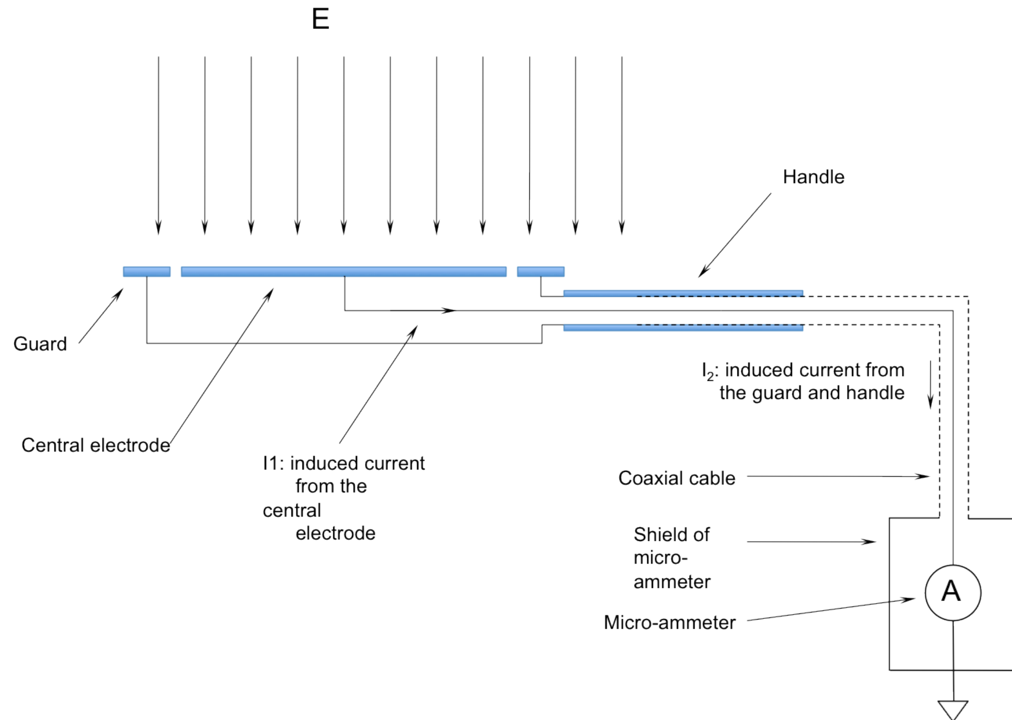

Figure 2.4. Schematic view of a ground reference sensor.

A ground reference meter determines the field strength by measuring the current or the induced charge on the surface of the probe that is usually a conduction electrode. From Gauss' Law:

$$Q = \varepsilon_0 \varepsilon_r E_i A \tag{2.10}$$

where ε_0 is the permittivity of the vacuum, ε_r is the relative permittivity of media, E_i is the incident electric field strength, and A is the area of the conducting electrode. It is obvious that the induced charge is linearly proportional to the field strength. When measuring an ac field, the field strength varies in a sinusoidal way, say $E_i=E_0 sin\omega t$, which gives a current [27]:

$$I = \frac{dQ}{dt} = \omega \varepsilon_0 \varepsilon_r E_0 A \cos \omega t \tag{2.11}$$

When a dc field is applied, the sensing electrode will be charged up rapidly and the current will saturate. Various mechanisms should be applied to either alter the incident field or neutralize the sensing electrode.

2.3.1 Ground Reference Meter Example

A ground reference meter design has been put forward by Charles J. Miller [33] early in 1967, see Figure 2.5.

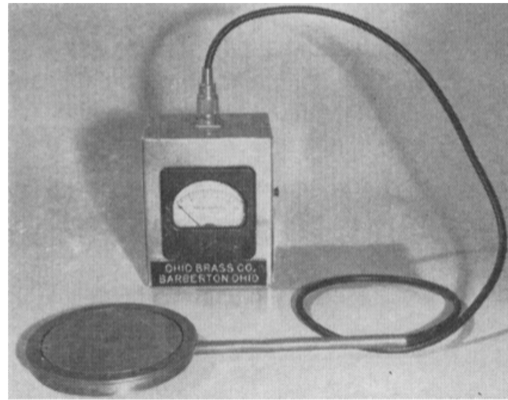

Charles J. Miller, Jr., 'The Measurement of Electric Fields in Live Line Working', IEEE Transactions on Power Apparatus and System, Apr. 1967, Vol. Pas-86, Issue 4, pp. 493-498.
©1967, IEEE

Figure 2.5. A snapshot of the ground reference sensor designed by Charles J. Miller [33].

An oscillation of the induced charge occurs on the surface of the central electrode, guard and handle when the sensor was placed in an ac electric field. When connecting the probe to a micro-ammeter through a coaxial cable, a current I_1 from the central electrodes flows through the micro-ammeter while a current I_2 from the guard and handle goes to the ground directly through the shield of the micro-ammeter. Since I_1 is proportional to the strength of the incident electric field, the field strength E can be determined. The resolution of the sensor is 39.37 kV/m at a frequency of 60 Hz.

The drawback of the ground reference meter is obvious, that it saturates in a dc electric field. This can be overcome in field mill instruments [34].

2.4 Electric Field Mill

A field mill modulates an incident dc field into an alternating field by rotating a traditionally grounded chopper above the sensing electrodes, so that the charging problem of the sensing electrodes can be resolved. Research has shown that the peak of the output signal is proportional to the strength of the electric field [35]. Figure 2.6 shows a general arrangement of the electric field mill.

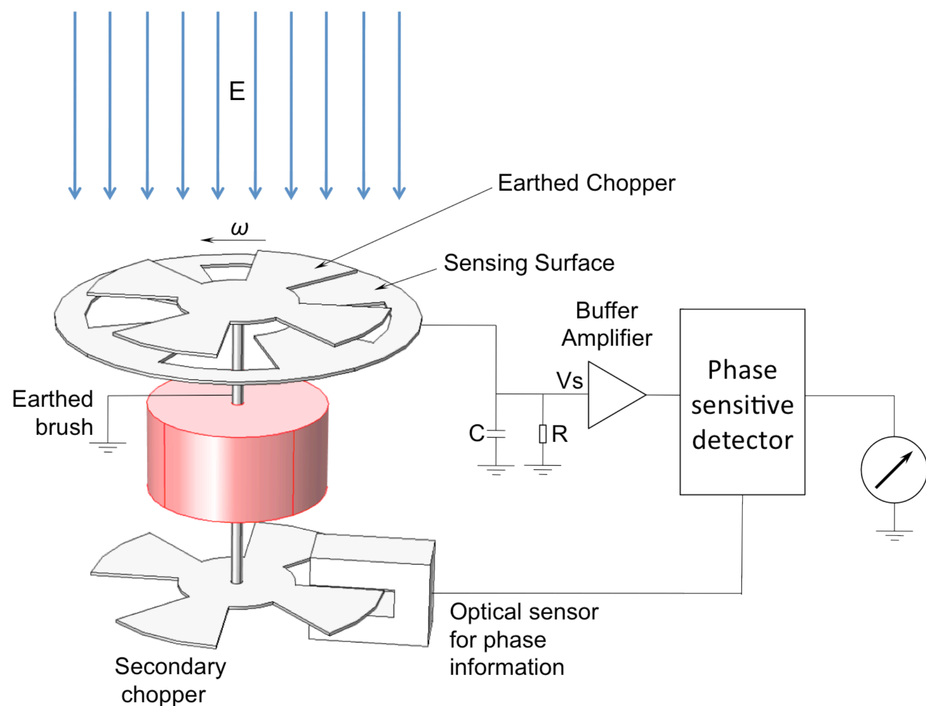

Figure 2.6. Field mill with its electronic circuit.

Commercially available field mills are usually battery powered and have been used in monitoring HVDC transmitting lines and atmospheric analyses for more than two decades [20].

Despite of their high sensitivity, as small as 20 V/m [36], conventional field mills have several drawbacks. They have to be grounded otherwise they won't be able to

measure dc fields due to the charging up of the sensor structure. Moreover, the rotating structure of the conventional field mill tends to wear out over a long time, limiting operation life span. Power consumption is another problem, as almost every field mill requires motors powered by batteries [37]. Finally, conventional field mills are expensive. The price of a typical commercial field mill along with its electronics and power ranges from $1000 to $7000.

Designs working without the ground reference have been reported by John N. Chubb [34]. Two designs are presented in the Figure 2.7.

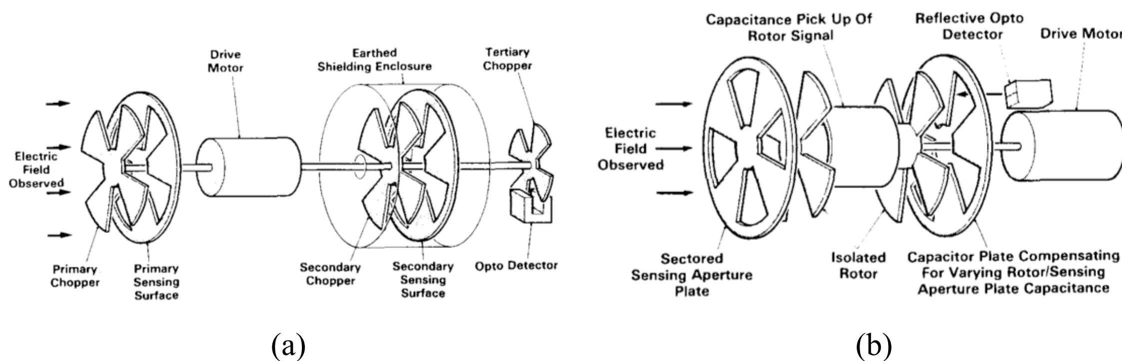

J.N. Chubb, 'Two new designs of field mill fieldmeter not requiring earthing of rotating chopper', IEEE Trans. Ind. Appl., Nov/Dec. 1990, Vol. 26, Issue 6, pp.1178-1181. ©1990, IEEE

Figure 2.7 (a). Field mill with compensation for rotor voltage; (b). Field mill with constant-capacitance rotor. [34]

Figure 2.7(a) illustrates a field mill with compensation for rotor voltage. In this design, two sets of field mills are mounted together using a single unearthed drive motor. Two choppers are connected electrically with a shaft while the secondary one is hidden behind an earthed shielding enclosure. As the electrical ground is not available in this case, the first chopper is floating. When exposed to the incident dc electric field, the chopper will charge up and generate an electric field that cancels the incident field reaching the primary sensing surface. In order to get an accurate measurement of the incident field, a compensating mechanism is required. The signal generated on the primary sensing electrodes is proportional to the combination of incident field and the

potential on the choppers, while the reading of the secondary sensing electrodes is the potential on the choppers. Therefore, the incident field strength could be derived by subtracting the reading of the secondary one from the primary one.

Figure 2.7(b) demonstrates another field mill design without a ground reference. In this design, an insulated sectored rotor is rotating behind a sectored shield plate. The incident field couples through the shield plate and generates an alternating potential on the rotor, the potential is capacitively coupled to an preamplifier input circuit. A compensating capacitance plate is attached behind the rotor so that the capacitance of the rotor is a constant during the rotation therefore the input signal is independent of any net voltage on the rotor. The strength of the incident electric field could be achieved by detecting the phase of the capacitively coupled signal from the rotor.

These two designs, while not requiring a ground reference, have worse performance than the common electric field mills. The former one has twice the thermal noise due to two sets of field mills, and for the latter one, the signal is attenuated by the capacitance division that leads to an increased single-to-noise ratio, which attenuates the source signal.

2.5 E-field measurement based on Lyman-α radiation of metastable hydrogen beam:

A new E-field measuring technique using the Lyman-α radiation has been reported by A. Lejeune et al. [38]. This technology shows a promising future in electric field measurement in vacuum environment. Using this technology, a weak electric field as low as 10 V/m for dc and 1 V/m for ac can be measured, by launching a beam of metastable hydrogen atoms through the electric field and collecting and measuring the intensity of the Lyman-α radiation emitted. When a hydrogen atom is exited, the electron of the atomic system will go to the stimulated state which is not stable. After emitting a photon, it will go back to the stable state or metastable state where the electron could stay in without outside perturbation. For example, the transition of hydrogen atomic system

from its metastable state, $2s_{1/2}$, to the $1s_{1/2}$ ground state, can be achieved by applying an external electric field. During this transition, the hydrogen atom emits a photon with a wavelength equal to 121.6 nm. This specific radiation is called Lyman-α radiation. The intensity of this radiation can be altered by the strength of the external electric field which changes the lifetime of the $2s_{1/2}$ state.

2.6 Micromachined Electric Field Sensors

Micromachining technology offers new methodologies for fabricating electric field sensors. MEMS technology offers advantages including smaller size and light weight, small power consumption, integration with electronics, and bulk fabrication which reduces the cost. What's more, as arrays of sensors can be applied and the perturbation to the incident field can be minimized with this dramatic shrink in size, a higher accuracy in measurement can be achieved even with the fact that for each individual sensor, the sensitivity may be less than the macroscopic counterparts.

MEFM Sensors:

A few micromachined electric field mill (MEFM) sensors are discussed below. The MEFMs constitute of a moving shutter, sensing electrodes and driving system. However, because of the difficulty in designing and fabricating a rotating structure with MEMS technique, most of the micro-machined field mills adopt a vibration motion as the moving mechanism of the shutter. In terms of the driving mechanism, comb drive and thermal actuators are mostly used.

Figure 2.8 illustrates a MEFM using a thermal actuator as the driving mechanism reported by Chen et al. [24]. In this design, they used a pair of bent beam thermal actuator as the driving mechanism. The thermal actuators were cascaded to enhance the total displacement of the shutter. The total area of the sensing electrodes is $1mm^2$. The driving voltage of their design was 2V and the sensor achieved a resolution of 240.8 V/m.

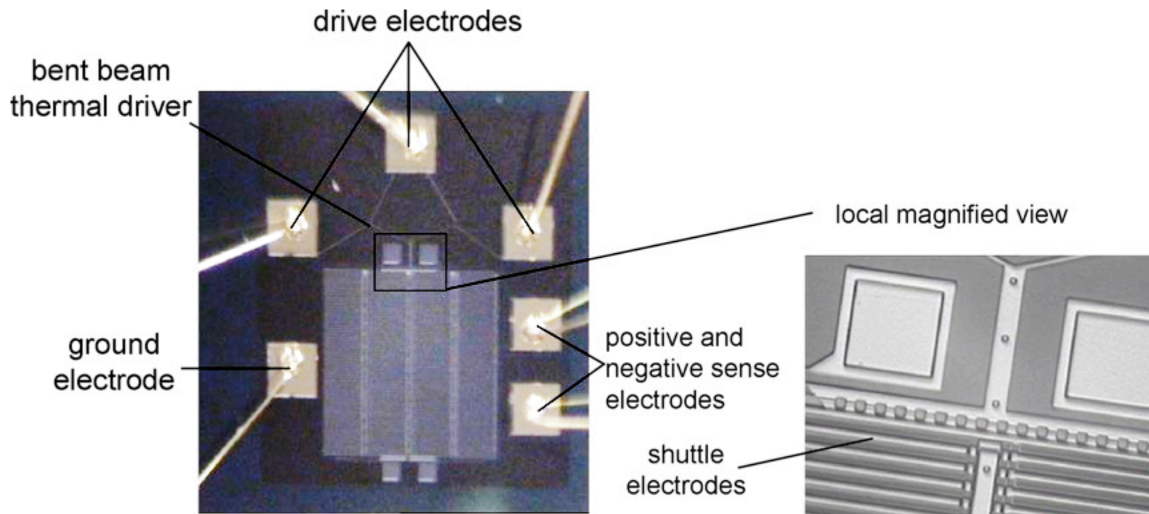

Xianxiang Chen, Chunrong Peng, Hu Tao, Chao Ye, Qiang Bai, Shaofeng Chen, and Shanhong Xia, 'Thermally driven micro-electrostatic fieldmeter', Sensors and Actuators A: Physical, 20 Nov. 2006, Vol. 132, Issue 2, pp. 677–682.

Figure 2.8. MEFM with thermal actuator [24].

Figure 1.2 illustrates the MEFM fabricated by Wijeweera [20]. The sensor has a single crystal silicon shutter with the area of 1mm×1mm and two arrays of gold electrodes patterned at the bottom of a 10 μm deep cavity beneath the shutter. The electrode arrays are positioned so that, when one is shielded by the shutter, another is exposed to the electric field through the slits, to carry out the difference field measured without any ground reference. The shutter is suspended by four sets of springs one at each corner and is actuated by two thermal actuators with a lever system to amplify the displacement. When working at its resonant frequency, the sensor achieved minimum detectable field strength at 42 V/m.

A comb drive actuated MEFM design from Yang et al. is shown in Figure 2.9 [39]. Instead of common strip sensing electrodes which lay beneath the shutter, comb electrodes were used in this design, see Figure 2.9 (b). An improved sensitivity was achieved using this kind of electrode design according to the report, and they also applied a symmetric structure to suppress the feed-through from the actuator into the sensing circuitry. The sensor itself operated at its resonant frequency to amplify the displacement of the structure. When applied with a 20 V dc bias voltage and antisymmetric $1V_{p\text{-}p}$

sinusoidal voltage on the comb drive, the sensor demonstrated a measurement range of 0-50 kV/m in electric field strength with a minimum detectable field of around 40 V/m.

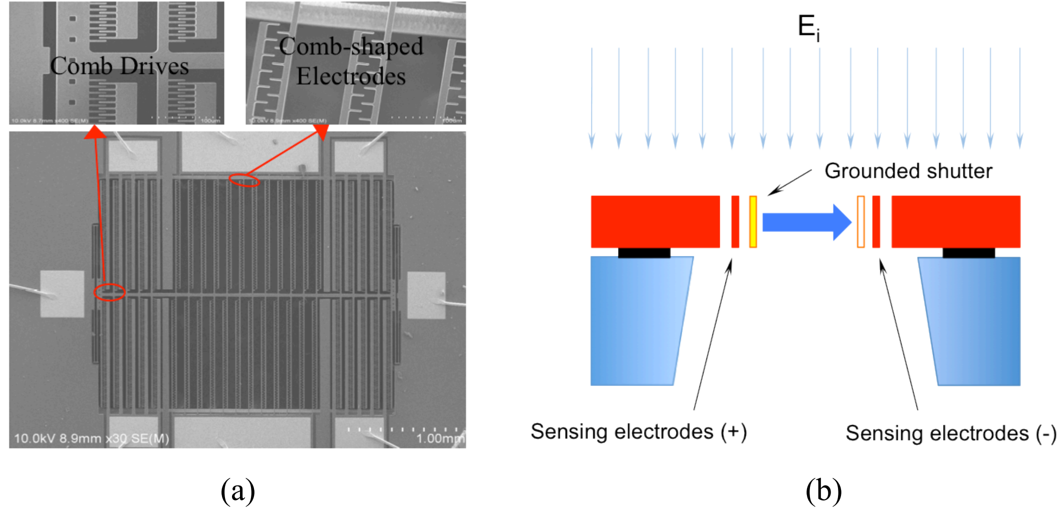

Pengfei Yang, Chunrong Peng, Haiyan Zhang, Shiguo Liu, Dongming Fang, and Shanhong Xia, 'A high sensitivity SOI electric-field sensor with novel comb-shaped microelectrodes', 16th International Solid-State Sensors, Actuators and Microsystems Conference, 5-9 Jun. 2011, pp. 1034-1037. ©2011, IEEE

Figure 2.9 (a). MEFM with comb drive and comb-shaped electrodes; (b). Schematics of the cross-section. [39]

Micromachined E-field sensor using electrostatic force:

Figure 2.10 is a schematic of the electrostatic force sensor reported by A. Roncin et al. [40]. The sensor consists of a spring supported copper membrane with a laser position sensor measuring the deflection of the membrane. An ac voltage is applied to the membrane so that when placed in the electric field, the membrane will oscillate at the frequency of the applied ac voltage. The amplitude of the oscillation, proportional to the square of the difference of the potential of the incident field and applied voltage, see Equation 2.12 and 2.13, is measured by the laser sensor.

$$F = \frac{\partial W}{\partial z} = -\frac{1}{2}\varepsilon_0 A E^2 = -\frac{1}{2}\varepsilon_0 A\left(\frac{V_m - V_s}{z}\right)^2 \quad (2.12)$$

$$F = k\Delta z \tag{2.13}$$

where F is the electrostatic force on the membrane, W is the energy stored in the capacitor system consisting of the membrane and the field source, ε_0 is the permittivity of vacuum, A is the surface area of the membrane, E is the electric field strength, V_m is the voltage on the membrane, V_s is the voltage of the field source, z is the distance separating the membrane and the voltage source, k is the total spring constant of the micro-springs, and Δz is the displacement of the membrane. The sensor achieved a resolution at 5 kV/m when measuring a dc field, and a 0.3 V/m resolution when measuring an ac field at 97 Hz.

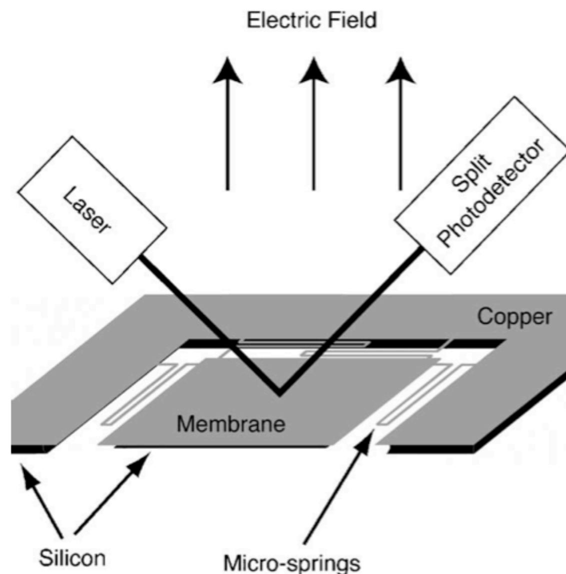

A. Roncin, C. Shafai, and D.R. Swatek, 'Electric field sensor using electrostatic force deflection of a micro-spring supported membrane", Sensors and Actuators A: Physical, 23 Sep. 2005, Vol. 123-124, pp.179–184.

Figure 2.10. Schematic view of sensor developed by A. Roncin et al. [40].

2.7 Comparison of different techniques

Various electric field measuring techniques have been presented in this chapter. Table 2-1 gives a comparison of each individual techniques and sensors.

Table 2-1. Comparison of different e-field measurement technology.

Reference	Category	Sensing mechanism	Sensitivity	Advange & Disadvantage
I. Zaldivar-Huerta et al. 2004	Electro-Optic electric field sensor	Electro-Optic electric field sensor with light modulator		Passive sensor, less perturbation; Less sensitivity
K. Johansson et al. 2010	Free-body meter	Two rotating surfaces connected with low impedance conductor	100 V/m	No ground reference required;
Charles J. Miller, Jr. 1967	Ground reference meter	Field strength determined by measuring the current or the induced charge on the surface of the probe	39.4 kV/m	Ground reference required.
John Chubb Instrumentation	Field mill	Rotating chopper modulates the field, measuring the induced charge on the sensing pad.	20 V/m	High sensitivity; Ground reference and maintenance required;
A. Lejeune et al. 2011	Lyman-α radiation	E-field strength determined by Lyman-α radiation of metastable hydrogen beam	10 V/m for dc; 1 V/m for ac;	High sensitivity; High vacuum required;
Chen et al. 2006	MEFM	Thermal actuator driven electric field mill	240.8 V/m	
Wijeweera et al. 2009	MEFM	Thermal actuator driven electric field mill	42 V/m	High sensitivity; Resonant working.
Yang et al. 2012	MEFM	Comb drive actuated, comb-shape electrodes applied	around 40 V/m	High sensitivity; Resonant working.
A. Roncin et al. 2005	Micro-machined electrostatic field sensor	Electrostatic force deflects a membrane.	5 kV/m for dc; 0.3 V/m for ac.	Extremely high sensitivity for ac.

Chapter 3 Sensor Design and Fabrication

3.1 Conventional MEFM

The brief introduction of the conventional MEFM has been done in chapter 2. Similar to the electric field mill, the conventional MEFM consists of a grounded shutter with perforations in it, a set of electrodes to sense the field strength, and an actuating mechanism to drive the shutter (see Figure 1.2).

The sensor fabricated by Wijeweera [20] outperformed almost every other MEFM reported [21,22,23,24,25,26]. However, it suffered from a few drawbacks.

a. Charging effect.

The sensor starts to be charged up right after the electric field is applied. Eventually, when fully charged, the entire sensor becomes an equipotential and the signal is completely lost.

b. Shifting of resonance.

Since the sensor requires resonance to magnify the shutter displacement to be sufficient to cover the electrodes, the sensor is fairly sensitive to changes in the environment. Shutter lift from the electric field, temperature changes and changes in packaging pressure will shift the resonance and affect the sensor output.

c. Non-optimized geometry for measuring electric field.

The shutter structure of the last generation shutter [20] was designed without any optimization applied. Therefore, it might not be able to provide the maximized sensitivity with the given total displacement of the shutter.

Solutions to problems a and c above form the main body discussions of this thesis. Solution to problem b, was the subject of the M.Sc. thesis of Mark Roy [41].

3.1.1 Fabrication of the Sensor

The sensor of Wijeweera [20] was fabricated using the MicraGem fabrication process developed by Micralyne Inc. (Edmonton, Canada) [42]. The fabrication process flow is:

a. Trenches with depth of 2 μm and 10 μm respectively are etched isotropically into a Pyrex substrate.
b. Gold is deposited on the bottom of the trenches and is patterned to form the electrodes.
c. A silicon on isolator (SOI) wafer is bonded to the Pyrex substrate with the device layer contacting the substrate.
d. The SOI wafer is back-etched to totally remove the handle layer and the oxide layer, exposing the device layer for the following steps.
e. Gold is deposited on the device layer and patterned to provide the wiring connection.
f. The device layer is patterned and etched using a DRIE (deep reactive ion etching) to form the upper structure including shutter, springs and actuation mechanism.

Unfortunately, CMC Microsystems no longer makes available to universities MicraGem fabrication. To enable in-house fabrication of the sensor at the University of Manitoba, silicon-pyrex bonding equipment (step c above) and plasma etch recipes (step f above) needed to be developed. Plasma etch processes were developed as part of this thesis, while bonding equipment was developed as part of the M.Sc. thesis of Mark Roy [41].

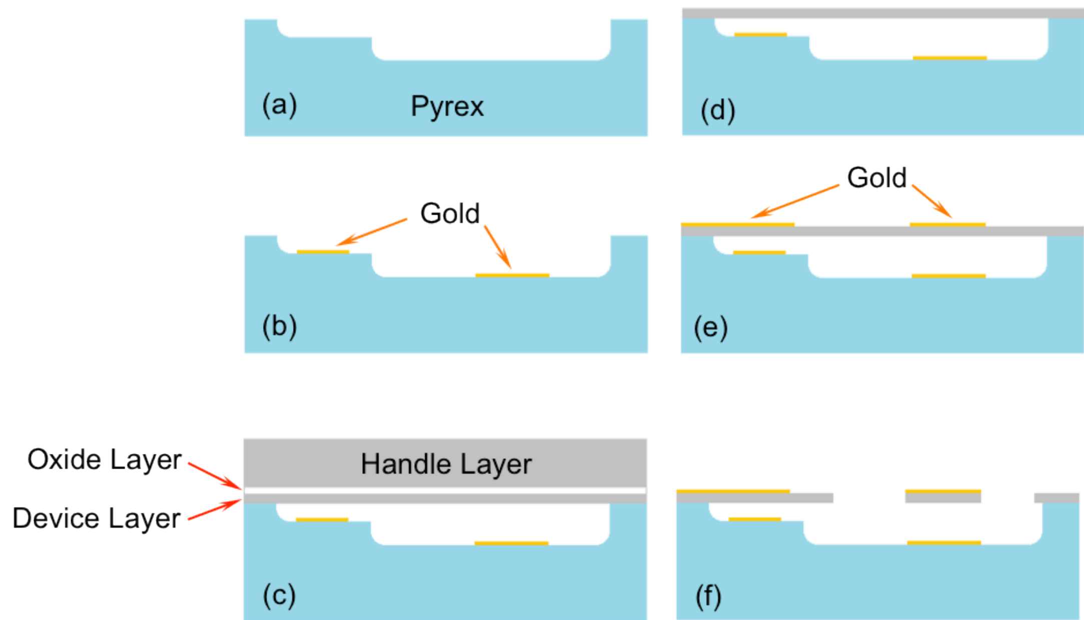

Figure 3.1. MicraGEM fabrication process: (a) Trenches are etched into Pyrex substrates. (b) Gold electrodes are patterned. (c) A SOI wafer is bonded to the substrates. (d) Back-etch the SOI wafer. (e) Gold is patterned on the device layer. (f) Structure is released (plasma etch recipes required).

3.2 In- House Fabrication Process

3.2.1 Lithography

Lithography is the starting of almost all the fabrication process, while photolithography is the most widely used form of lithography [43]. Most pattern transfer in the IC industry is achieved via photolithography. A standard photolithography process follows the following steps:

Resist Spinning and Soft Bake:

Spin coating of the photoresist is the first step of the photolithography. In this step, a thin layer of photoresist from a viscous solution is poured onto the wafer sitting on the spinner. Then, the solution is spun leaving a layer of photoresist with a uniform thickness, typically between 0.5 to 2 μm. The thickness of photoresist after spinning is proportional to the inverse square root of the spinning speed. Figure 3.2 gives a brief demonstration of resist spinning:

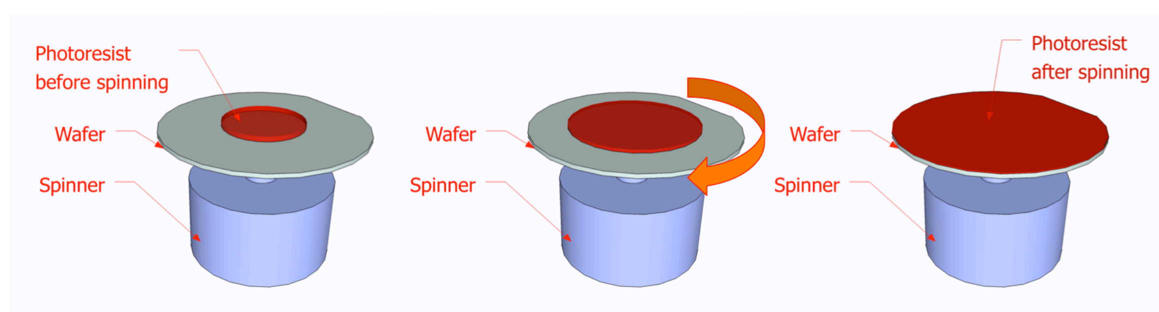

Figure 3.2. Demonstration of resist spinning.

In our fabrication process, HDR 504 positive photoresist was used, spun at 5 krpm for 25 sec, resulting in a resist film of 1.2 μm.

After the spinning, a soft bake is employed to remove the remaining solvent in the resist. It can also remove the built-in stress in the resist film. A typical soft bake could be

a bake at 90 °C to 110 °C, 30 to 60 sec on the hot plate, or 30 min in the oven. In our process, a 100 °C, 60 sec bake on the hot plate was used.

Exposure:

After soft bake, the wafer with resist film on it is exposed to the UV in the mask aligner to transfer the mask pattern to the resist film. Contact exposure is used in our process. In contact exposure, the mask is in direct contact with the substrate. This gives a relatively high resolution and no complex projection lens system is required. When the mask and substrate was perfectly aligned, a 3.5 sec exposure was applied found through experimentation.

Developing:

Developing is the step where the resist film is patterned by removing the soluble part of the resist after UV exposure. Aqueous alkaline is used as the solution when trying to develop a positive photoresist. Typically, developing of the resist is done by spraying the solution on the wafer surface. Timing is quite essential; a careful timed developing is usually critical to the lithography process where both temperature and humidity could change the optimal time of the developing. In our process, a 15 sec develop was used with the temperature at 25±1 °C and a 22±2 % relative humidity in the cleanroom. Some of the results after developing are given in the Figure 3.3.

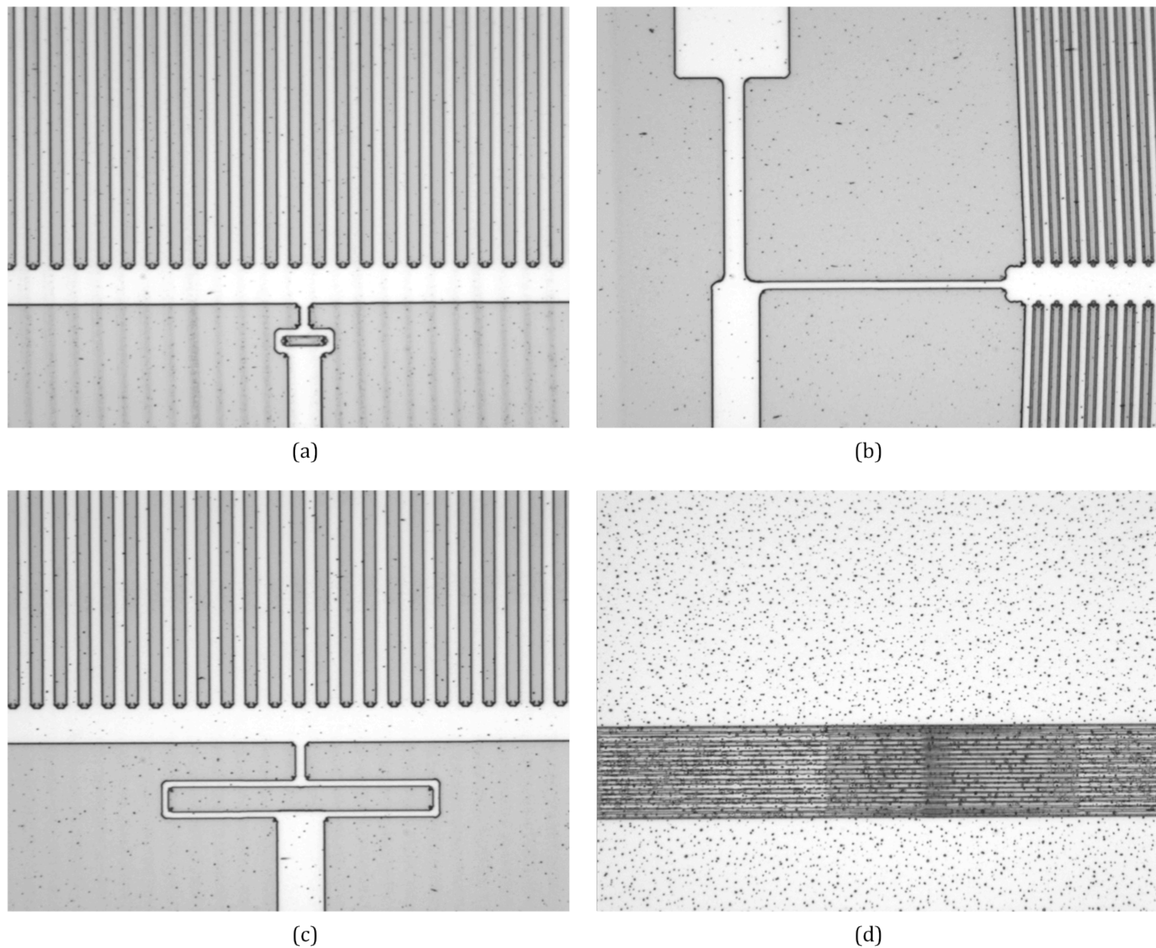

Figure 3.3. Results of the lithography. (a) Shutter with 5 μm slits; (b) Actuator and lever system; (c) Another design of shutter with 5 μm slits; (d) 2 μm parallel lines.

From Figure 3.4, it is obvious that the designed lithography process worked well with the structure of the sensor, and could achieve a minimum non-repeating feature at round 2 μm. This is good enough for the shutter structure in our design. The curves appearing at each corner were brought in during exposure and were further enhanced by developing.

3.2.2 Plasma Etching

A slit with perfectly vertical sidewall was desired for the design and fabrication of MEFM. That requires a highly anisotropic plasma etch process when etching and

releasing the shutter structure. DRIE was used in the original MicraGEM fabrication process to achieve this vertical sidewall, however, this equipment does not exist in the NSFL, and so an alternative had to be figured out. Wet etch is not considered as a candidate, for it could not give a highly anisotropic (vertical sidewall) profile. Examples of non-anisotropic etching are given in Figure 3.4:

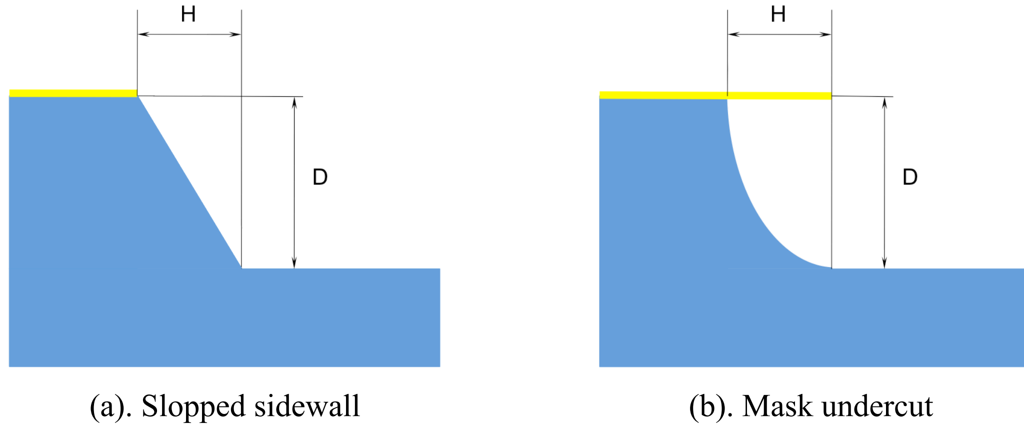

(a). Slopped sidewall (b). Mask undercut

Figure 3.4. Examples of non-anisotropic etching.

The anisotropic rate (A) could be calculated by:

$$A = 1 - \frac{H}{D} \tag{3.1}$$

An RIE technique similar to the black silicon method [44] was selected. A Trion Phantom II ICP/RIE plasma etcher was used in the experiments of this thesis.

Working Principle:

A universal method for determining the recipe of a fluorine-based RIE of silicon, which gives a control over the profile of the trench, was developed by H. Jansen et al. [45]. Based on the anisotropic silicon etching recipe using SF_6 and O_2 [46].

The working principle of SF_6 silicon etching is the generation of free fluorine when ionizing the SF_6 [47].

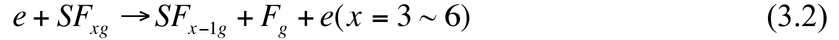

$$e + SF_{xg} \rightarrow SF_{x-1g} + F_g + e(x = 3 \sim 6) \qquad (3.2)$$

The free fluorine atoms then react with silicon to perform the etching.

$$Si + 4F \rightarrow SiF_4 \qquad (3.3)$$

where SiF_4 vaporizes at -86 °C. The SF_x+ ion reacts with oxygen and generates SO_xF_y that is also gaseous. SF_6 etch is, however, isotropic in common plasma etch parameters. The method of enabling anisotropic etching is achieved is by employing a passivation layer to protect the sidewalls during the etch, preventing undercut. From the research of Legtenberg et al. [48], adding oxygen to the gas mixture causes a SiF_xO_y film to be deposited on the reaction surface. This SiF_xO_y film works as the passivation layer that stops the fluorine atom from reaching the silicon beneath the layer on the sidewalls, see Figure 3.5. On horizontal surfaces, however, the passivation layer on the horizontal surface of silicon can be removed by the ion bombardment of the SF_x^+ ions accelerated by the electric field. This can result in a more vertical etch profile. However, in practice continuous buildup of passivation layer as the etch progresses, results in a sloped profile, as opposed to vertical. Thus, a method is needed to remove the excess passivation build-up. When CHF_3 gas is added into the process it consumes the passivation material and produces the product CO_xF_y gas [49].

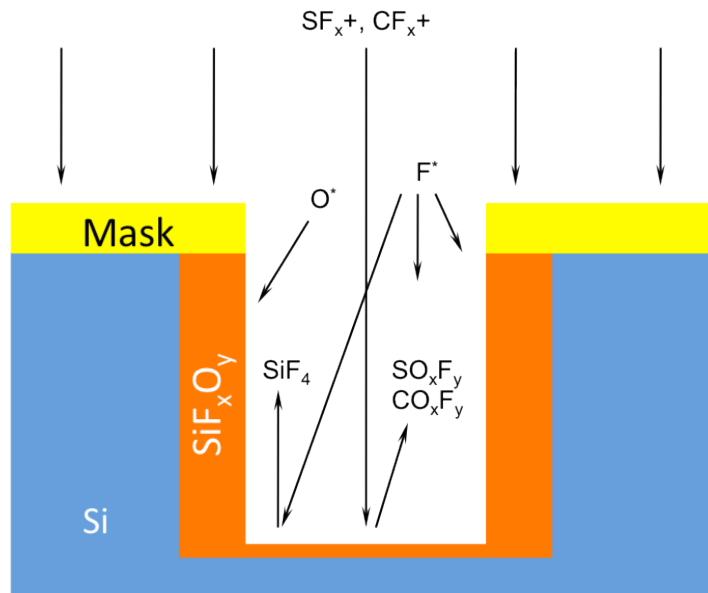

Figure 3.5. Schematic view of the SF_6 /O_2 /CHF_3 etch.

Parameter Analysis:

Several parameters are considered to be critical to the plasma etch. First, the ratio between different ingredient gases. Second, the pressure of the etching chamber. Third, the power of the field generate the plasma. Fourth the total gas flow, which is the rate of gases entering into the chamber, therefore the refresh rate of the etchant. The effect of these parameters on the etch profile will be explained below based on previous studies.

Parameter analysis for anisotropy was given in Legtenberg's paper [48]. According to his study, the anisotropy is mainly decided by the flow of the oxygen and SF_6. An increasing O_2 rate will initially increase the anisotropy until it reaches a maximum, than reduce the anisotropy as outward slopes are generated during the process. Increasing the SF_6 will generally reduce the anisotropy except when the O_2 flow is very large. In this case, an increased F concentration can affect the formation of the passivation layer while SF_5^+ reacts with O_2, forming volatile SO_xF_y that furthermore consumes the oxygen. As a result, the anisotropy increases by adding SF_6 when O_2 flow is high.

Applying a high etching pressure will increase the fluorine concentration and decrease the ion bombardment. Both will cause a reduction in anisotropy. The removal of the passivation layer on the horizontal surfaces heavily relies on the ion bombardment. Moreover, as the movement of ions becomes less directional because of increasing collisions, less SF_x^+ or CF_x^+ could reach the bottom of the trench (see Figure 3.5). Also, with higher fluorine concentration and more collisions, the fluorine atoms have more chance to impact the sidewalls of the trench, etching the silicon and reducing anisotropy.

Increasing the RIE power will increase the fluorine concentration and the bombardment. Legtenberg's study indicates that with an increasing in RIE power, the anisotropy will initially increase, and later on decrease after reaching a maximum.

The effect of total flow rate was investigated by Jorné et al. [50], and no close relation to the anisotropy was observed.

The Mask material is another key parameter in the etching process. The selection of the mask material is based on the etchability, conductivity, temperature and selectivity [51]. Silicon oxide was used as mask material in Jansen's study [51]. Although it can be etched in SF_6, it showed a relatively high selectivity as ion bombardment is a primary effect that controls silicon oxide etch. Photoresist is not considered a good mask material here, since O_2 is one of the etchants in the recipe and can etch photoresist. Metals are generally good mask materials, as they are barely etched by the etchant.

In our etching trials, several metal materials were investigated. Sputtering was used to deposition the metal. Cr is a good material for mask, however, it does not form a non-porous layer of metal in the sputtering system. As a result, the ions may penetrate through the mask layer and reach the silicon beneath. Although copper is strong material that will not be sputtered during the etching, an adhesion layer is required before it could be deposited on silicon, which will make process more complicated. Au was originally designed to be the metal deposited on the surface of the sensor. However, it could be sputtered in the plasma etching, and the cost is great. With all these considerations, aluminum was selected as the mask material.

Etching Experiments:

Etching experiments were done in the NSFL at the University of Manitoba. A Trion Phantom II RIE/ICP plasma etcher was the equipment used to carry out etches. As discussed earlier in this chapter, an anisotropic etch with vertical sidewall requires a balance between the reaction of the etchant fluorine gas and reaction of oxygen with silicon that forms a passivation layer which SF_6 cannot etch. With a certain flow ratio of SF_6 and O_2, oxide formed by the reaction of oxygen with silicon work as the micromask, preventing silicon etching in those locations. This can lead to unetched pillars forming on the surface of the wafer. Figure 3.6 shows the schematic of this process.

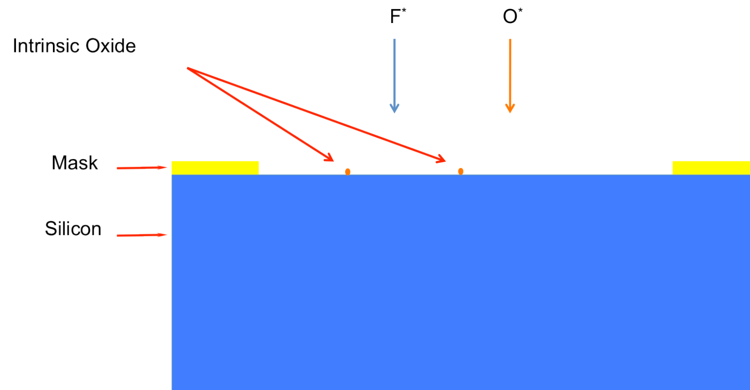

(a) Beginning of the etching with intrinsic oxide on the surface of wafer.

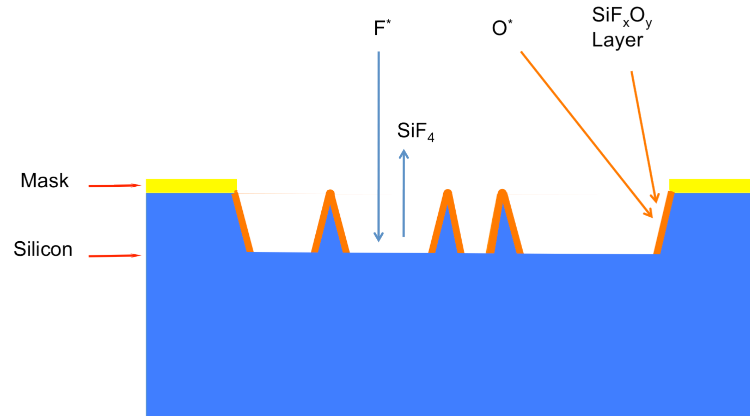

(b) The oxide acts as the mask during etching, and oxide layer is deposited at the sidewall as passivation layer.

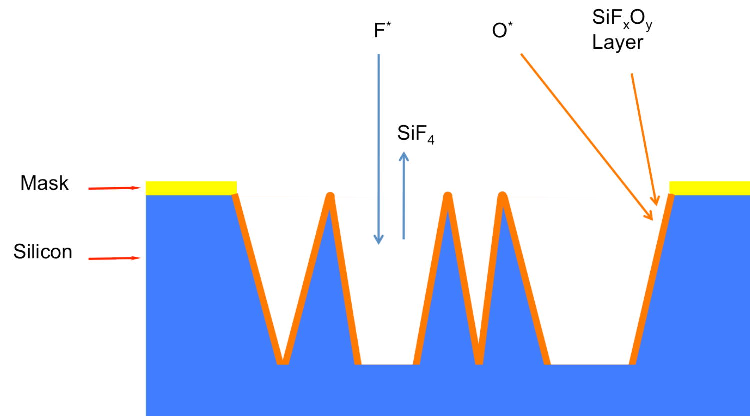

(c) Spikes are formed.

Figure 3.6. Schematic of how surface turns to black.

The pillars scatter the light reflected from the surface and make the surface look black. After the black surface is formed, a correct balance of SF_6 to O_2 has been achieved.

Next, the correct ratio of CHF_3 gas has to added to the mixture, to consume the passivation so that an anisotropic etch with vertical sidewall can be achieved. The basic procedure for determining a good anisotropic etch is as follows.

- Step 1: Etch a piece of silicon with SF_6/O_2 plasma with a preferred pressure and RIE/ICP power. The fluorine ions that etch and oxygen ions that form passivation layer compete with each other. By increasing the amount of oxygen ions, thicker passivation layer will form, especially at the sidewall, to keep it untouched from fluorine ions. Gradually increase the oxygen flow until the surface turns dark. This indicates that an etching without undercut exists.
- Step 2: When the dark etch region appears, add some CHF_3 to the etchant. The effect of CHF_3 is illustrated in Figure 3.7. CHF_3 consumes the oxygen (and so the growth of the passivation layer) and also consumes the passivation itself. Also, it etches the oxide layer either on the surface or on the sidewall. The amount of CHF_3 gas is increased until the balance of the reactions is found to shift the etching profile more negatively tapered and the spikes are removed. Continue to increase the amount of CHF_3 until the surface becomes clear again (no black silicon is formed).
    - Note: For your particular device wafers, a different amount of exposed silicon may be present than on the test wafers, which can also affect the balance of the reactions. And so, a rebalanced of the mixtures in step 1 and 2 may be needed to account for the differing amounts of silicon present in the etch chamber.
- Step 3: Check the etch profile. Parameters could be adjusted in this step until the wanted profile exists. Adding more O_2 will lead to a more positive profile, as well as increase the pressure or reduce the power. While adding more CHF_3 will make profile more negative.

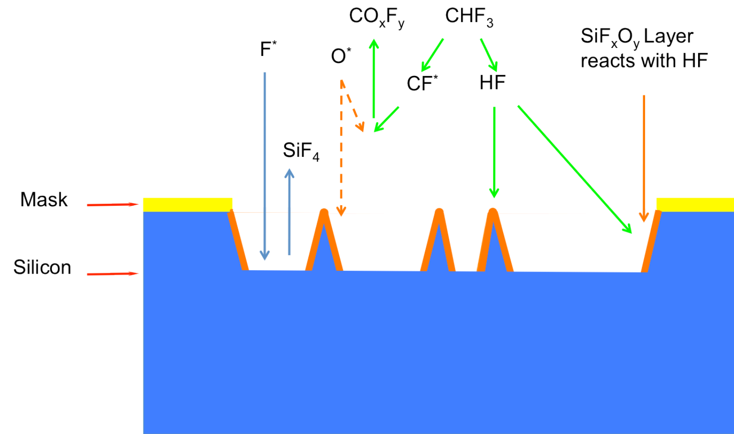

(a) Adding CHF_3 into the etchant.

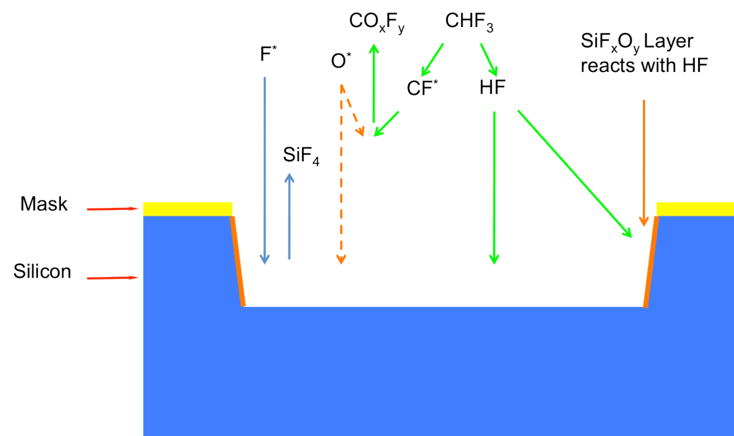

(b) Trench profile changed.

Figure 3.7. Effect of adding CHF_3 into the etchant.

In all the etch attempts, 3 inches <100> wafers were used, and a 200 nm aluminum layer was deposited by sputtering and patterned to work as the mask in the silicon etch. Some attempts and results are list in Table 3-1. The trench depths here were measured using Tencor Alpha Step 500 surface profiler, while the profiles of trenches were measured using Olympus BX51 microscope with digital camera. Table 3-1 shows the plasma etch results. It is a sub-set of all data in Appendix B. Figure 3.8 is an illustration of profile after etching, explaining the terms in Table 3-1.

Table 3-1. Etching experiments.

Etch	1	2	3	4	7	8	10	11
Pressure (mTorr)	50	50	50	50	100	100	50	50
RIE (W)	75	75	50	50	50	50	50	50
ICP (W)	100	100	100	100	100	100	100	100
Time (s)	600	600	600	600	600	600	600	600
CF_4 (sccm)	0	0	0	0	0	0	0	0
SF_6 (sccm)	30	30	30	30	30	30	30	30
O_2 (sccm)	15	15	15	15	15	15	15	15
CHF_3 (sccm)	0	10	0	10	10	20	15	20
Depth (μm)	9.56	15.16	6.58	7.83	6.528	8.458	14.35	15.45
Etch-rate (μm/min)	0.956	1.516	0.658	0.783	0.6528	0.8458	1.435	1.545
W_{mask} (μm)	16	22	14	14	6	14	7	8
Undercut	0	0	0	0	46%	24%	17%	26%
W_{bottom} (μm)	4	2	5	4	4	12	6	4
slope angle	58°	51°	56°	57°	58°	71°	78°	68°
Anisotropy	0.37	0.34	0.32	0.36	0.39	0.65	0.79	0.61

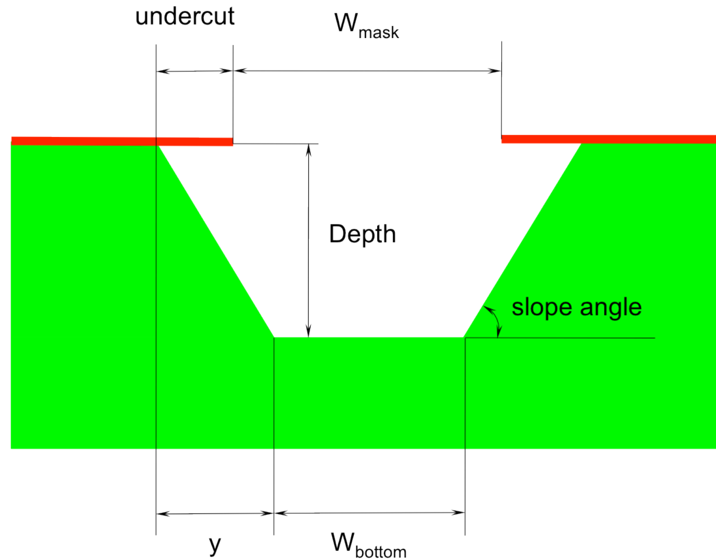

Figure 3.8. Illustration of the profile after etching.

Comparing the first two experiments, CHF_3 gas was introduced into the etchant, which gave a much higher etch-rate and not much difference in the anisotropy. Reducing the RIE from 75 W to 50 W, comparing experiment 3 and 1, the anisotropy actually decreased. That is exactly what was described in the original paper. However, the anisotropy increased a little in experiment 4, where the same recipe was used as experiment 2 except the reduced pressure. That could be a result of error in measurement.

Comparing the experiment 7 and experiment 4, an increased pressure was applied, which should have decrease the anisotropy as described previously in this chapter. However, the measurements showed that the anisotropy actually increased slightly. Then, more CHF_3 was added into the recipe, see experiment 8. A huge boost in the anisotropy was observed in agreement with the original literature. As a result, in experiment 10 more CHF_3 was added to the recipe at a lower pressure, and the anisotropy furthermore increased and reached 0.79. This could be explained by the increased amount of CHF_3 consuming the oxygen in the etchant so that a thinner passivation layer was formed at bottom of the trench.

One more experiment was carried out with even higher CHF_3 ratio at 20 sccm, a decrease in the anisotropy could be observed. That means the passivation layer was heavily etched so that it was too thin on the sidewall. Figure 3.9 demonstrates how anisotropy varies against flow rate of CHF_3.

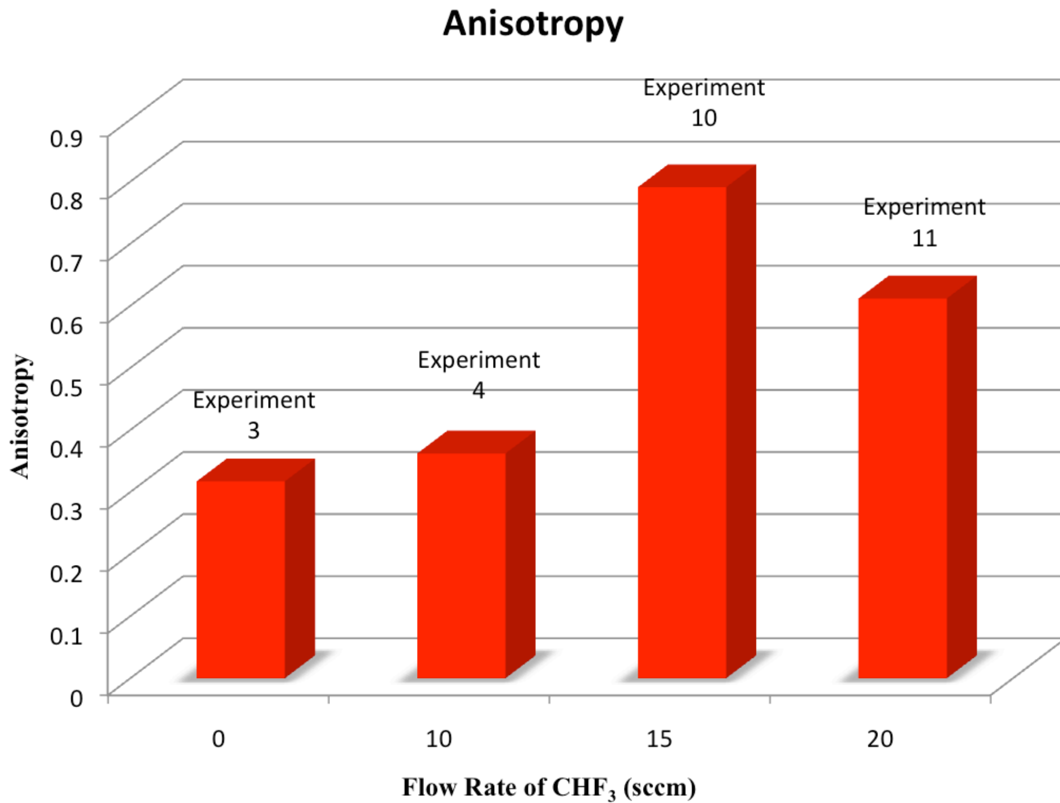

Figure 3.9. Anisotropy against flow rate of CHF_3 for Pressure = 50 mTorr, RIE = 50, ICP = 100, SF_6 = 30 sccm, O_2 = 15 sccm.

Undercut of the mask, as shown in Figure 3.4 (b), can also occur. This is seen in experiment 7,8,10, and 11 in Table 3-1. The measurement was carried out using Olympus BX51 microscope with digital camera with 100× magnification. The resolution of the measurement is around 1 μm due to the limitation of the eyesight. First, sizes of the perforations in the aluminum layer were measured before the plasma etch. The aluminum layer worked as the mask in the plasma etch. After the plasma etch, the aluminum layer was striped away, leave the profiles of etch exposed. Then the widths of the etching

profiles were measured. By subtracting the widths of the perforations of the mask from the widths of the etching profiles, the undercut can be got.

Comparing the experiment 7 and experiment 4, the undercut was introduced by increasing the pressure, which indicates that the fluorine ions were scattered and more fluorine ions could reach the sidewall. Comparing the experiment 10 and experiment 4, the undercut was introduced by increasing the flow rate of CHF_3. Since CHF_3 consumed the oxygen in the etchant, thinner passivation layer was formed on the surface of the profile, and the fluorine ions could easily reach the silicon beneath the passivation layer, which made the profile less positive tapered and increased the anisotropy. A further increasing in flow rate of CHF_3 introduced more undercut but less anisotropy, see experiment 11.

Result Analysis:

An anisotropy of 0.79 was the best that was observed. This could either be a local minimum resulted in by the lacking in attempts or be caused by the limitation of the equipment. One of the potential reasons could be insufficient substrate cooling. The thermal feature of the specific chemical reaction was fully studied by Gilgunn et al. [52]. The temperature on the surface where reaction taking place follows the equation:

$$P_i + P_e = P_r + P_c \tag{3.4}$$

P_i in the equation is the power from the ion bombardment:

$$P_i = en_i v_B V_{bias} S \tag{3.5}$$

where e is the electronic charge, n_i is the ion density, v_B is the Bohm velocity, V_{bias} is the dc bias on the sheath, S is the area where ion bombardment taking place [53]. P_e is the power from the reaction of forming SiF_4:

$$P_e = \alpha E c_{Si} \Delta H S_{react} \tag{3.6}$$

where α is the portion of heat absorb by the wafer, E is the etch rate, c_{si} is the molar density of silicon, ΔH is the heat generated in the reaction, and S_{react} is the surface area of the reaction. P_r is the radiation power of the wafer surface, which is tiny compared to the P_c, the power dissipation to the power-sink of the chamber:

$$P_c = \frac{\Delta T}{R_t} \quad (3.7)$$

where ΔT is the difference in temperature between the wafer and heat-sink while the temperature of the heat-sink could be assumed as a constant, and R_t is the thermal resistance between wafer and heat-sink. From the equation, one can see that during the etching, the temperature of the wafer is mainly depends on the etch rate and the thermal resistivity as the ion bombardment is a constant and reasonable small. With a large R_t, which is exactly the problem of the plasma etcher in our cleanroom, the heat can accumulate in the wafer, and raise the temperature; The balance of the etching reaction will be shifted during the etching process, eventually, reducing the anisotropy.

Chapter 4 Simulation Settings

4.1 Optimization of the Shutter Structure

As discussed in Chapter 3, the sensor fabricated by Wijeweera [20] that works at it resonant frequency suffers from the shift of the resonant frequency of sensor which affects the output of sensor. A solution to this is to design a sensor that does not work at its resonant frequency to magnify the shutter displacement. Works have been done based on the resonant working design, see Mark Roy's thesis [41]. In his simulations, a total shutter displacement equaling 5 μm was picked. This shutter displacement was chosen so that the shutter could cover and uncover the electrodes completely. Figure 4.1 is the illustration of the original sensor and its cross-section [20].

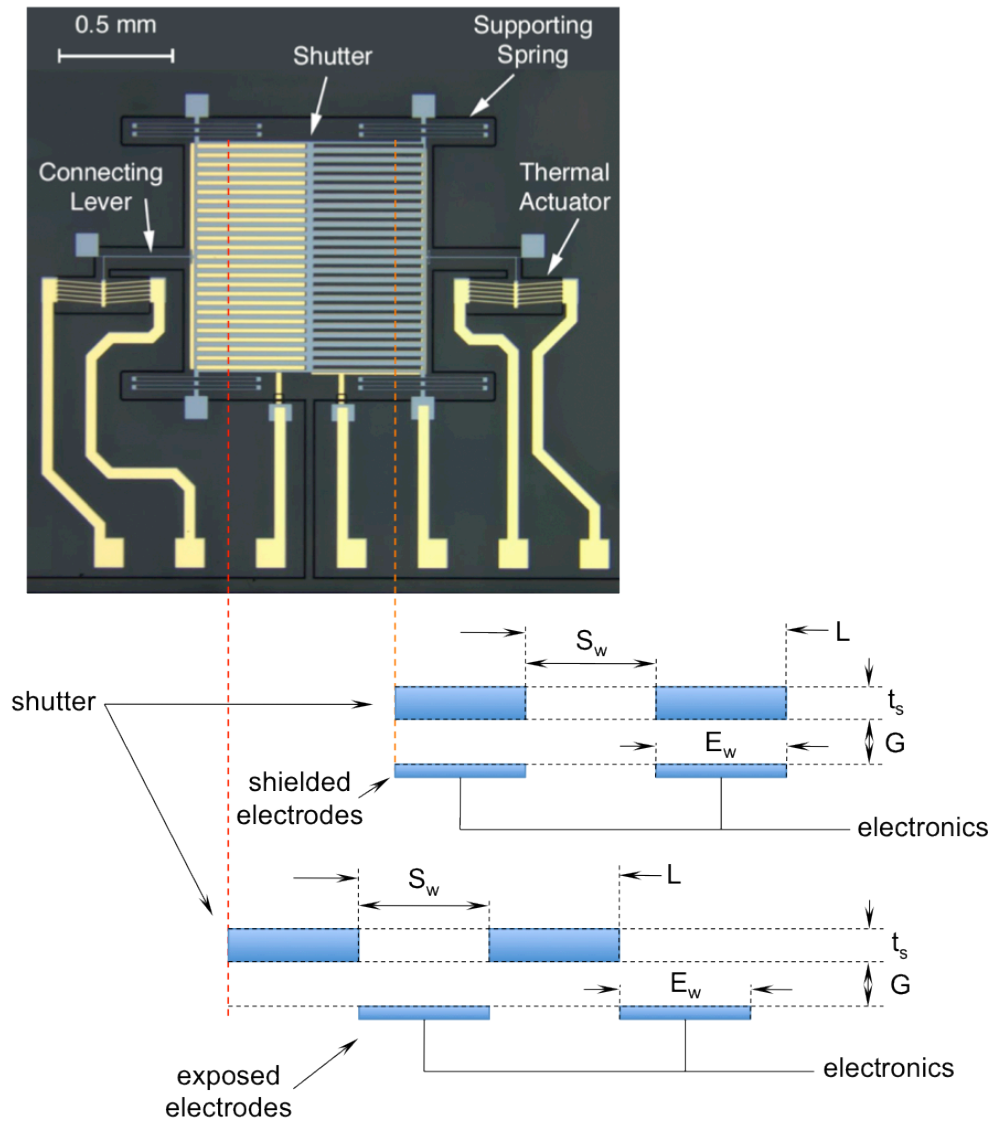

Figure 4.1. The MEFM fabricated by Wijeweera [20] and its cross-section.

This chapter presents simulations of the MEFM operation. The Parameters of S_w, t_s, E_w, and G are studied to determine their effect on the MEFM signal. Therefore, all of four parameters will be fully investigated using FEM simulations. The definitions and simulated ranges of different MEFM design parameters are given in Table 4-1.

Table 4-1. Definition of the MEFM design parameters and the simulated range of each parameter.

Parameter	Definition	Range
L	Shutter perforation repetition period	10 µm
S_w	Width of slit in the shutter	2 µm to 9 µm
E_w	Width of the electrodes	1 µm to 10 µm
t_s	Thickness of the shutter	2 µm to 8 µm
G	Gap between the shutter and electrodes	0.5 µm to 10 µm

Among all these parameters, L corresponds to the total shutter displacement while the other four are arbitary with the condition that S_w and E_w should not be larger than L, see Figure 4.1. With these considerations comes the range of each different parameter in Table 4-1.

4.2 Simulation

FEM simulations were done using COMSOL Multi-physics. The electrostatic interface of the AC/DC module was used. The interface is essentially solving a partial differential equation in 3-D simulations:

$$-\varepsilon_r \varepsilon_0 \nabla^2 V = \rho \tag{4.1}$$

where V is the electric potential, ε_r is the relative permittivity of the material, ε_0 is the permittivity of vacuum, and ρ is the space charge density. While in 2-D simulations, the interface is solving the partial differential equation:

$$-d\varepsilon_r \varepsilon_0 \nabla^2 V = \rho \tag{4.2}$$

where d is the thickness in z direction, V is the electric potential, ε_0 is the permittivity of vacuum, P is the electric polarization vector, and ρ is the space charge density.

Initially, 3 dimensional simulations were done. However, it turned out to be extremely time-consuming and not easy to manipulate the parameters. To overcome all these drawbacks, 2 dimensional simulations were designed and carried out. They offered the advantages of both shorter computation time and good accuracy.

4.2.1 3-D Simulations Set-up

The 3-D simulations were based on the studies done by Chao Gong et al. [54]. In their work, effects of width of slits, thickness of shutter, and the distance between shutter and electrodes on the amount of induced charge on the electrodes were studied by comparing the amount of the induced charge on the exposed electrodes and the maximum amount of charges that could be induced in the same area of the electrode. Similar simulations of the amount of induced charge were carried out to study the effect of S_w, t_s, and G on induced charge and are presented in this section. The following is the set-up of the simulation.

A 200 µm × 200 µm × 50 µm chamber filled with common air was generated. The bottom of the chamber was set to be electrically grounded (Dirichlet boundary), (see Figure 4.2) and the red part indicates the ground. All other boundaries were set to be default (Neumann boundary), that is:

$$n \bullet D = 0 \tag{4.3}$$

where n is the normal of the boundary, D is the electric displacement field. The sensor would be placed in the chamber.

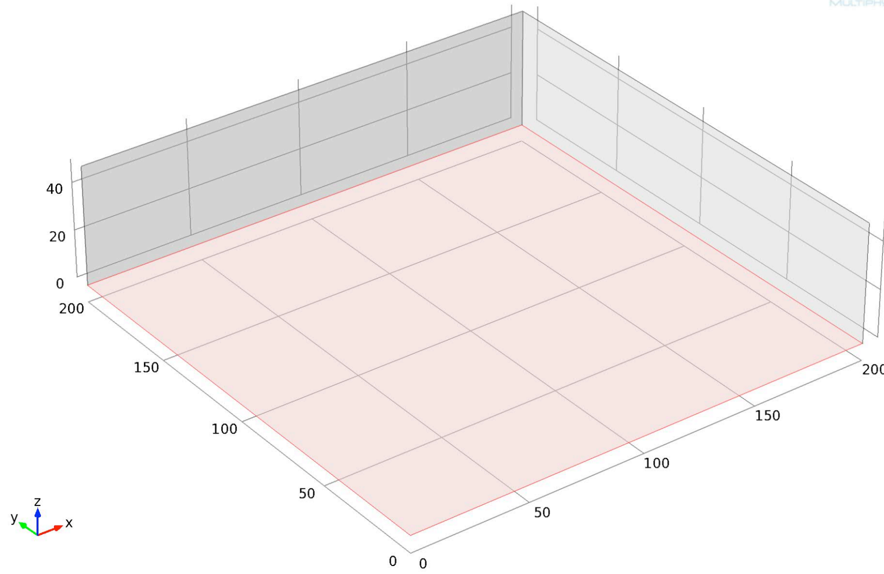

Figure 4.2. Air Chamber.

The parallel field approximation is valid here, for the HVDC transmitting line is fitted at approximately ten meters above the ground, while the size of the sensor is around few square millimeters, and is placed closed to the ground. Therefore, in the simulation, an electric field with uniform field strength could properly simulate the real incident field on the sensor. A uniform electric field along the height with 0.1 V/m in strength was required in the chamber where the sensor placed in the simulations. In order to generate this uniform electric field, an artificial air chamber is needed to mimic the distance between transmission line and the sensor. In my simulations, a 200 μm × 200 μm × 50 μm chamber was used, as shown in Figure 4.3. It is known that, when two layers of insulators stacks together, the field distribution within the insulators alters according to the ε_r, and the field strength follows the Gauss's Law:

$$\oint_S D \bullet dS = \int_V \rho dV \tag{4.4}$$

As the charge density on the boundary in between is zero, the field strength perpendicular to the boundary could be derived:

$$n \bullet (\varepsilon_r^1 E_1 - \varepsilon_r^2 E_2) = 0 \tag{4.5}$$

where ε_r^1 is the relative permittivity in the artificial area and ε_r^2, approximately equals 1, is the relative permittivity in the chamber. When a 0.5 V potential was applied on the top

boundary of the chamber, the red part in Figure 4.3, the ε_r^2 can be calculated and it should equal 1×10^{-5}. All other boundaries were also set to be default, which is no charge is on the boundary. As a result, the boundary condition of the partial differential equation became a mix boundary condition.

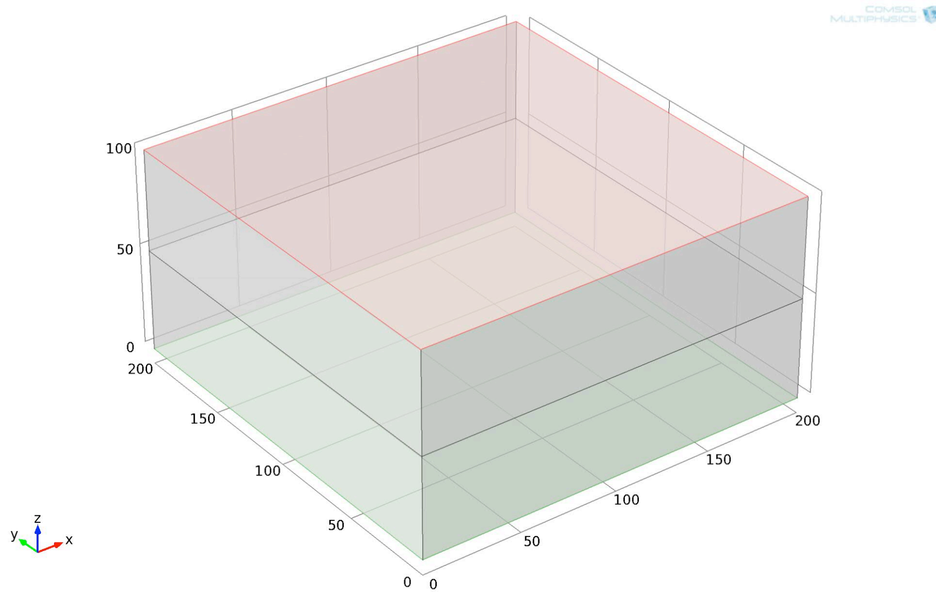

Figure 4.3. Structure with artificial air chamber on the top.

A 200 μm × 200 μm size shutter was generated within the chamber; see Figure 4.4, while the thickness was calculated according to the width of the slits in the shutter. The size of the shutter should be carefully designed so that the total size of the structure won't be too large. The surface of the shutter was set to be gold and electrically grounded, while the body of the shutter was single crystal silicon.

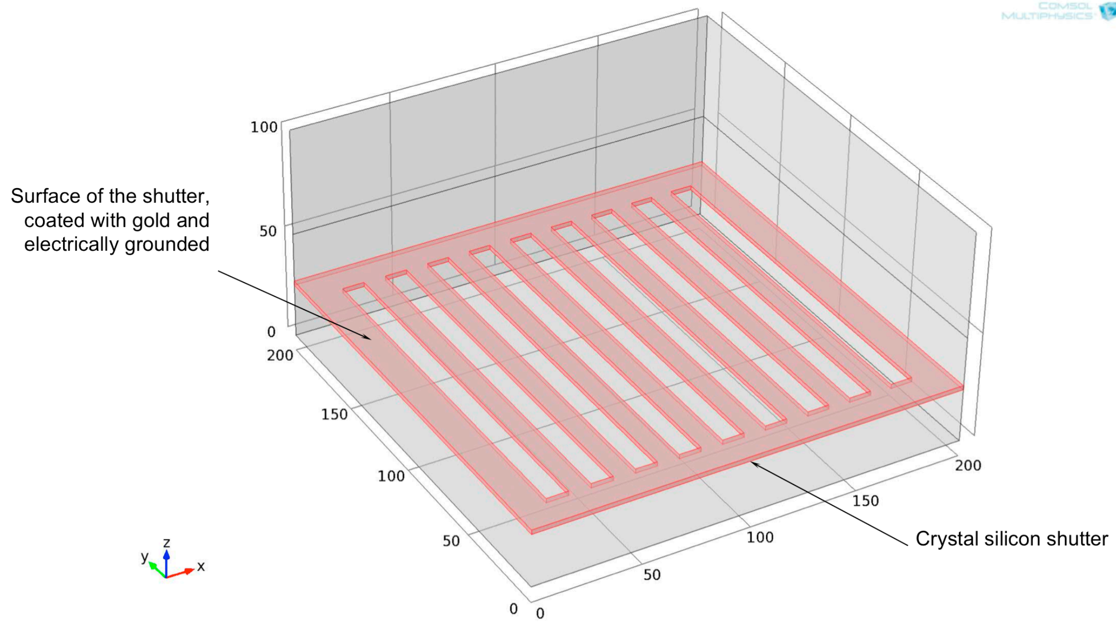

Figure 4.4. Shutter in 3-D simulation.

The electrodes were fitted beneath and had the same size of the slits in the shutter. The gap between electrodes and the shutter was set to be one of the simulation parameters therefore would be changed through series of the simulations. In Figure 4.5, only exposed electrodes are shown, see the red part. The electrodes were set to be gold and also electrically grounded so that the amount of induced charge could be calculated later on.

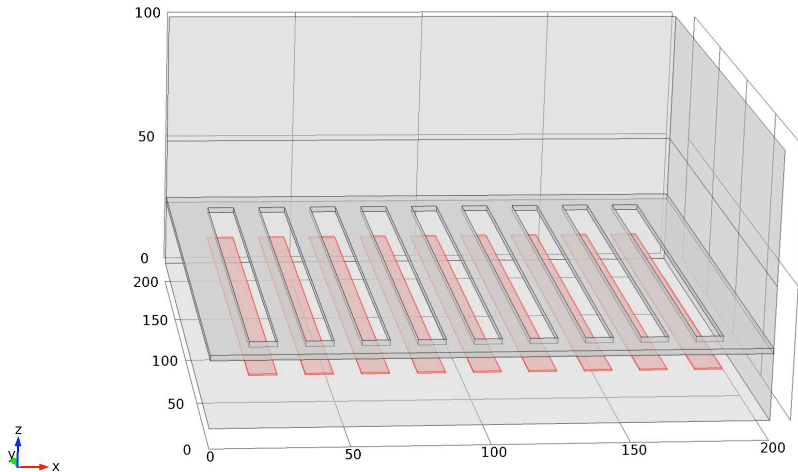

Figure 4.5. Electrodes beneath the shutter.

It is reasonable to create a high meshing density area to define the part where finer meshing is applied. By applying mesh refinement on these specific areas, a more coarse mesh could be applied on the parts of the structure where the field calculation is not critical to the result. Therefore, the total mesh density will be reduced, speeding up the simulations without any penalty on the accuracy.

Mesh refinement is one of the options in meshing part of COMSOL Multi-physics. When regular refinement is selected, the COMSOL Multi-physics will divide each element generated into four triangular elements of the same shape in 2-D or eight tetrahedral elements in 3-D [55]. In every simulation listed here, regular refinement was used. The area was filled with common air with $\varepsilon_r = 1$, see the red part in Figure 4.6.

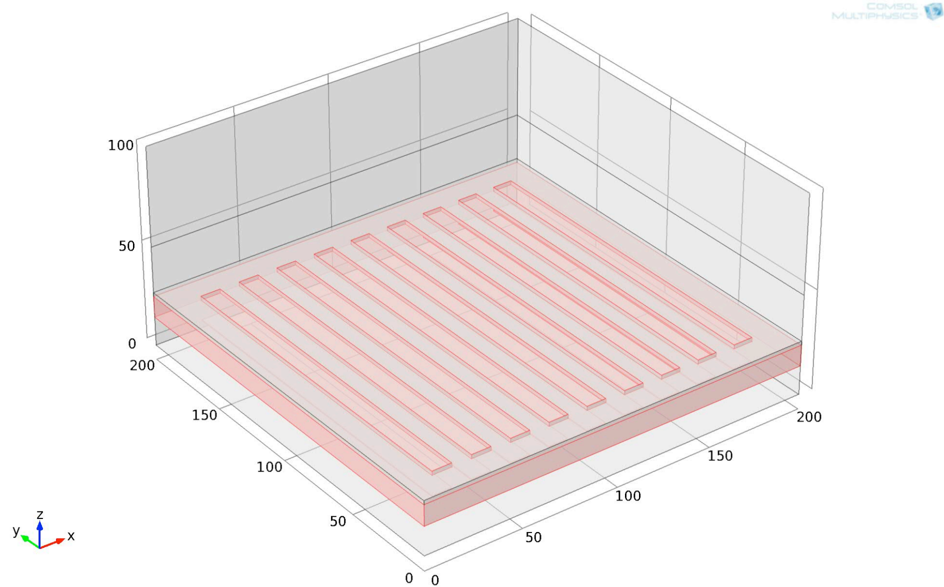

Figure 4.6. High mesh density area.

4.2.2 Results of 3-D simulations

As the 3-D simulations here were based on the study done by Chao Gong et al. [54], thus, the result of those simulations should be similar to the their results if the simulations were carried out properly.

The result of the 3-D simulation is given in the Figure 4.7 (a), while Figure 4.7(b) shows the result of the similar simulation done by Chao Gong et al.. The correspondence between parameters is given in the Table 4-2.

Table 4-2. Correspondence of parameters.

Parameters	Parameters used here	Parameter used by Chao
Width of slit in shutter	S_w	d
Shutter thickness	t_s	t
Gap between shutter and electrodes	G	D
Amount of induced charge	q	q
Amount of induced charge ideal	Q	Q

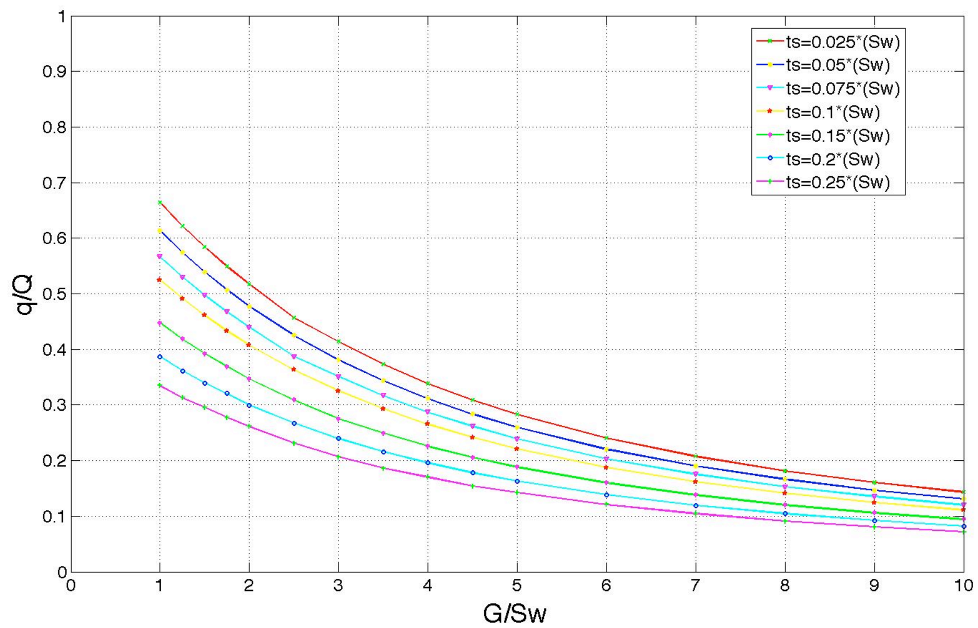

Figure 4.7 (a) q-d curves from 3-D simulations.

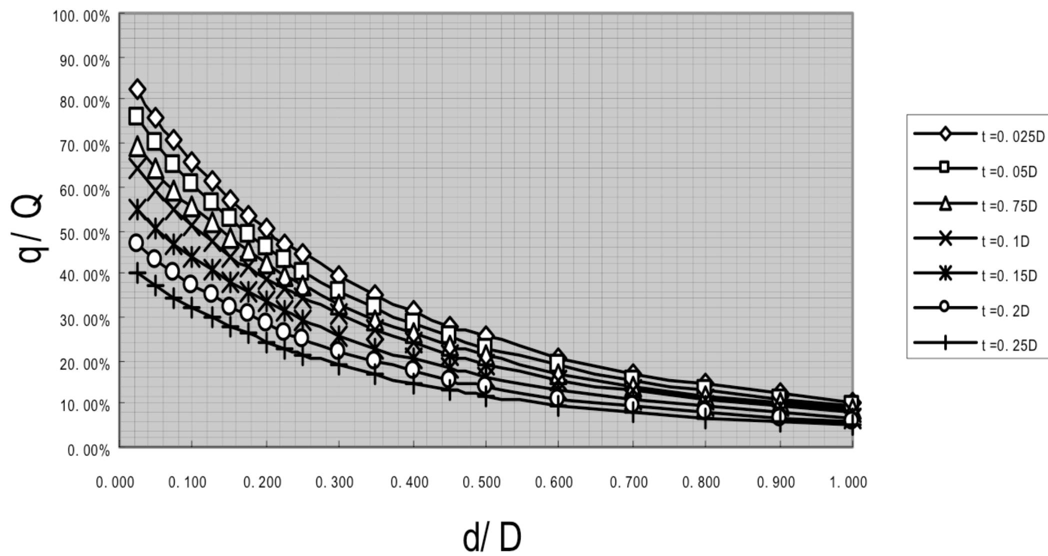

Chao Gong, Shanhong Xia, Kai Deng, Qiang Bai, Shaofeng Chen, "Design and Simulation of Miniature Vibrating Electric Field Sensors", IEEE, 2004
©2004, IEEE

Figure 4.7 (b) q-d curves of the parallel-vibration EFSs [54].

From Figure 4.7 (a), it is clear that, with a fix S_w, increasing G will cause a reduction in the total amount of induced charge on the exposed electrodes. While, a large t_s results in a less amount of induced charge on the exposed electrodes.

The two plots agree with each other strongly. The difference is within few percent, and the similarity is strong enough to prove the correction of the 3-D simulations.

4.2.3 Difficulties of 3-D simulations

Although the 3-D simulation works perfectly with the structure given above, the drawbacks are also apparent.

- Time consumption

Each 3-D simulation takes approximately 2 to 8 hours to complete depending on the structure size and the mesh density. This does not make possible a thorough investigation of all the structure parameters as tens of thousands simulations are needed for the study in this thesis.

- Converging problem

Since a structure with small features is being simulated, convergence could be another problem that should be considered. An extremely fine meshing is required for accuracy. However, by applying a fine meshing on the structure, the number of elements in 3-D simulations increases dramatically and the computing time can be devastating.

- MATLAB interface is not applicable

The MATLAB interface for COMSOL 4 has a defect that a boundary and domain detecting function is not available. Without the boundary and domain detection function, the interface is not reliable. Therefore, can not be used for 24 thousand simulations.

4.2.4 2-D Simulation

2-D simulation is also valid for the sensor structure, as the width of the slit, typically around 5 to 10 µm in the new generation sensor design, is quite small compared the length of the slit, which is around 450 µm. Which makes the 2-D approximation available along the cutting line seen in Figure 4.1. As a result, a series of two-dimensional electrostatic simulations were used to analyze the structural properties of the MEFM. The 2-D simulations have several advantages comparing to the 3-D counterparts.

a). 2-D simulations take much less time to solve in comparison to 3-D ones.

As a result, a large quantity of simulations could be done within a reasonable time span to give a thorough investigation of all different parameters of the structure. A total of 24,000 simulations were done within few weeks.

b). MATLAB interface is available for generating the simulations automatically.

For each simulation, a total of 9 parameters, including structure sizes and meshing density, have to be set. With the help of the MATLAB interface, all the parameters could be automatically set while applying the all boundary and domain conditions. A domain and boundary detecting program developed by Mark Roy was used to make sure that all the conditions could be applied properly to the various structures.

c). 2-D simulations give a good approximation of the 3-D simulations.

Figure 4.8 shows the ratio between the induced charge on the exposed electrodes (q) and the maximum amount of charges that can be induced on the same area (Q) over the gap between shutter and electrodes with 2.5 μm shutter thickness. Both 3-D and 2-D results are given in the figure. It is clear that both results show a strong similarity with each other, and the difference is within few percent.

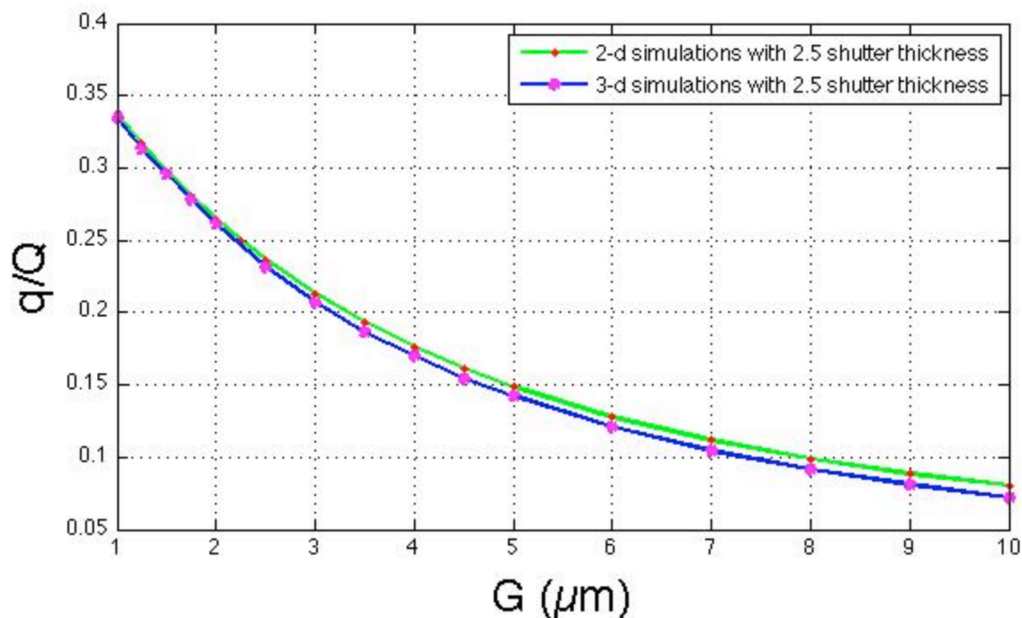

Figure 4.8. Results of 2-D and 3-D simulations.

4.2.5 2-D Simulation Set-up

A 640 µm × 100 µm chamber was generated and was filled with common air with $\varepsilon_r = 1$. The bottom edge of the chamber was set to be electrically grounded, marked in red in the Figure 4.9. While other boundaries are set to be default that no charge is on the boundaries.

Figure 4.9. Chamber where the sensor was placed.

A 640 µm × 100 µm block of artificial air, illustrated in Figure 4.10, was generated above the main chamber. Similar to the one in 3-D simulations, a 1 V voltage is applied on the top boundary of the block and the ε_r is set to be 1×10^{-5} to mimic the field source 10 m away. All other boundaries are set to be charge free, which again made the boundary condition of the partial differential equation a mixed boundary condition. As the total area of the sensor is small, 1 mm × 1 mm, compared to the distance from the transmission line, the parallel electric field approximation is valid.

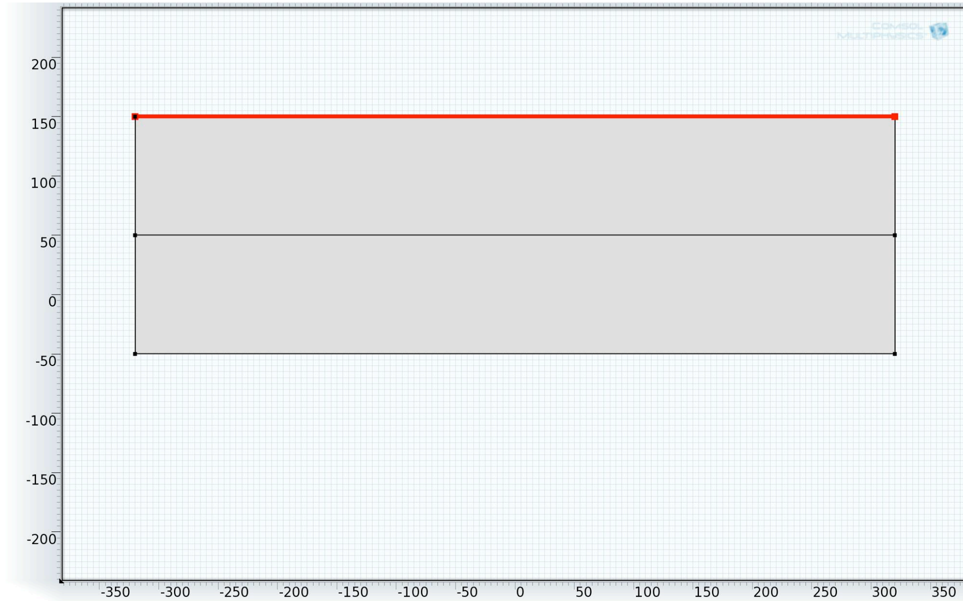

Figure 4.10. Chamber filled with artificial air.

A silicon shutter was generated by three steps, see the blue part in the Figure 4.11. The shutter possesses a center block which was 60 μm in width to reduce the interference of two sets of electrodes, two arrays of shutter blocks in the perforated region and two solid ends of the shutter. The top boundary of it was set to be gold, which would give a better electrical grounding.

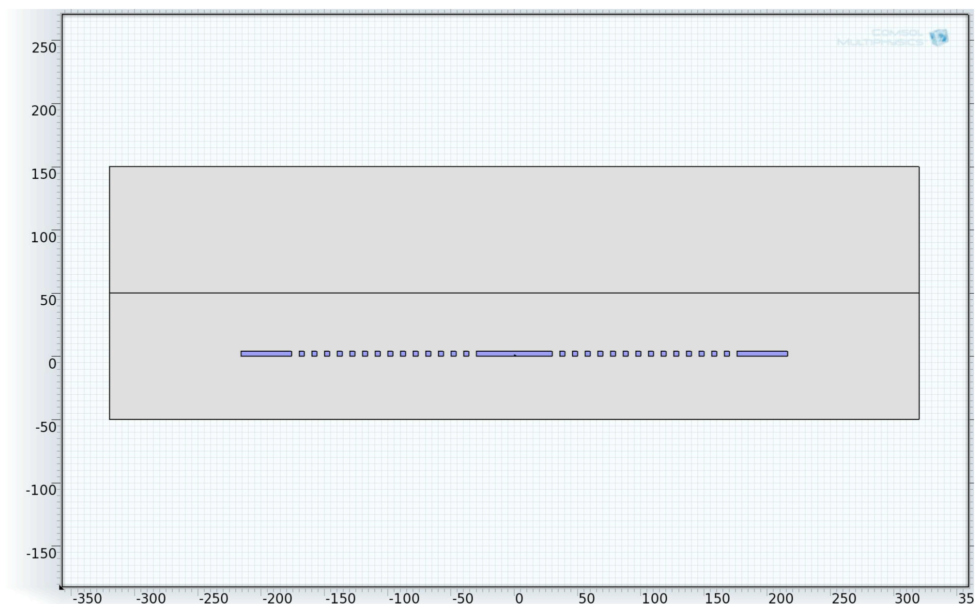

Figure 4.11. Shutter with rectangular cross-section.

Two arrays of electrodes, blue parts in Figure 4.12, were generated so that one is covered and another is blocked by the shutter. Both arrays were grounded and set to be gold, as a result the induced charge on the surface of the electrodes follows the Equation 2.10.

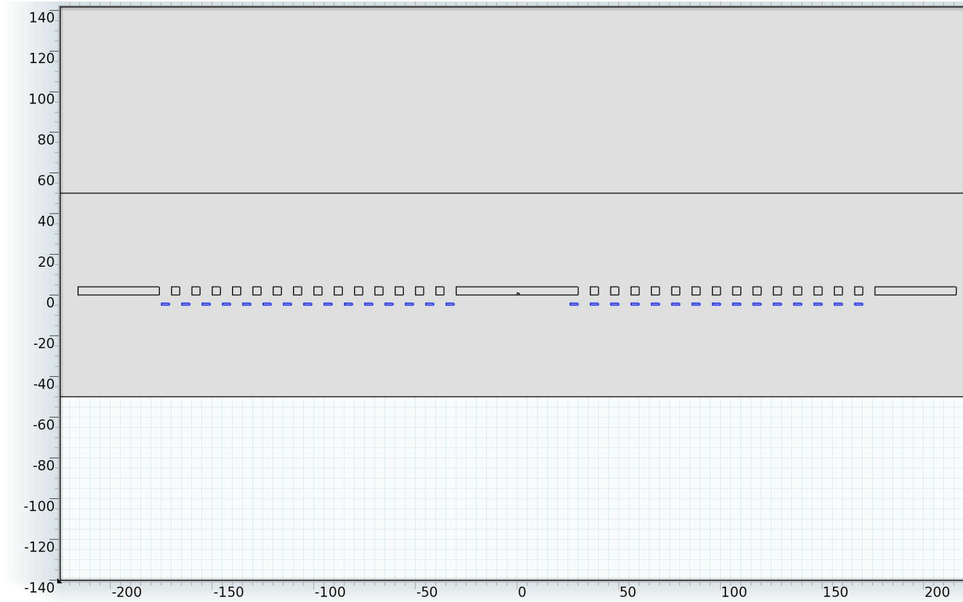

Figure 4.12. Electrodes

A 630 µm × 20 µm Pyrex substrate was generated and the bottom of it was grounded, (see the yellow line in Figure 4.13), according to the MicraGEM fabrication process, see the red part in the Figure 4.13.

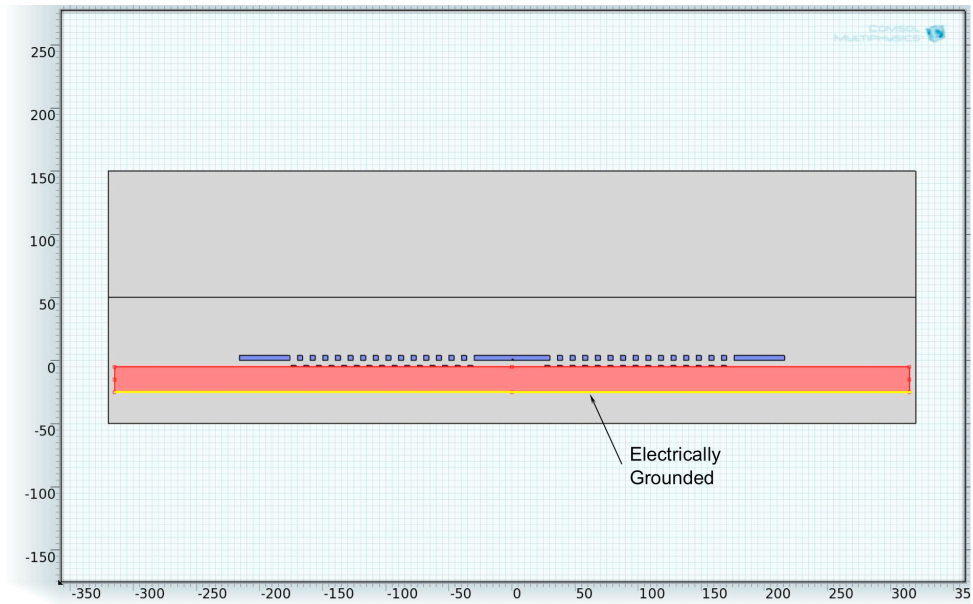

Figure 4.13. Pyrex substrate

High mesh density area was generated, shown as the red part in Figure 4.14, so that later on mesh refinement could be applied on the area. It is critical to the actuation of the simulation as will be discussed.

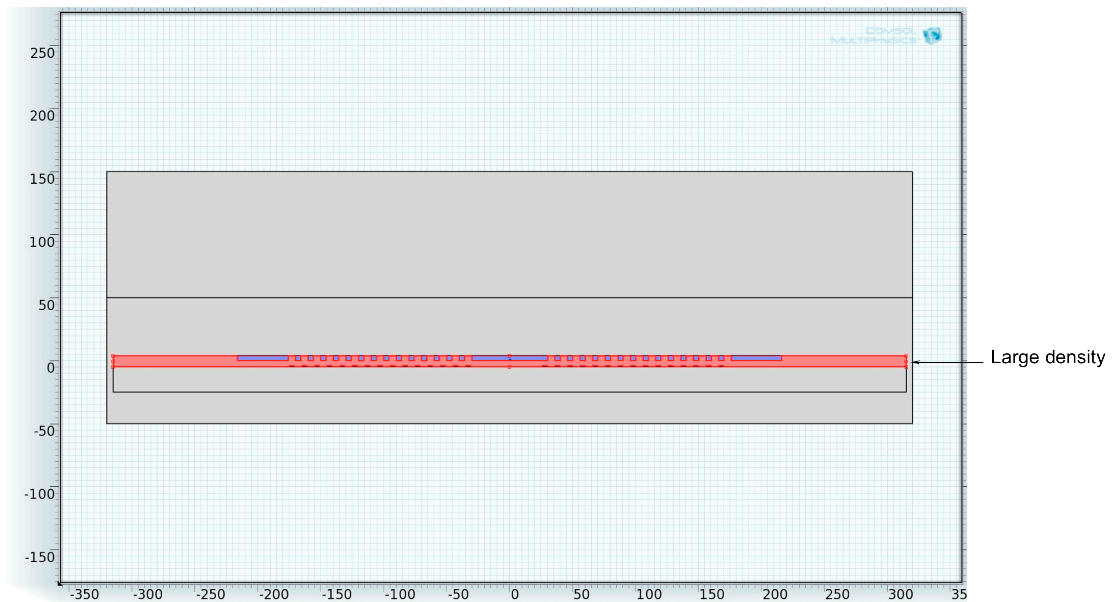

Figure 4.14. Large mesh density area (red color), all other regions are low density.

4.2.6 Simulation parameters

a. Simulation size vs. Computation time

The structure size is one of those fundamental variables that will affect the simulation time. As a repeating structure, it is not necessary to simulate a full size sensor with approximately 100 electrodes on each set. A simplified structure could greatly shrink the simulation size.

Figure 4.15 shows the computation time of each 2-D simulation over the number of perforation repetitions (number of slits). Noticing that the total shutter size is a function of numbers of slits in the shutter, it is apparent that less slits, thus smaller shutter, will give a shorter computation time.

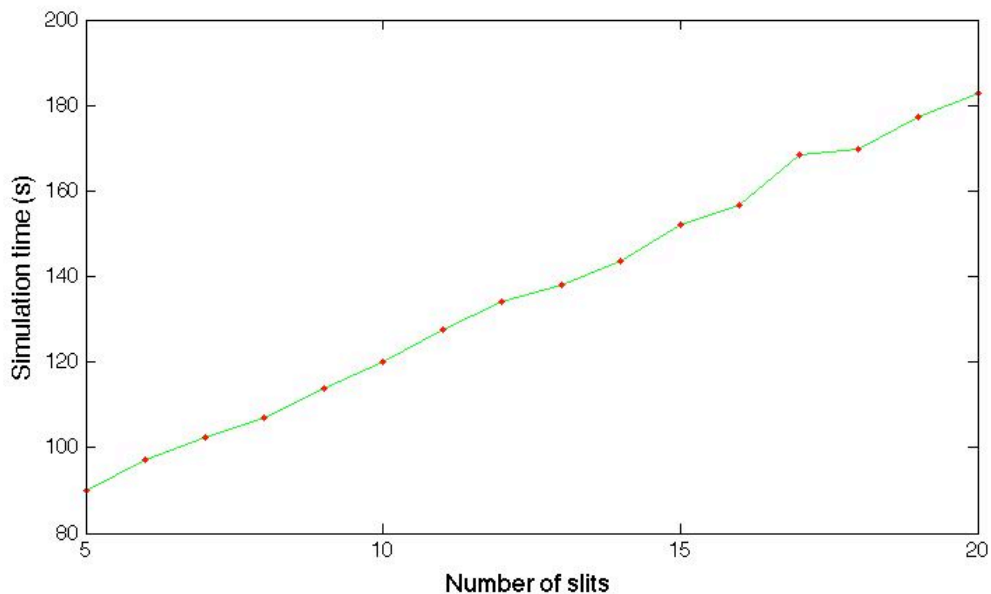

Figure 4.15. Number of slits vs. simulation time.

However, as shown in the Figure 4.16, the electric field strength is not stable on the first few slits at each side, the field strength increases until reaching a constant value after several slits, thus a structure without enough electrodes will lose its accuracy. From the Figure 4.16, it is obvious that the electric field strength at the fourth electrodes from

each edge differs from those in the center of the electrode array. Therefore, at least 7 electrodes were simulated. However, in my simulations, 15 slits on each side were used for better accuracy.

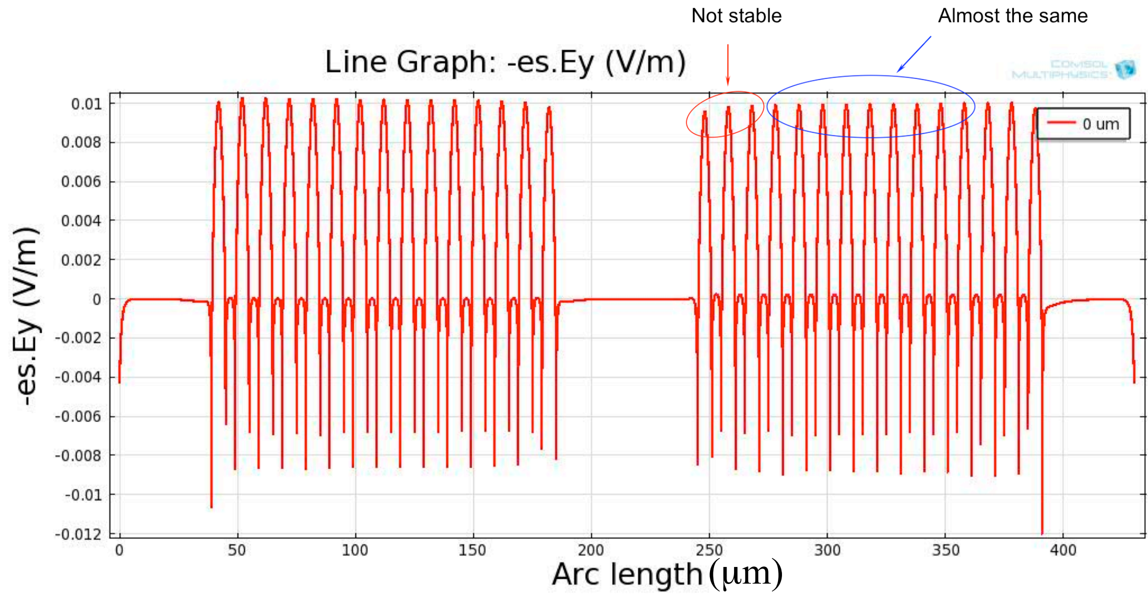

Figure 4.16 (a) Field strength at bottom of shutter.

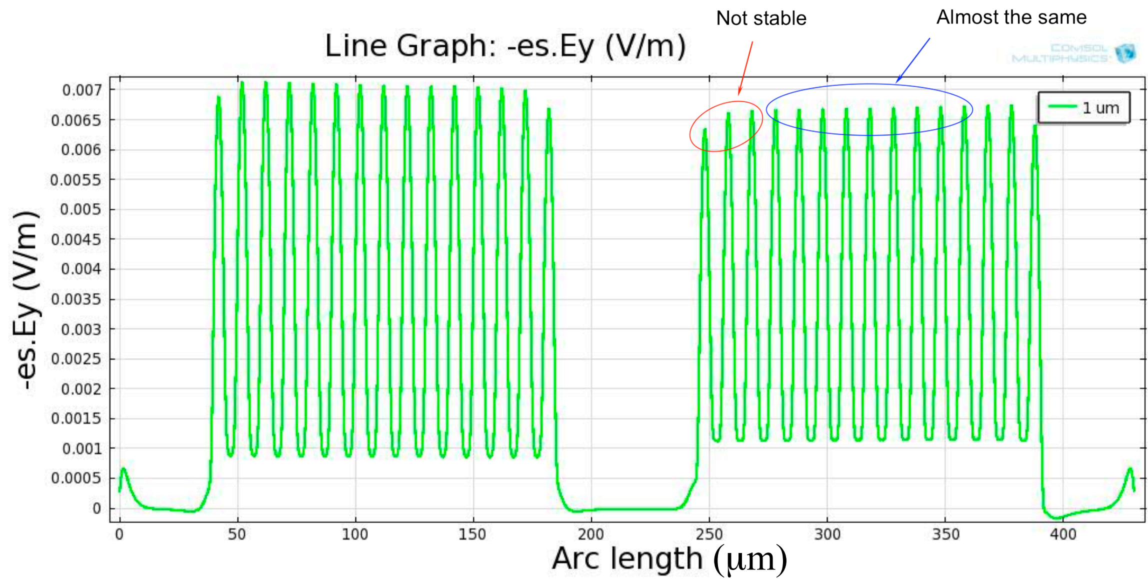

Figure 4.16 (b). Field strength at 1um away from the bottom of the shutter.

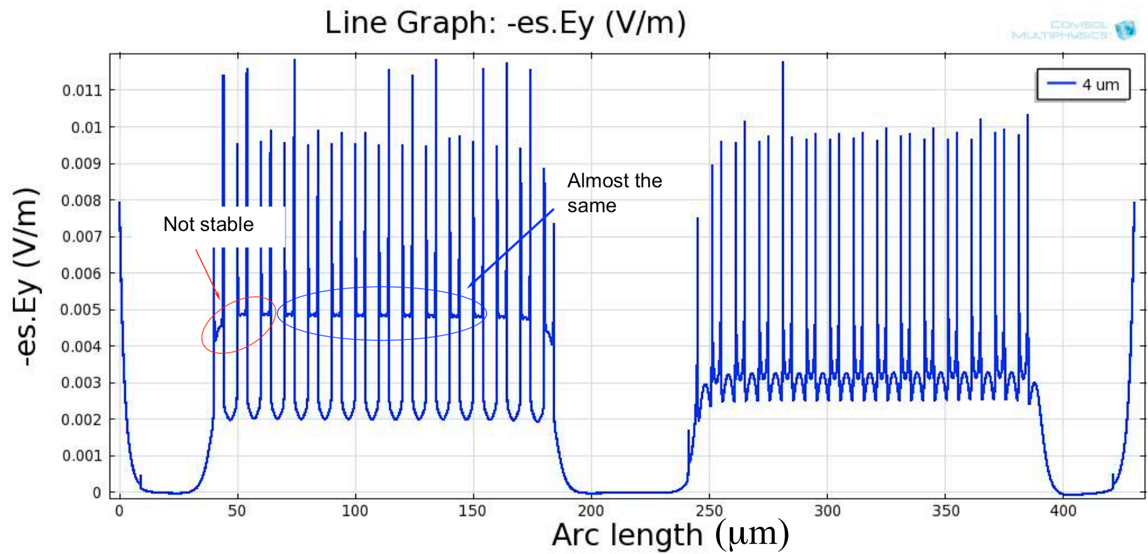

Figure 4.16 (c) Field strength at the top of electrodes.

b. Effect of mesh density on computation Time

Figure 4.17 shows the simulation time as a function of mesh density. The mesh density 1 in Figure 4.17 indicates the mesh density that was applied on the shutter, high mesh density area, and the electrodes in the 2-D simulations, while the mesh density 2 stands for the mesh density that applied on the other domains of the 2-D simulations. In my simulations, the real size of elements generated in meshing varies form one tenth of the mesh density applied to the mesh density, e.g. 1 µm to 10 µm when mesh density equals 10 µm. Besides, refines were also applied on the high mesh density area in the 2-D simulations to further increase the meshing density in that specific domain. The refine of mesh of COMSOL Multi-physics works that the elements generated in the meshing will be divided into new elements based on the refine rate. The number of the new elements equals 2 to the power of refine rate. That is 2 new elements when refine rate equals 1 and 4 new elements when refine rate equals 2 and so on. With different mesh density, the simulation time could vary from a few tens of seconds to thousands of seconds.

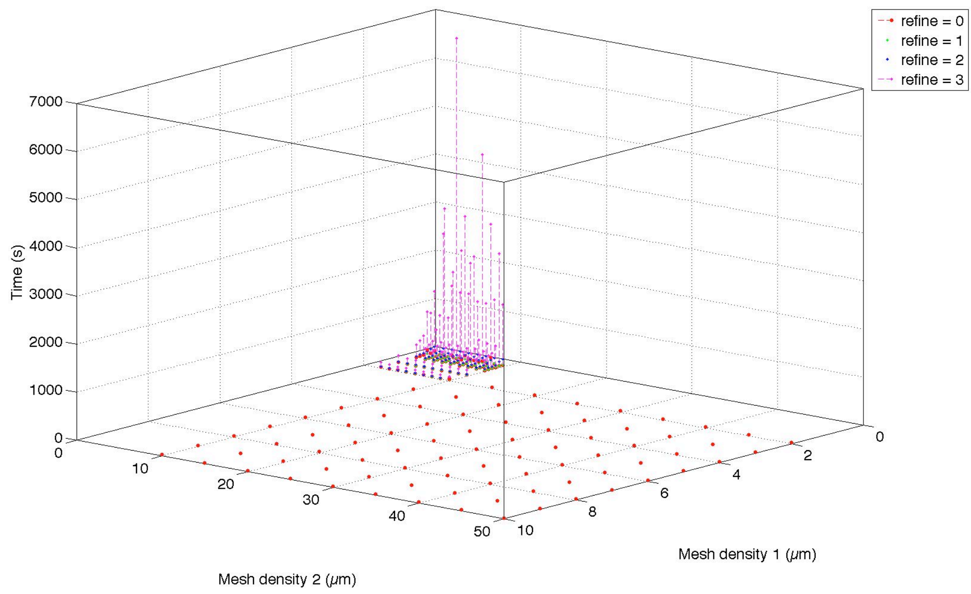

Figure 4.17. Time of each simulation vs. mesh density.

c. Effect of mesh density on simulation results

Two plots of Figure 4.18 below indicate that with the same meshing refine, the induced charge is a function of the density of mesh.

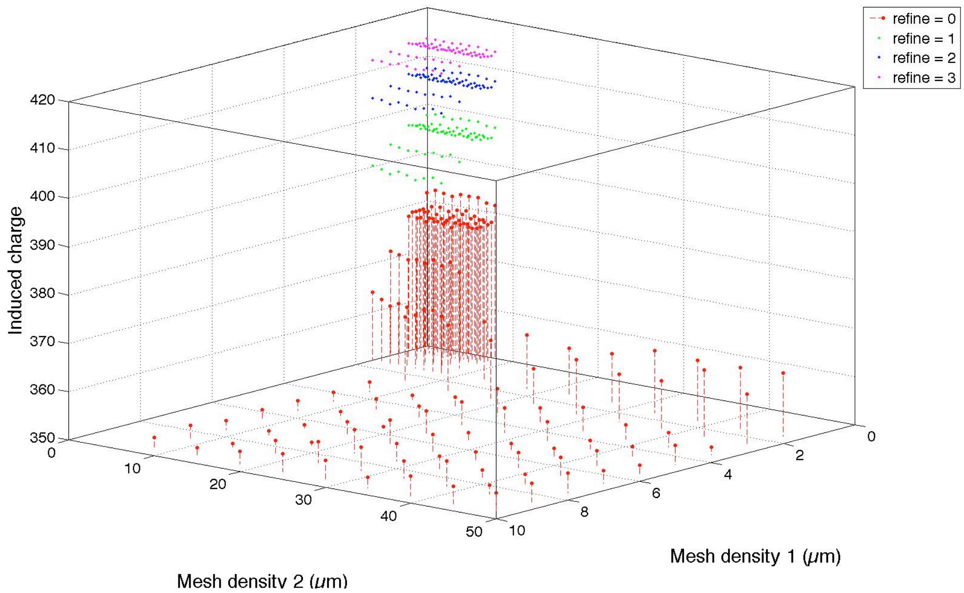

Figure 4.18 (a) Induced charge on the exposed electrodes vs. mesh density.

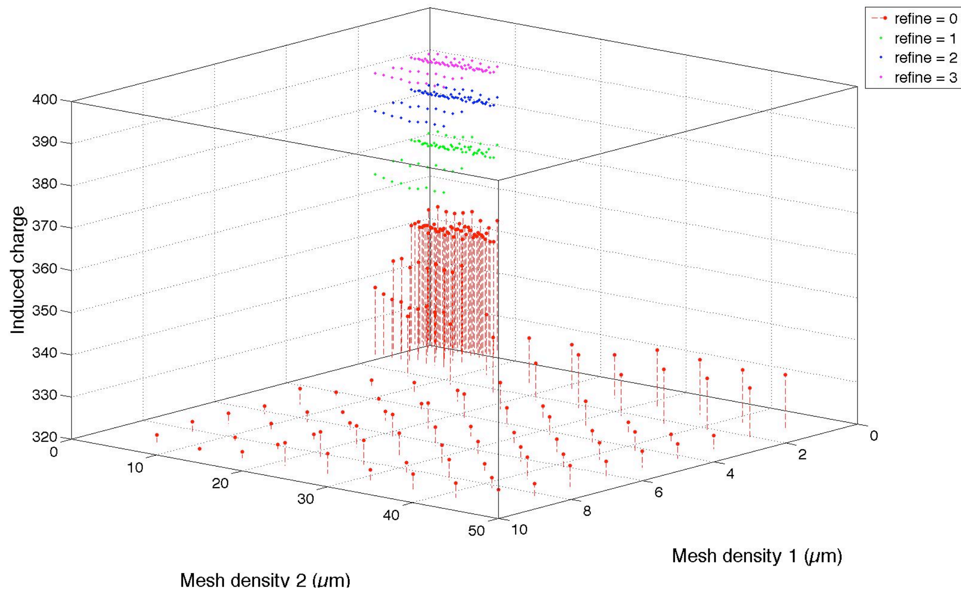

Figure 4.18 (b) Induced charge on the shielded electrodes vs. mesh density.

The difference in the amount of induced charge on two sets of electrodes over different mesh density when refine rate equals 0 is given in the Table 4-3:

Table 4-3. Mesh density and difference in the amount of induced charge

Mesh density 1	Mesh density 2	I. C. on exposed 1	I. C. on exposed 2	Difference	Percent
2 → 10	10	365.6817	353.7722	11.9095	3.4
2	10 → 50	365.6817	364.5724	1.1093	0.3
0.5 → 2	2	383.2787	365.6817	17.597	4.8
0.5	2 → 10	383.2787	383.3197	0.041	0.01
		I. C. on shielded 1	I. C. on shielded 2		
2 → 10	10	336.0103	324.7824	11.2279	3.4
2	10 → 50	336.0103	336.1857	0.1754	0.05
0.5 → 2	2	353.8847	338.9247	14.96	4.4
0.5	2 → 10	353.8847	354.2987	0.414	0.11

While the difference between meshing with various refine rates are given in Table 4-4 (finest meshing is used):

Table 4-4. Refine rate and difference in the amount of induced charge.

Refine rate	I.C. on exposed 1	I.C. on exposed 2	Difference	Percent
0 → 1	384.2083	399.9291	15.7208	4.09
1 → 2	399.9291	409.4352	9.5061	2.38
2 → 3	409.4352	415.4078	5.9726	1.46
	I.C. on shielded 1	I.C. on shielded 2	Difference	Percent
0 → 1	355.2951	372.9564	17.6613	4.97
1 → 2	372.9564	384.2209	11.2645	3.02
2 → 3	384.2209	391.4604	7.2395	1.88

From Table 4-3, it is obvious that when having a fixed refine rate, the result mainly depends on the mesh density 1 that is the mesh density applied on the shutter, electrodes and the large mesh density area. From Table 4-4, when have mesh density 1 and mesh density 2 fix, the result is correspondent to the refine rate.

In the actual simulations, mesh density 1 equaling 1 µm, mesh density 2 equaling 5 µm, and refine rate equaling 3 were picked. The reason of those parameters is mainly a balance of accuracy and computation time.

4.2.7 2-D Results

The results of 2-D simulations will be presented and fully discussed in the chapter 5 along with the results from simulations of alternatives of the conventional MEFM design.

Chapter 5 2-D Result Analysis

In this chapter, the parameters of the shutter design of the MEFM will be discussed. The following parameters were studied: width of slit, electrodes width, shutter thickness and gap between shutter and electrodes, based on 2-D simulations. The range of each parameter is given in Table 4-1. In each simulation, only one of the four parameters was changed while other three were fixed. Also, new designs other than conventional MEFM design will be presented here as an alternative. At the end of the chapter, the effect of a guard ring under the shutter at its periphery will also be discussed.

In this chapter, only some of the total 24,000 simulations are plotted. They are the ones that with the parameters selected according to the experience of the previous simulations and real fabrication in our cleanroom, see chapter 3. Width of slit (S_w), electrodes width (E_w), shutter thickness (t_s) and gap (G) are set at 6 µm, 4 µm, 4 µm and 4 µm respectively, while the applied field strength equals 0.1 V/m.

5.1 Grounded Shutter Design

Width of Slit (S_w):

Figure 5.1 shows that the induced charge on the electrodes increases with increasing width of slit in the shutter. Though, on each set of the electrodes, the amount of induced charge increases dramatically, from 0 to around 1800 when the width of slit increasing from 2 µm to 9 µm, the absolute in the difference does not increase that much.

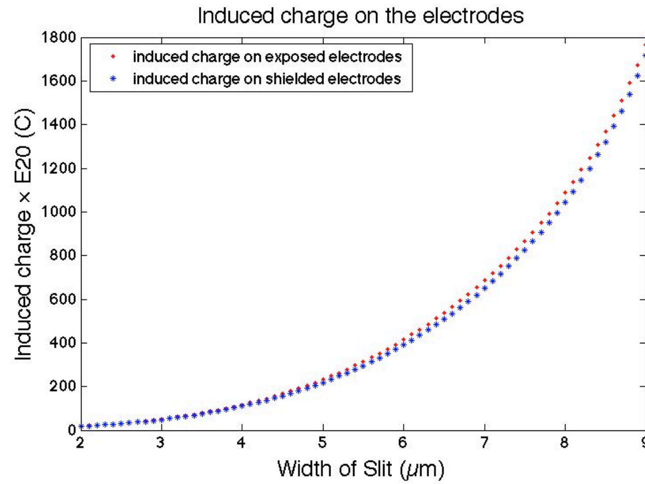

(a) The amount of the induced charge on the electrodes

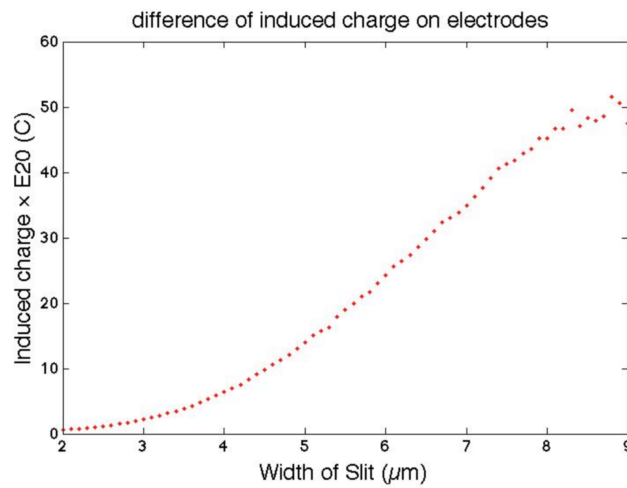

(b) Difference in the amount of the induced charge

Figure 5.1. Effects of width of slit. E_w = 4 μm, t_s = 4 μm, G = 4 μm. (Grounded shutter design with a rectangular cross-section)

Electrode Width (E_w):

Figure 5.2(a) shows that, wider electrodes, thus larger surface area, provide more induced charge on each set of the electrodes. However, Figure 5.2 (b) shows that the difference in the induced charge on two sets of electrodes, on contrary, decreases when

the width of electrodes increases. At the left end of the line in Figure 5.2(b) we see that the difference reaches its maximum when the width of electrodes is between 2 μm and 3 μm.

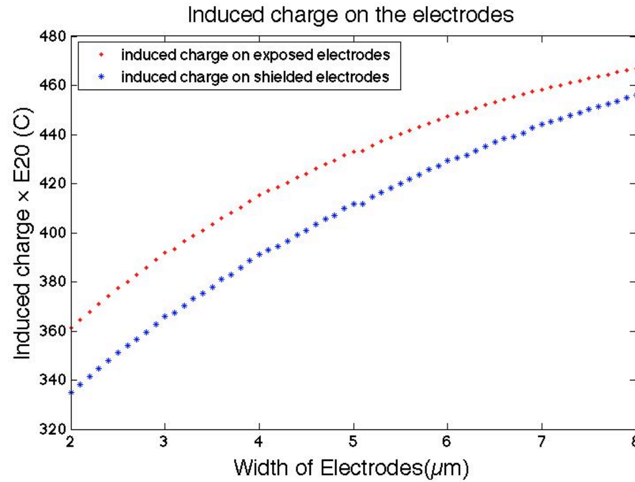

(a) The amount of the induced charge on the electrodes

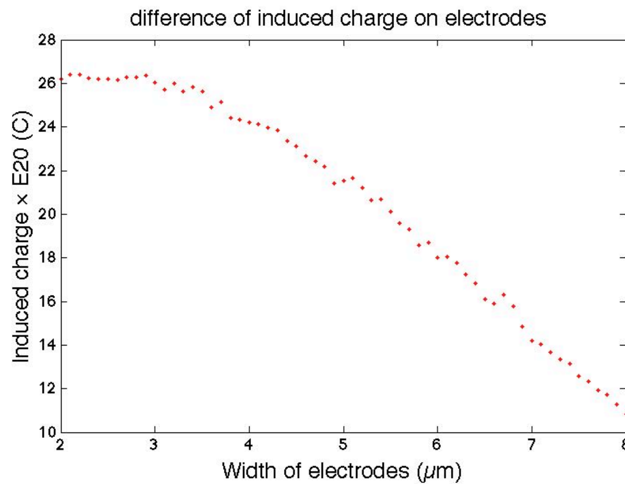

(b) Difference in the amount of the induced charge

Figure 5.2. Effects of electrodes width on induced charge. S_w = 6 μm, t_s = 4 μm, G = 4 μm. (Grounded shutter design with a rectangular cross-section)

Shutter Thickness (t_s):

The shutter thickness is one of the most critical parameters of the shutter as, (see the Figure 5.3), because the field passing the shutter is a function of the inverse of the shutter thickness. A slight change in the shutter thickness can make huge difference on induced charge on each set of the electrodes. Furthermore, the amount of induced charge on the exposed electrodes tends to shrink faster than on the shielded electrodes. As a result, in Figure 5.3 (b), the amount of induced charge falls dramatically from around 130 to almost 0 when the shutter thickness varies from 1 μm to 10 μm. Therefore, a thin shutter is desired if available in the real fabrication process.

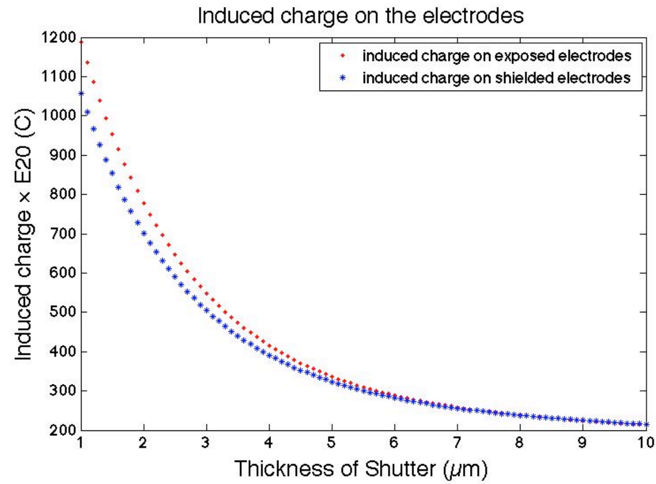

(a) The amount of the induced charge on the electrodes

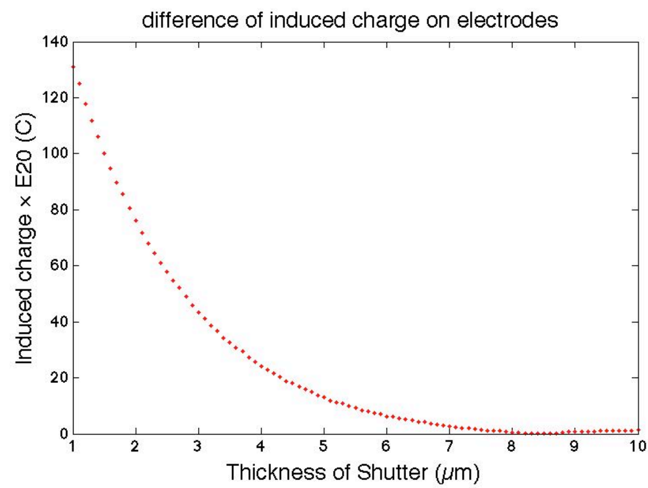

(b) Difference in the amount of the induced charge

Figure 5.3. Shutter thickness vs. induced charge. S_w = 6 μm, E_w = 4 μm, G = 4 μm. (Grounded shutter design with a rectangular cross-section)

Gap between Shutter and Electrodes (G):

The gap between the shutter and the electrodes is another critical parameter controlling the amount of induced charge on two sets of electrodes. Generally, the difference in the amount induced charge on two sets of electrodes decreases when the gap increases. However, notice the inflection point at around 1 μm in Figure 5.4 (b), that's because that the relative permittivity of the silicon is greatly larger than that of the air, part of the fringing field penetrating through the slits will couple into the silicon bulk of the shutter, there will be higher electric field strength at the bottom of the silicon bulk, which leads to an increase in the induced charge on the shielded electrodes and a decrease in the difference. This effect could only be observed when the electrodes are close enough to the shutter, say, less than 1 μm. From Figure 5.4 (b), a small gap, around 1 μm to 2 μm, is optimal.

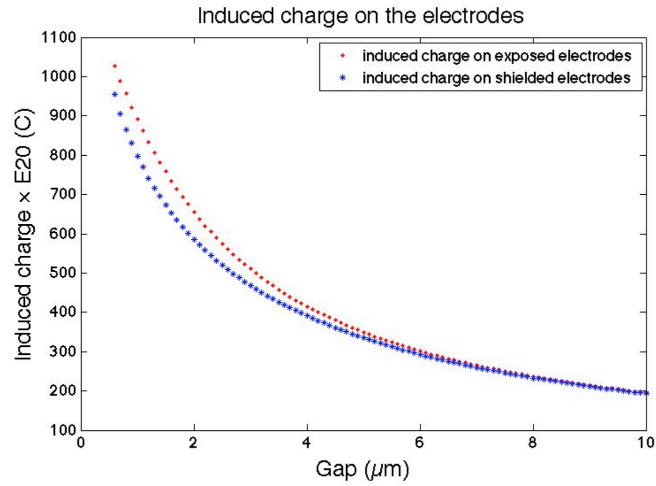

(a) The amount of the induced charge on the electrodes

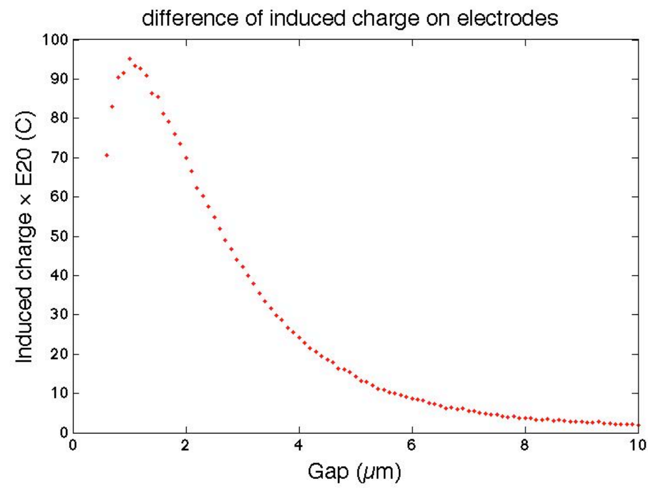

(b) Difference in the amount of the induced charge

Figure 5.4. Gap vs. induced charge. S_w = 6 μm, E_w = 4 μm, t_s = 4 μm. (Grounded shutter design with a rectangular cross-section)

5.2 Floating Shutter Design

The idea of the floating shutter design is that, as the shutter is not grounded, in Figure 5.5, the field strength on the surface of the exposed electrodes could be calculated using:

$$E_{ex} = \frac{V_s}{d + t_s + G} \tag{5.1}$$

While, on the surface of the shielded electrodes, the field strength is:

$$E_{sh} = \frac{V_s}{d + G + \frac{t_s \cdot \varepsilon_{rAir}}{\varepsilon_{rSi}}} \tag{5.2}$$

Noticing that the relative permittivity of air (ε_{rAir}) is approximately 1, when the relative permittivity of silicon (ε_{rSi}) is 11.68, as a result, E_{sh} is slightly larger than E_{ex}. This leads to a change in the amount of induced charge on the electrodes. The simulations showed that, with the same structure, the difference in the amount of induced charge on two sets of electrodes is several times larger than the grounded shutter design. The yellow lines in Figure 5.5 are the gold deposited only on the surface of the floating shutter to render an equipotential.

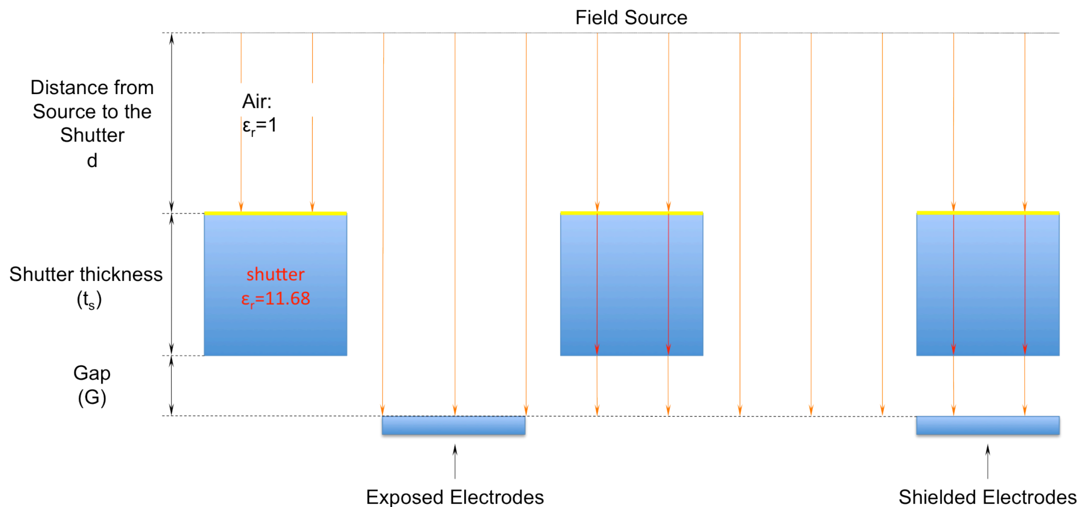

Figure 5.5. Schematic view of the floating shutter design.

Width of Slit (S_w):

The amount of induced charge on each set of electrodes decreases with the increasing width of the slits instead of increasing in the grounded shutter design. However, the difference increases in the range from 2 μm to 8 μm, see Figure 5.6 (b). When the width exceeds 8 μm, the increment saturated because of a rapid drop in amount of induced charge on the shielded electrodes. Therefore, the optimal width of slit with the given parameters would be 7 μm, which gives both good result and enough silicon size for the structure strength. The scattered points in Figure 5.6 (b) are probably resulted from the convergence criteria that are not small enough for the simulation.

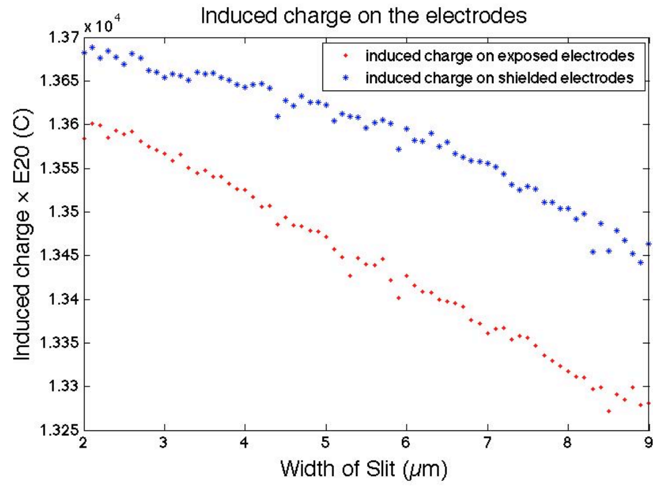

(a) The amount of the induced charge on the electrodes

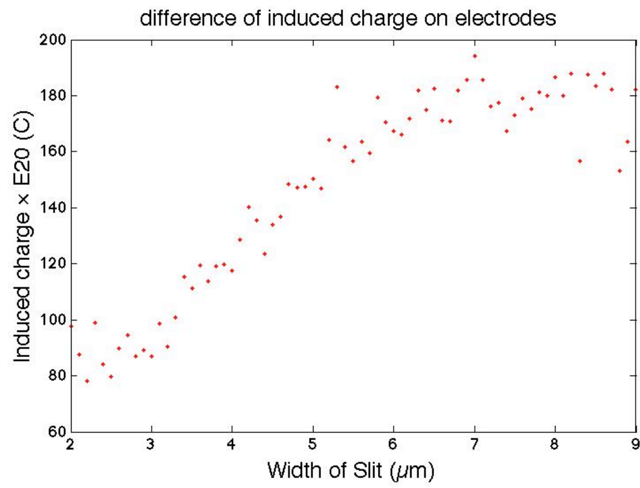

(b) Difference in the amount of the induced charge

Figure 5.6. Width of slit vs. induced charge. $E_w = 4$ µm, $t_s = 4$ µm, G = 4 µm. (Floating shutter design with a rectangular cross-section)

Electrode Width (E_w):

The amount of induced charge on both sets of the electrodes increases with larger electrode width, while the difference is relatively stable when the width is within the range from 2 μm to 3.5 μm, then a reduction appears in a linear way, see Figure 5.7. The Figure indicates that a 2 μm to 3.5 μm electrode width is optimal with other parameters fixed at the given value. The scattered points in Figure 5.7 (b) are probably resulted from the convergence criteria that are not small enough for the simulation.

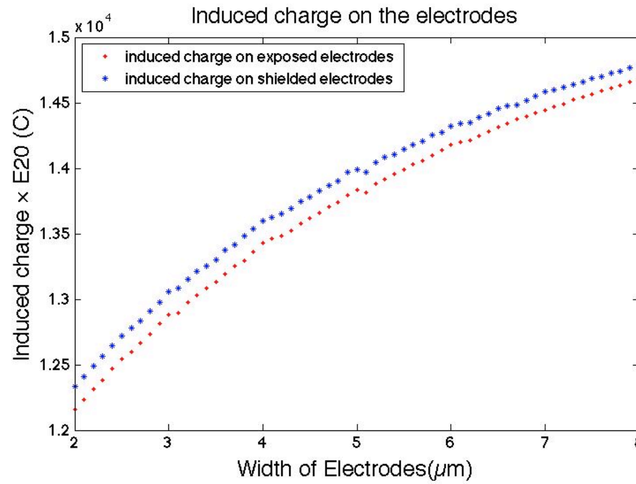

(a) The amount of the induced charge on the electrodes

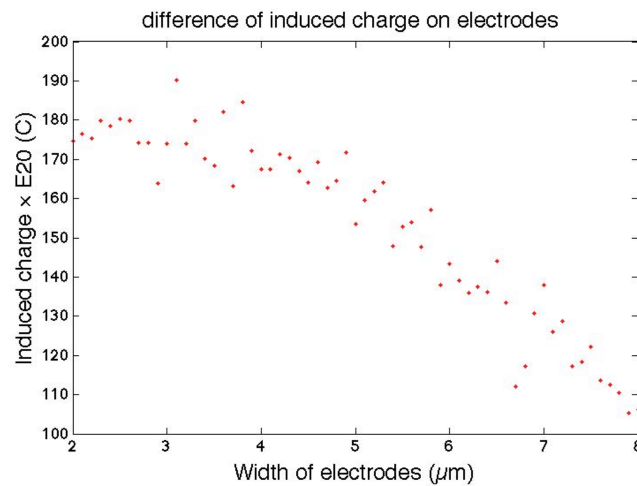

(b) Difference in the amount of the induced charge

Figure 5.7. Width of electrode vs. induced charge. S_w = 6 μm, t_s = 4 μm, G = 4 μm. (Floating shutter design with a rectangular cross-section)

Shutter Thickness (t_s):

The simulations indicate that the difference in the amount of induced charge on both sets of the electrodes grows when a thicker shutter is employed. Basically, a thicker shutter would be welcomed in this case, however, this may cause trouble in the real

fabrication process. A shutter with 6 μm to 7 μm thickness is reasonable since the benefit in difference is limited with a thicker shutter. The scattered points in Figure 5.8 (b) are probably resulted from the convergence criteria that are not small enough for the simulation.

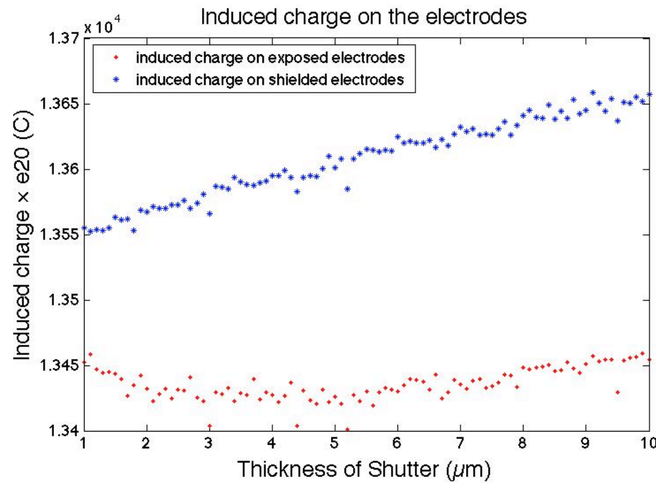

(a) The amount of the induced charge on the electrodes

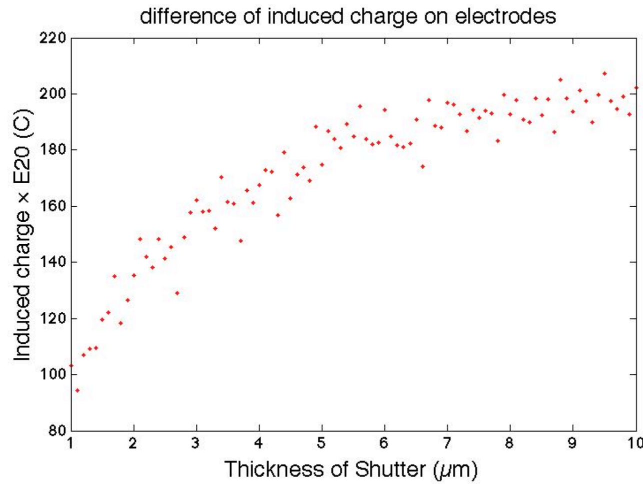

(b) Difference in the amount of the induced charge

Figure 5.8. Shutter thickness vs. induced charge. S_w = 6 μm, E_w = 4 μm, G = 4 μm. (Floating shutter design with a rectangular cross-section)

Gap between Shutter and Electrodes (G):

An increasing in size of the gap will cut down the difference in amount of induced charge on both sets of the electrodes greatly. Unlike that of the grounded shutter design, the total amount of induced charge on the set of exposed electrodes increases as the gap increases. This could be easily seen in Figure 5.9 (a). We can also see that the amount of induced charge on both sets of electrodes tend to equalize with increasing gap size. Thus, a smaller gap size is preferred theoretically. However, a tiny gap size may cause trouble in real fabrication process.

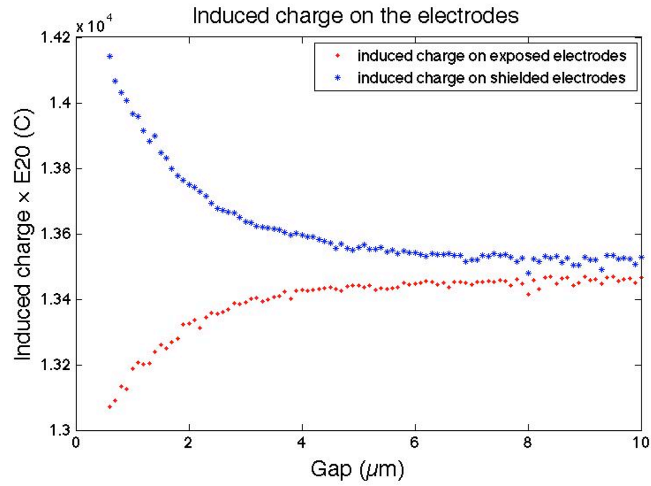

(a) The amount of the induced charge on the electrodes

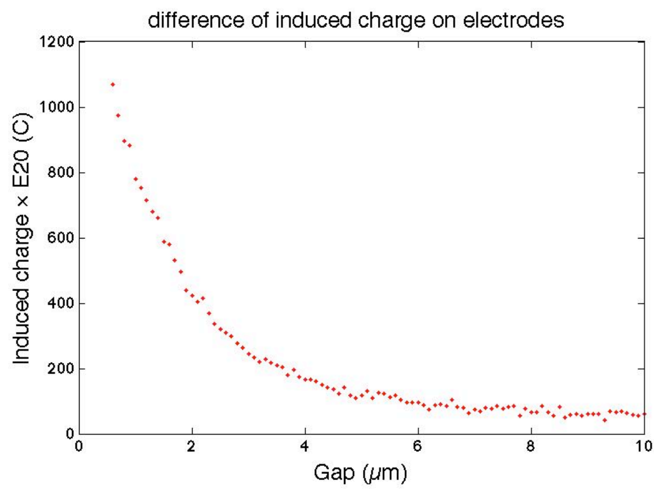

(b) Difference in the amount of the induced charge

Figure 5.9. Gap vs. induced charge. S_w = 6 μm, E_w = 4 μm, t_s = 4 μm. (Floating shutter design with a rectangular cross-section)

5.3 Trapezoidal Shutter Cross-section

The trapezoidal shutter cross-section is initially a compromise of the real fabrication process. Since in our cleanroom, the best anisotropic rate (A) of the plasma etch could only be 0.8, see section 3.2.2. However, later simulations revealed that, this actually led to a better result than the rectangular shutter cross-section designs. Figure 5.10 is a schematic view of the trapezoidal shutter cross-section.

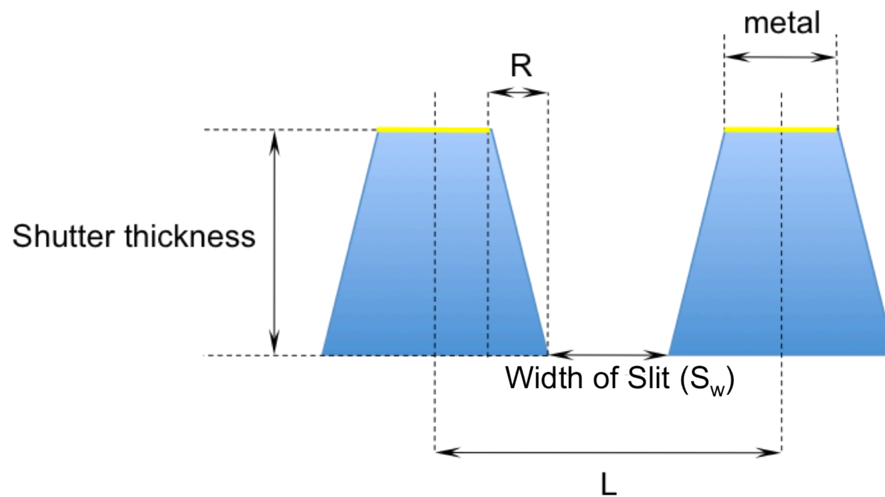

Figure 5.10. Schematic view of the trapezoidal shutter cross-section.

5.3.1 Design with Electrically Grounded Shutter

In this section, sensor designs with shutters that are electrically grounded were simulated. Results with the anisotropy equals 0.6 are also listed along with the ones with the anisotropy equals 0.8 as a comparison.

Width of slit (S_w):

The width of slit here has a confinement in range, instead of from 2 μm to 10 μm, it could only range from 2 μm to 8.4 μm when A equals 0.8 and from 2 μm to 6.8 μm when A equals 0.6. That's the result of the imperfectly anisotropic etch which creates an

outward slope at the edge, (see Figure 5.10 above). L, which is 10 micron in our design, is the period of the perforation in the shutter, R, the width of the ramp, equals isotropic rate times shutter thickness, where isotropic rate is (1-A). Therefore, in order to maintain the metal on the top layer of the shutter, essential to keep the shutter electrically grounded, the width of slit has to be smaller than 8.4 μm and 6.8 μm when A equals 0.8 and 0.6 respectively. Generally, in this case, the effect of width of slit is similar to that of the rectangular cross-section. The larger width of slit, the larger the difference and a better output signal. The optimal width of slit is 7 μm when A equals 0.8, (see Figure 5.11 (b)). A great drop in the difference of the amount of the induced charge at the right end of the curve indicates that, when the width of the metal layer is getting smaller, more fringing field could couple through the shutter and the field distribution beneath shutter alters greatly. This will be discussed in the latter parts of this chapter.

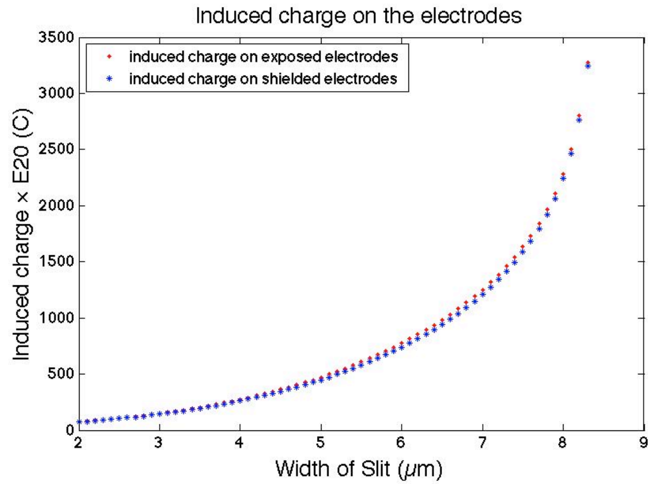

(a) The amount of the induced charge on the electrodes

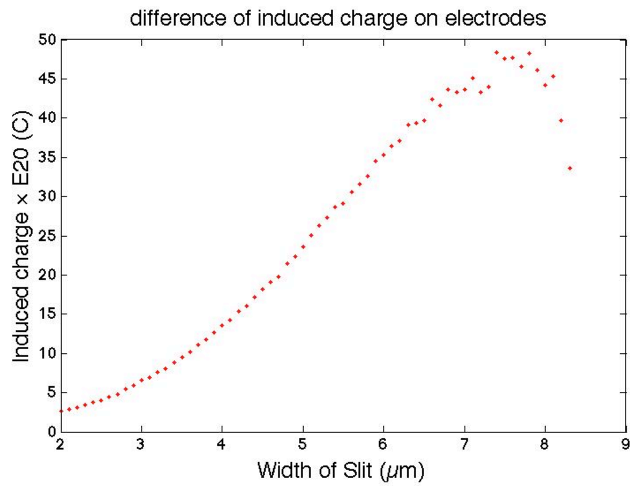

(b) Difference in the amount of the induced charge

Figure 5.11. Width of slit vs. induced charge, A equals 0.8. E_w = 4 μm, t_s = 4 μm, G = 4 μm. (Grounded shutter design with a trapezoidal cross-section)

Figure 5.12 shows the result of the same design with A equaling 0.6. No obvious difference can be observed except the actual amount of the induced charge. Comparing the induced charge on different electrodes in Figure 5.12 (a), a larger amount of induced charge could be found in the situation where A equals 0.6. But this amplification does not give a larger difference. In Figure 5.12 (b), the profile of the difference shows a similarity

in both magnitude and tendency, which means that when other three parameters are fixed, the anisotropy would not introduce much difference with an altering width of slit.

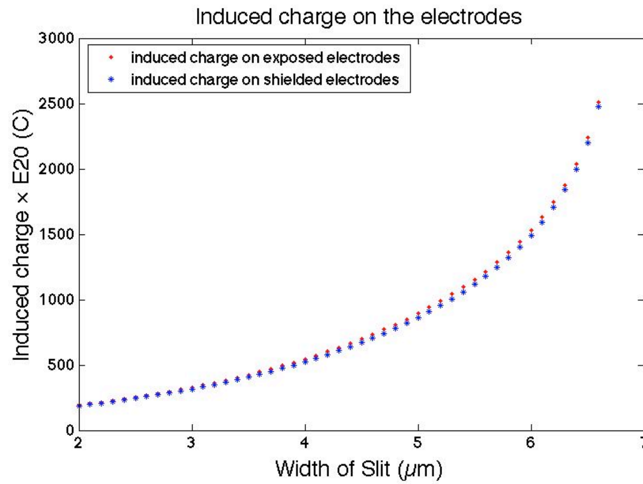

(a) The amount of the induced charge on the electrodes

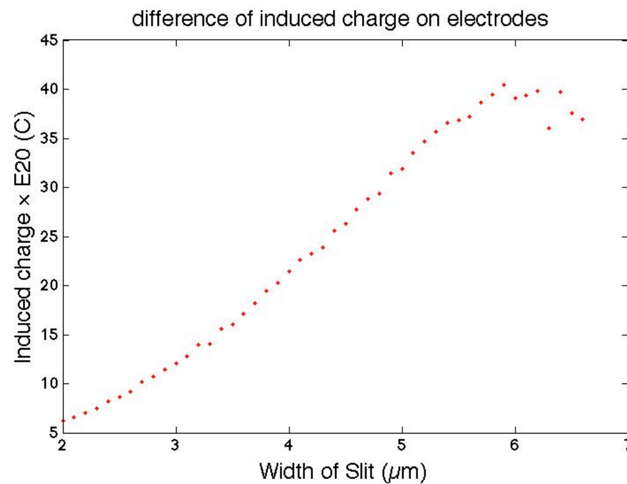

(b) Difference in the amount of the induced charge

Figure 5.12. Width of slit vs. induced charge, A equals 0.6. E_w = 4 µm, t_s = 4 µm, G = 4 µm. (Grounded shutter design with a trapezoidal cross-section)

Electrode Width (E_w):

The electrode width of the shutter with trapezoidal cross-section functions almost the same as the one of the rectangular cross-section, that is, though, larger electrode width gives a larger amount of induced charge on each set of the electrodes as increased surface area, the difference actually shrinks. Furthermore, a peak amount of difference could be observed in Figure 5.13 (b) when width of electrodes is between 2 μm and 3 μm. As a result, a series of thinner electrodes will be required. In this case, the minimum size is set at 2 μm with the considering of fabrication resolution.

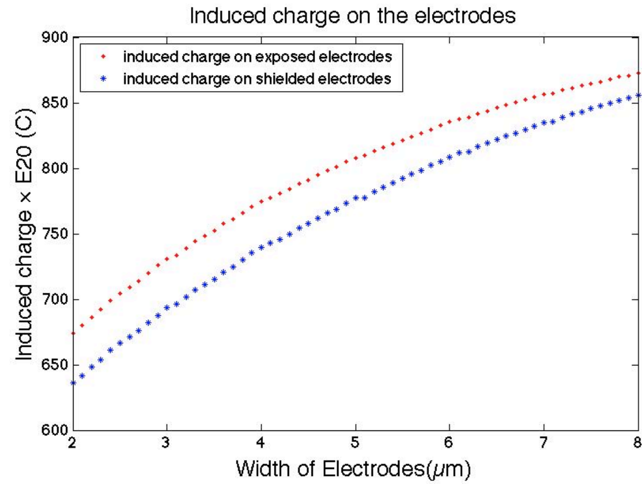

(a) The amount of the induced charge on the electrodes

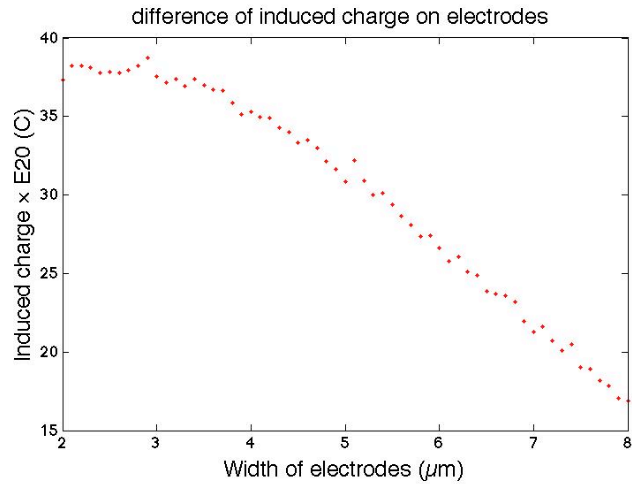

(b) Difference in the amount of the induced charge

Figure 5.13. Electrodes width vs. induced charge, A equals 0.8. S_w = 4 µm, t_s = 4 µm, G = 4 µm. (Grounded shutter design with a trapezoidal cross-section)

A great increase in the amount of induced charge on each set of electrode is shown in Figure 5.14. By reducing the anisotropy to 0.6, more fringing field could couple into the space beneath shutter. Also, a slight increment of difference could be observed in Figure 5.14 (b) while the maximum still exist when the width of electrodes is around 3µm.

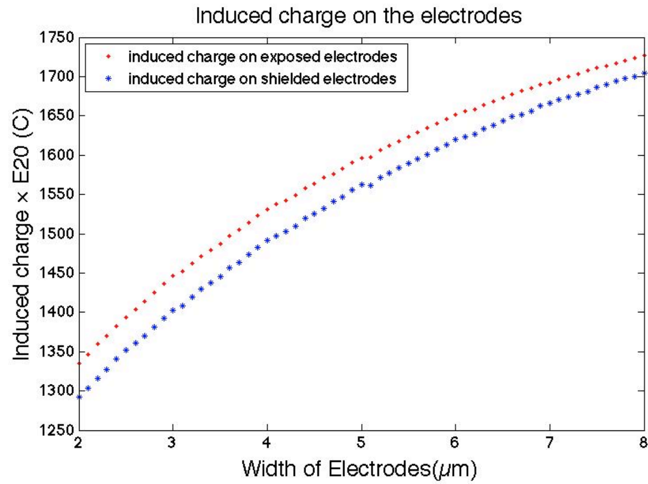

(a) The amount of the induced charge on the electrodes

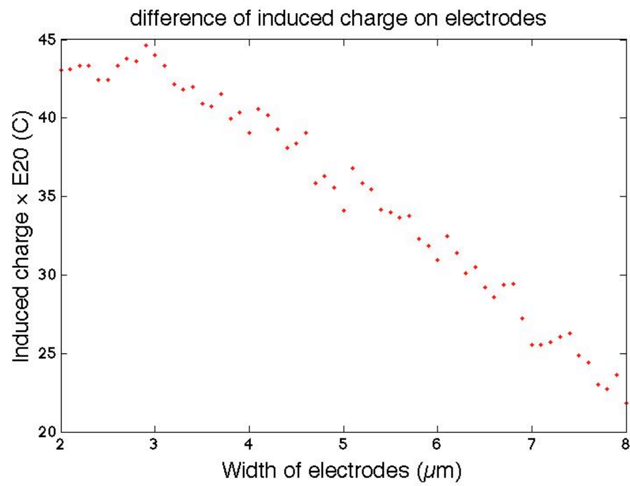

(b) Difference in the amount of the induced charge

Figure 5.14. Electrodes width vs. induced charge, A equals 0.6. S_w = 4 μm, t_s = 4 μm, G = 4 μm. (Grounded shutter design with a trapezoidal cross-section)

Shutter Thickness (t_s):

Figure 5.15 (a) gives an idea how the amount of induced charge on the electrodes will change when shutter thickness alters with electrodes width, width of slit and gap all fixed. The amount firstly drops as the shutter thickness increases, which is the same as

the rectangular cross-section ones. However, when the thickness reaches a certain value, between 4 μm and 5 μm, the amount of induced charge starts to increase, since more silicon is exposed because of the imperfectly anisotropic etch. The fringing field is now more easily to couple into the silicon instead of the air, and as explained before, this reduces the attenuation of the electric field strength.

After the thickness of shutter exceeds a critical value, 7.4 μm as shown in Figure 5.15 (b), the area of exposed silicon in the shutter is large enough to alter the field distribution beneath the shutter greatly so that the series of covered electrodes tend to have more induced charge on its surface than the exposed one.

Nevertheless, within the range of the thickness simulated here, the maximum difference still happens when the shutter thickness is small. In our design, a 4 μm shutter thickness will be selected.

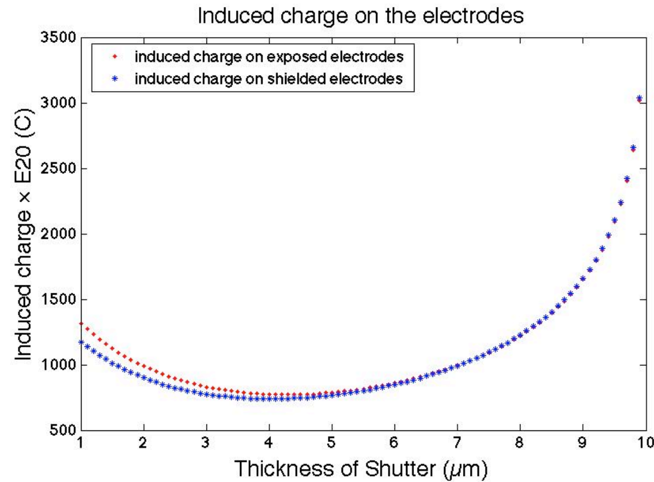

(a) The amount of the induced charge on the electrodes

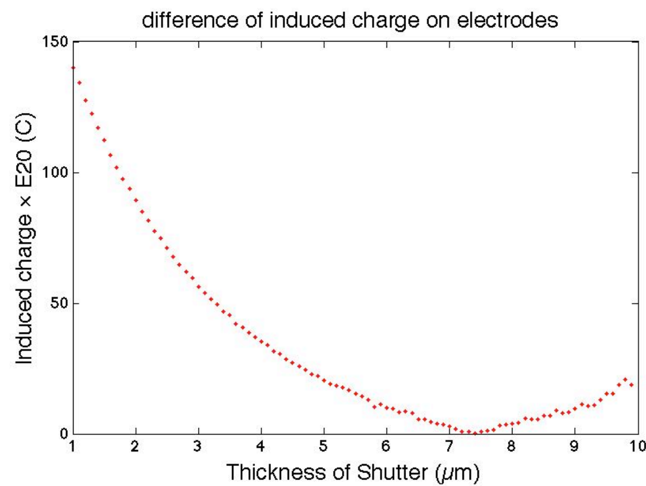

(b) Difference in the amount of the induced charge

Figure 5.15. Shutter thickness vs. induced charge, A equals 0.8. S_w = 4 μm, E_w = 4 μm, G = 4 μm. (Grounded shutter design with a trapezoidal cross-section)

Figure 5.16 indicates how the shutter thickness affects the amount of induced charge when anisotropy equals 0.6. Compared to the one with the anisotropy equaling 0.8, no obvious difference can be observed from Figure 5.16 (a) except the actual amount. However, in Figure 5.16 (b), the difference of the one with a 0.6 anisotropy tends to drop slightly faster than the one with a 0.8 anisotropy but never reaches the zero. The

comparison shows that the anisotropy does not have much effect on the sensor performance in terms of the shutter thickness.

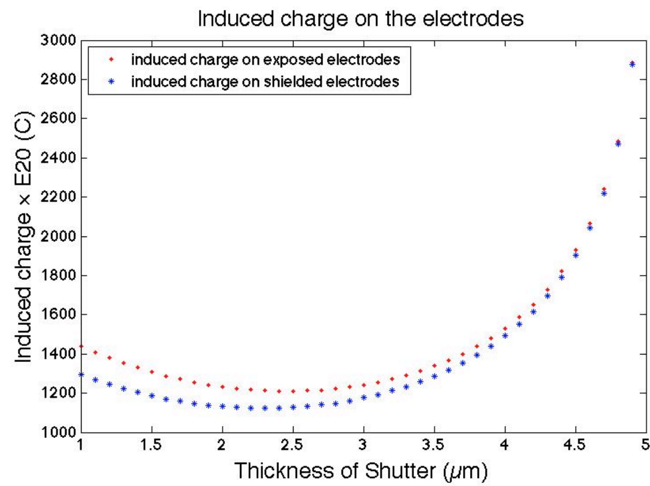

(a) The amount of the induced charge on the electrodes

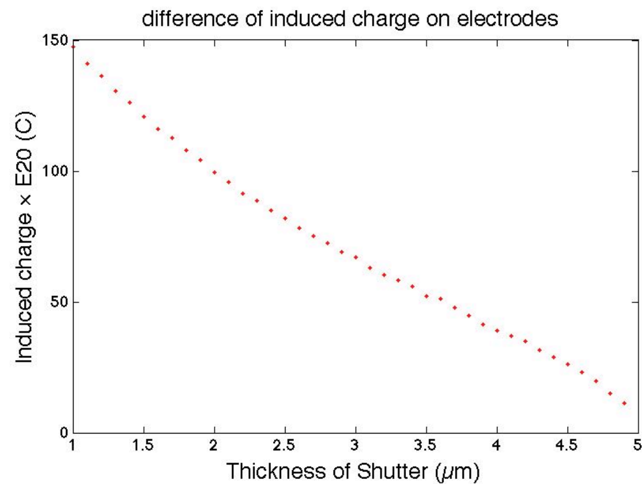

(b) Difference in the amount of the induced charge

Figure 5.16. Shutter thickness vs. induced charge, A equals 0.6. S_w = 4 μm, E_w = 4 μm, G = 4 μm. (Grounded shutter design with a trapezoidal cross-section)

Gap between Shutter and Electrodes (G):

As gap increases, the difference in the amount of the induced charge generally decreases so as the amount on each set of electrodes, except at the range where the gap is small, around 1μm, see Figure 5.17. The optimal gap in this case is 2 μm.

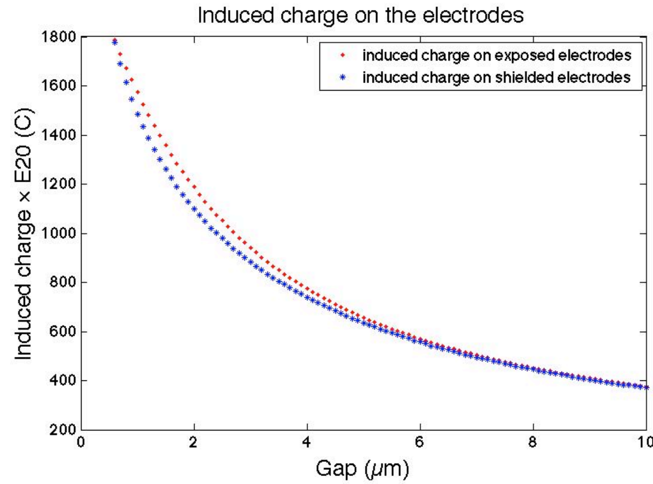

(a) The amount of the induced charge on the electrodes

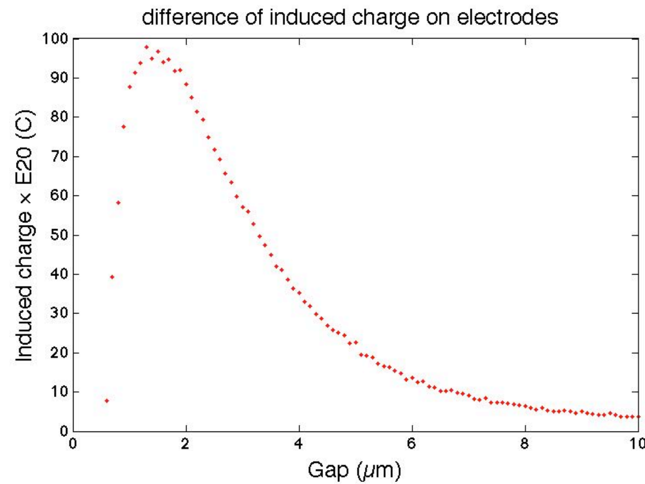

(b) Difference in the amount of the induced charge

Figure 5.17. Gap vs. induced charge, A equals 0.8. S_w = 4 μm, E_w = 4 μm, t_s = 4 μm. (Grounded shutter design with a trapezoidal cross-section)

In this case, the one with a 0.6 anisotropy seems having a different result. A tail can be clearly observed in Figure 5.18 (b). However, a closer look reveals a same tendency in the amount of the induced charge one each set of the electrodes. In Figure 5.18 (a), the shielded electrodes have more amount of the induced charge initially, but drop much faster than the exposed one when the gap increases from 1 μm to 2 μm. In this region, the amount of the induced charge on the shielded electrodes is actually lower than that on the exposed ones. A further increasing in the gap leads to a saturation in the decreasing of the amount of the induced charge on the exposed electrodes and the difference again start to shrink. This phenomenon could also be seen in Figure 5.17 (a). Thus, it is appropriate to say that instead of giving a complete different result, the change of the anisotropy results in a higher field strength beneath the shutter, a shift the profile of the difference a little bit towards the x-axis and a reduction in the difference.

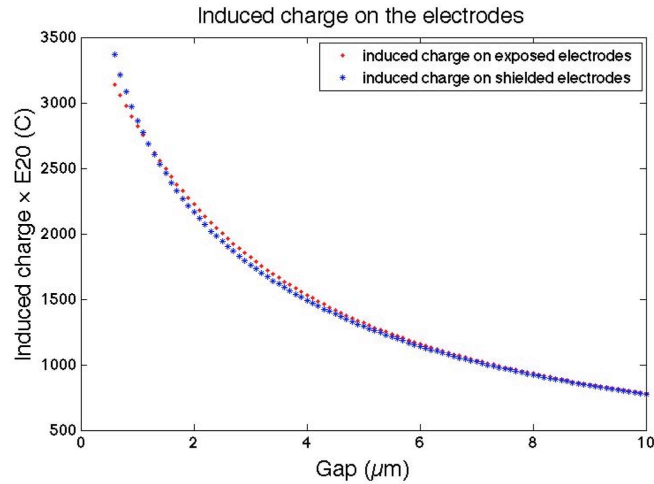

(a) The amount of the induced charge on the electrodes

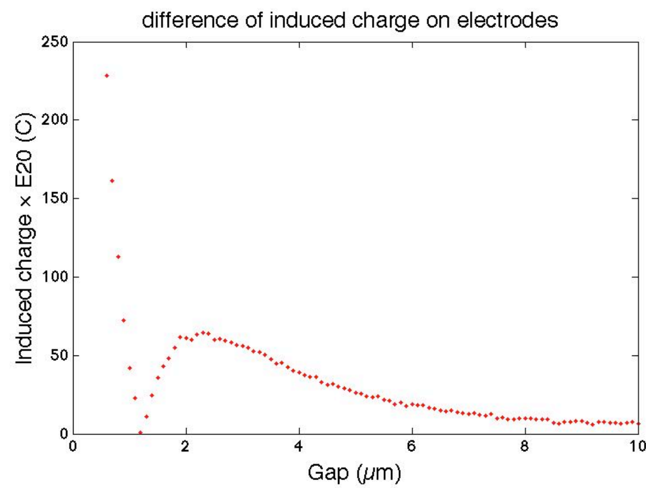

(b) Difference in the amount of the induced charge

Figure 5.18. Gap vs. induced charge, A equals 0.6. S_w = 4 μm, E_w = 4 μm, t_s = 4 μm. (Grounded shutter design with a trapezoidal cross-section)

The bizarre profile in both Figure 5.17 (b) and Figure 5.18 (b) might be explained in the way below. When the gap is around or smaller than 1 μm, (see Figure 5.19 (a)), the fringing field coupling into the exposed silicon is strong enough to contribute to the induced charge on the electrodes. After gap exceeds 2 μm, (see Figure 5.19 (b)), the

fringing through the slits dominates, and the difference in induced charge turns out to be similar to that of rectangular cross-section.

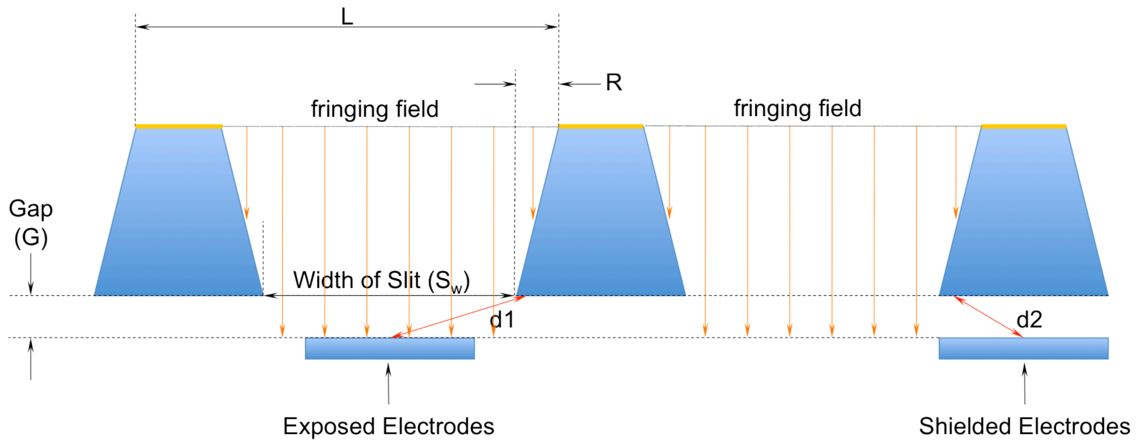

(a)

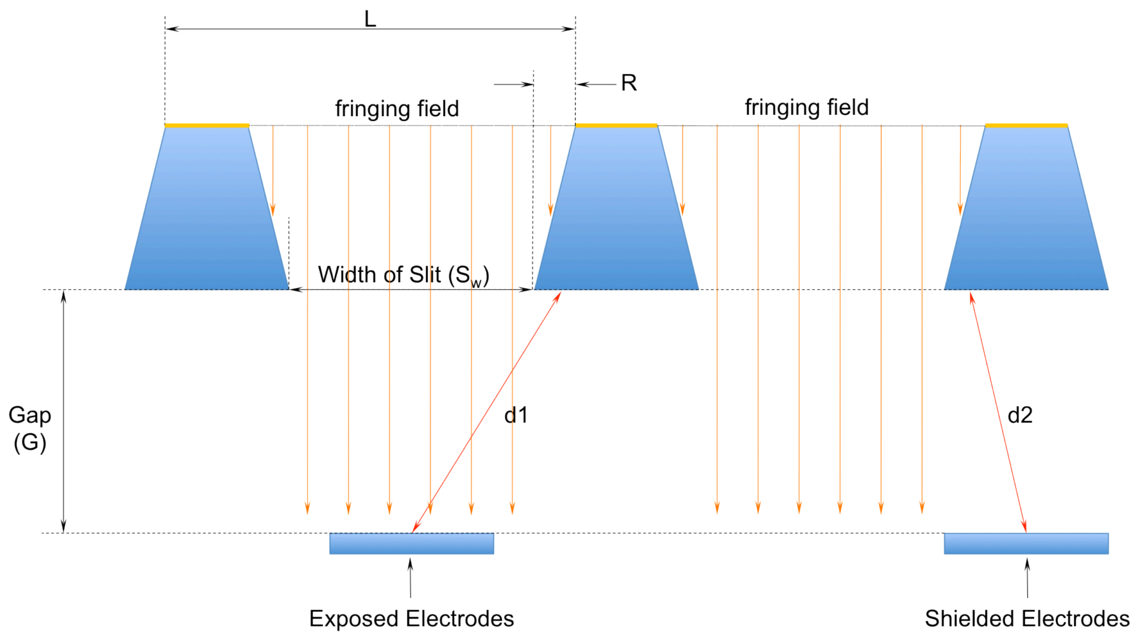

(b)

Figure 5.19 Guessing of the reason of the abnormal result of close gap with trapezoidal shutter cross-section (a) Gap is small; (b) Gap is large

5.3.2 Floating shutter design with Trapezoidal Shutter Cross-section

The floating shutter designs with trapezoidal shutter cross-section were also simulated. They share the same structure with the design with trapezoidal shutter cross-section except that the metal layer is removed on the driving beam and springs so that the shutter is not electrically grounded.

Same as what was done in section 5.3.1, two different designs with A equals 0.8 and 0.6 were simulated and compared.

Width of Slit (S_w):

Similar to that of the floating shutter design with rectangular shutter cross-section, the increased width of slit also leads to a decrease in the amount of induced charge on the both sets of the electrodes while the difference, on contrary, grows. From Figure 5.20, a 6 μm to 7 μm width of slit will be good considering both the difference and the shutter structural strength. The scattered points in Figure 5.20 (b) are probably resulted from the convergence criteria that are not small enough for the simulation.

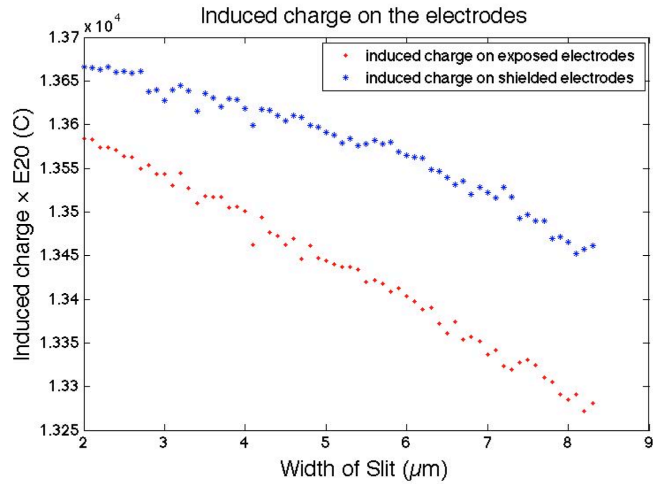

(a) The amount of the induced charge on the electrodes

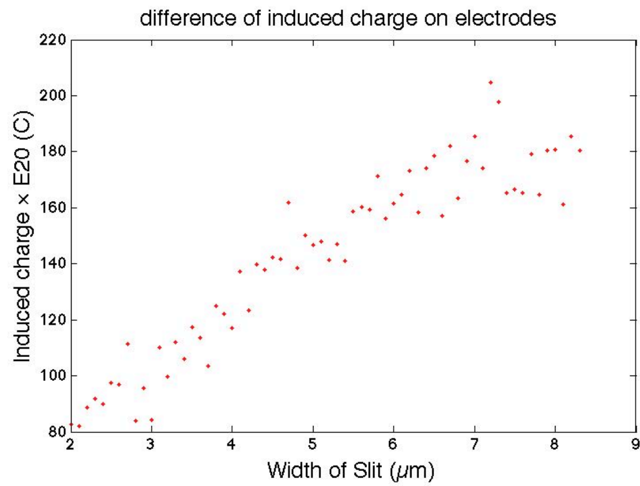

(b) Difference in the amount of the induced charge

Figure 5.20. Width of slit vs. induced charge, A equals 0.8. E_w = 4 μm, t_s = 4 μm, t_s = 4 μm. (Floating shutter design with trapezoidal cross-section)

To maintain the shutter thickness with a given width of slit, the shutter with A equaling 0.6 has smaller range in width of slit from 2 to 6.8 μm. The change of A leads to a slightly decrease in both amount of induced charge on each set of electrodes. But the difference hardly shrinks, as given in Figure 5.21. The results claim that the anisotropy is not critical to the output in terms of the slits in this case. The scattered points in Figure

5.21 are probably resulted from the convergence criteria that are not small enough for the simulation.

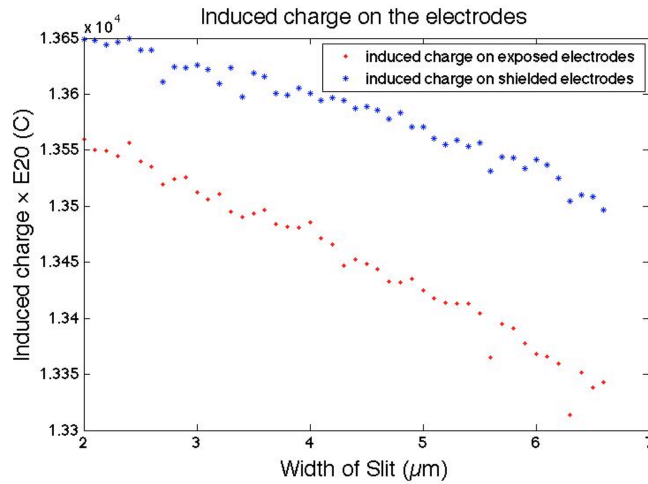

(a) The amount of the induced charge on the electrodes

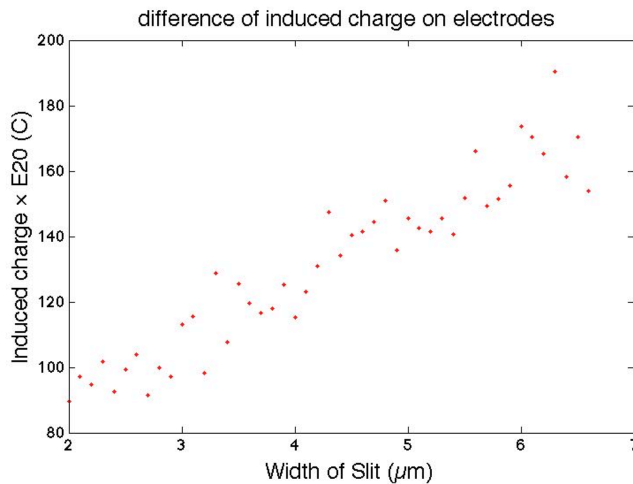

(b) Difference in the amount of the induced charge

Figure 5.21. Width of slit vs. induced charge, A equals 0.6. E_w = 4 µm, t_s = 4 µm, t_s = 4 µm. (Floating shutter design with trapezoidal cross-section)

Electrode Width (E_w):

The simulations of the electrode width of the trapezoidal shutter cross-section gave an almost identical result of that of the floating design with rectangular cross-section, except for that the actual difference is slightly lower. A maximum of difference could be observed in Figure 5.22 (b) when the electrodes width is around 3 μm. Therefore, the electrode width from 2 μm to 4 μm will be reasonable in fabrication with the given width of slit at 6 μm. The scattered points in Figure 5.22 (b) are probably resulted from the convergence criteria that are not small enough for the simulation.

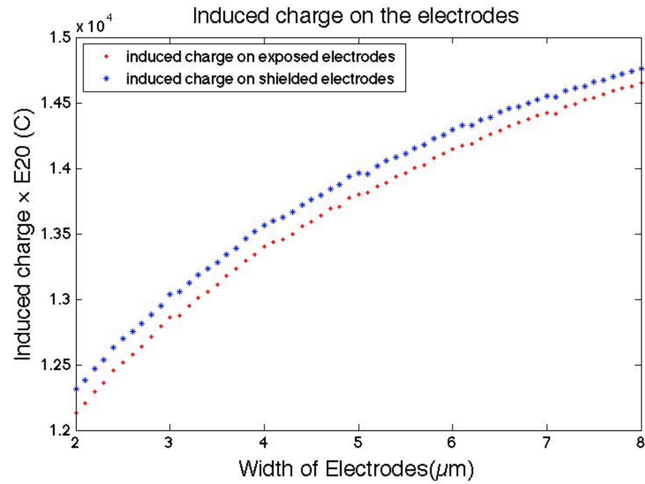

(a) The amount of the induced charge on the electrodes

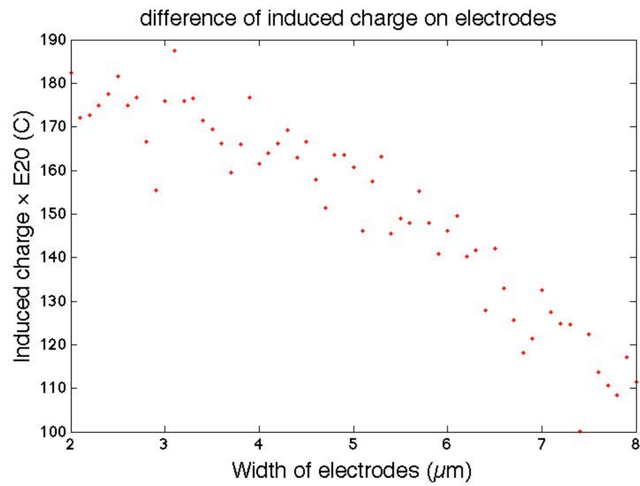

(b) Difference in the amount of the induced charge

Figure 5.22. Electrode width vs. induced charge, A equals 0.8. S_w = 6 μm, t_s = 4 μm, t_s = 4 μm. (Floating shutter design with trapezoidal cross-section)

The simulation gave an almost same result when change the anisotropy to 0.6. No obvious difference can be found Figure 5.23 compared to Figure 5.22. This gives the idea that, with a floating shutter, and fixed width of slit, gap and shutter thickness, the anisotropy will not affect the output signal over the various electrodes width. The

scattered points in Figure 5.23 (b) are probably resulted from the convergence criteria that are not small enough for the simulation.

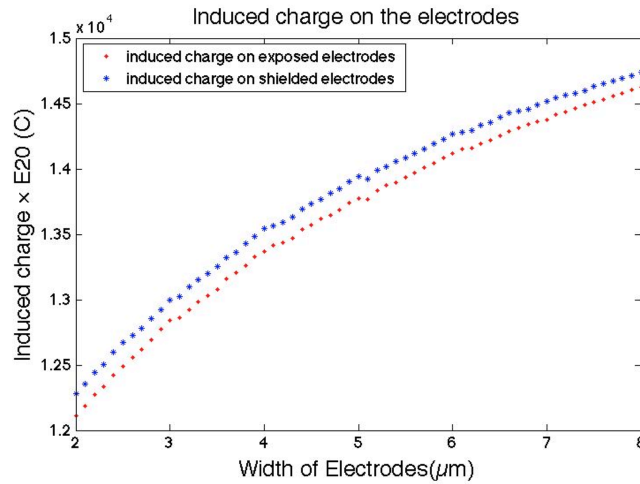

(a) The amount of the induced charge on the electrodes

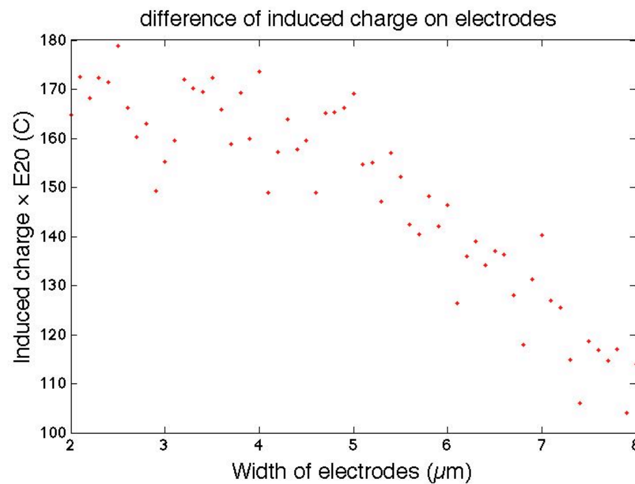

(b) difference in the amount of the induced charge

Figure 5.23. Electrode width vs. induced charge, A equals 0.6. S_w = 6 µm, t_s = 4 µm, t_s = 4 µm. (Floating shutter design with trapezoidal cross-section)

Shutter Thickness (t_s):

As shown in Figure 5.24, though the difference of amount of induced charge on both sets of electrodes has the same tendency to the rectangular cross-section design, the amounts of induced charge on each set of electrodes are not quite similar. Instead of having a growth in the total amount of induced charge, it actually reduces on the exposed electrodes and initially grows then decreases on the shielded electrodes. However, as the difference is still holding a growing tendency, the thicker shutter will still be optimal. In our design, the shutter thickness will be selected to be 6 μm or 7 μm. The scattered points in Figure 5.24 (b) are probably resulted from the convergence criteria that are not small enough for the simulation.

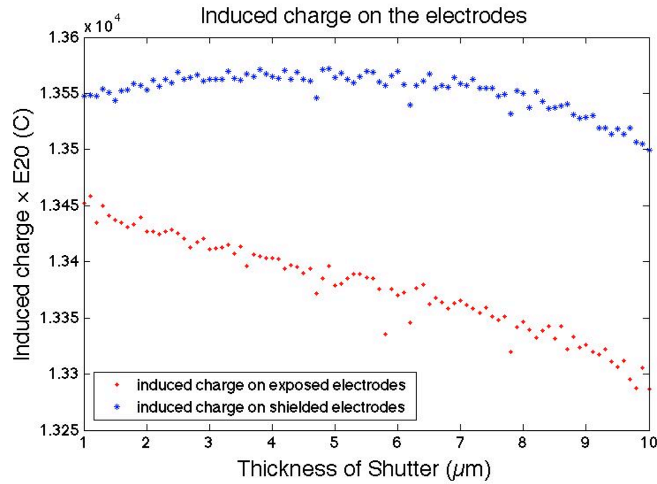

(a) The amount of the induced charge on the electrodes

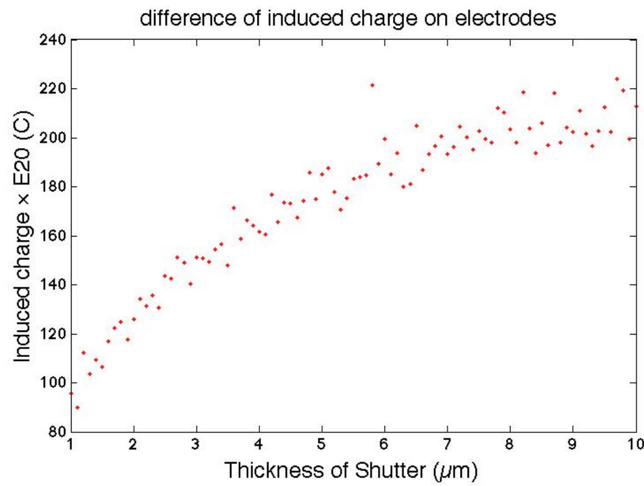

(b) Difference in the amount of the induced charge

Figure 5.24. Shutter thickness vs. induced charge, A equals 0.8. S_w = 6 µm, E_w = 4 µm, G = 4 µm. (Floating shutter design with trapezoidal cross-section)

Figure 5.25 is the result when the anisotropy equals 0.6. As explained before, the maximum shutter thickness here could only be 4.8 µm to maintain the slits with at 6 µm. Despite of the difference in the range of the variable, two results seem quite similar to each other. The difference also presents an increasing tendency along the shutter thickness. As the conclusion, the anisotropy would not change the result in terms of the

shutter thickness. The scattered points in Figure 5.25 are probably resulted from the convergence criteria that are not small enough for the simulation.

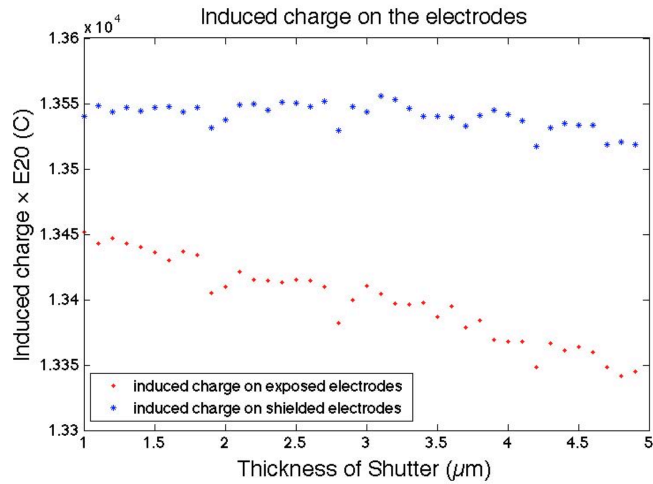

(a) The amount of the induced charge on the electrodes

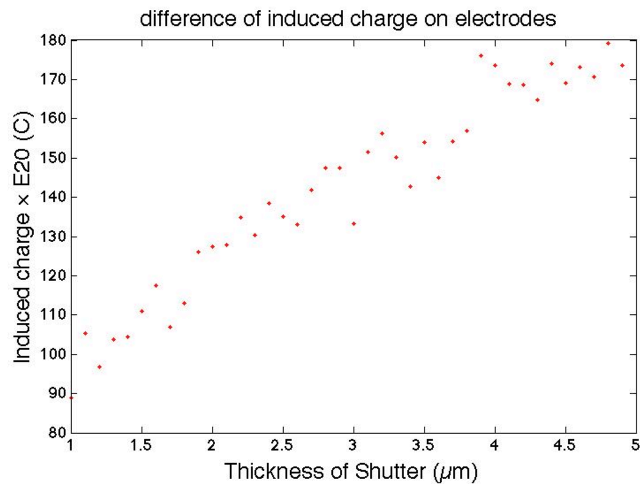

(b) Difference in the amount of the induced charge

Figure 5.25. Shutter thickness vs. induced charge, A equals 0.6. S_w = 6 μm, E_w = 4 μm, G = 4 μm. (Floating shutter design with trapezoidal cross-section)

Gap between Shutter and Electrodes (G):

Figure 5.26 demonstrates the effect of gap between shutter and electrodes. According to Figure 5.26 (a), the field strength also tends to average out behind the shutter, which gives an increment in the amount of induced charge on the exposed electrodes and a reduction on the shielded ones, thus a dramatic drop in the difference. As a result, a small gap is critical to the output signal. Basically, the idea gap is 1 μm. However, that may cause trouble in fabrication, and a 2 μm gap is selected.

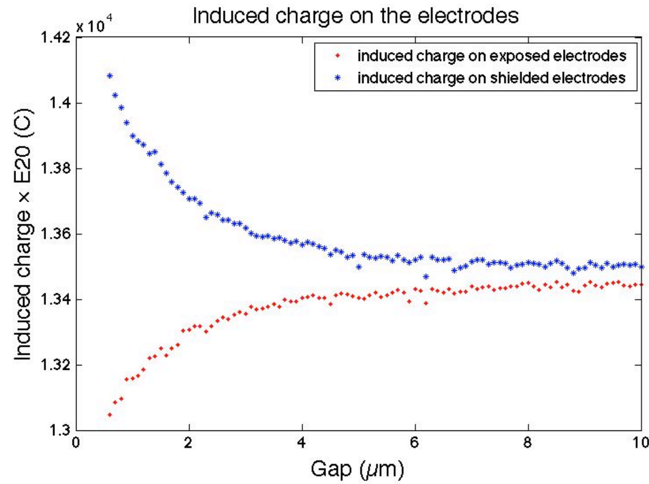

(a) The amount of the induced charge on the electrodes

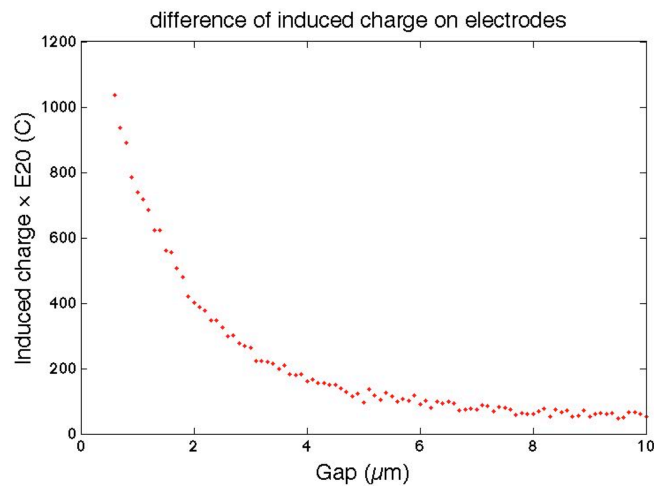

(b) Difference in the amount of the induced charge

Figure 5.26. Gap vs. induced charge, A equals 0.8. S_w = 6 μm, E_w = 4 μm, t_s = 4 μm. (Floating shutter design with trapezoidal cross-section)

By changing the A to 0.6, no apparent difference in the result had taken place, according to Figure 5.27. Both cases share a same tendency, that the difference decrease over the gap, though, the maximum in the one where the A equals 0.6 is little bit lower than the previous one. That suggests the anisotropy has no effect on the output in terms of the gap.

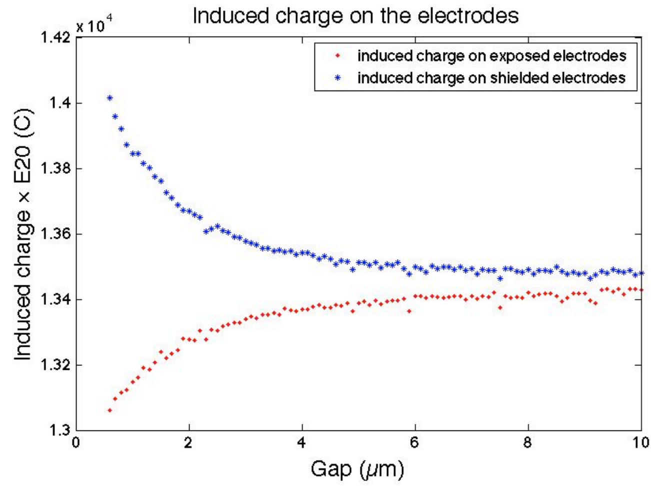

(a) The amount of the induced charge on the electrodes

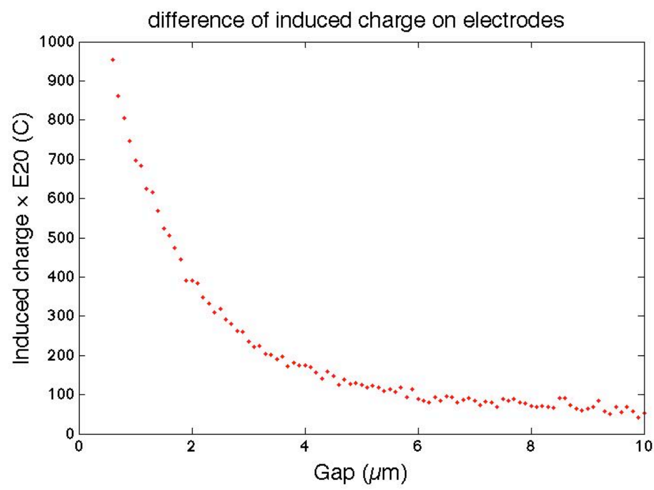

(b) Difference in the amount of the induced charge

Figure 5.27. Gap vs. induced charge, A equals 0.6. S_w = 6 μm, E_w = 4 μm, t_s = 4 μm. (Floating shutter design with trapezoidal cross-section)

5.4 Parameter Comparison

In this part, all of the differences from 4 series of simulations are put together so that a comparison could be carried out to give a brief idea on which design is optimal. The 'grounded rec', 'floating rec', 'grounded tetra' and 'floating tetra' stand for the grounded shutter design with rectangular shutter cross-section, floating shutter design with rectangular shutter cross-section, grounded shutter design with trapezoidal shutter cross-section and floating shutter with trapezoidal shutter cross-section, respectively.

5.4.1 Width of Slit (S_w)

Figure 5.28 shows a comparison between all four designs based on varieties of width of slit. Both plots indicate that, the differences of the floating shutter design are generally 4 times larger than that of the grounded shutter counterparts. While the grounded shutter design with trapezoidal shutter cross-section has a slightly larger difference than the grounded shutter design with rectangular shutter cross-section within the range from 2 μm to 7.5 μm. And there is not much difference between two floating shutter designs. It is apparent that a width of slit between 6 μm and 7 μm is optimal for all four designs.

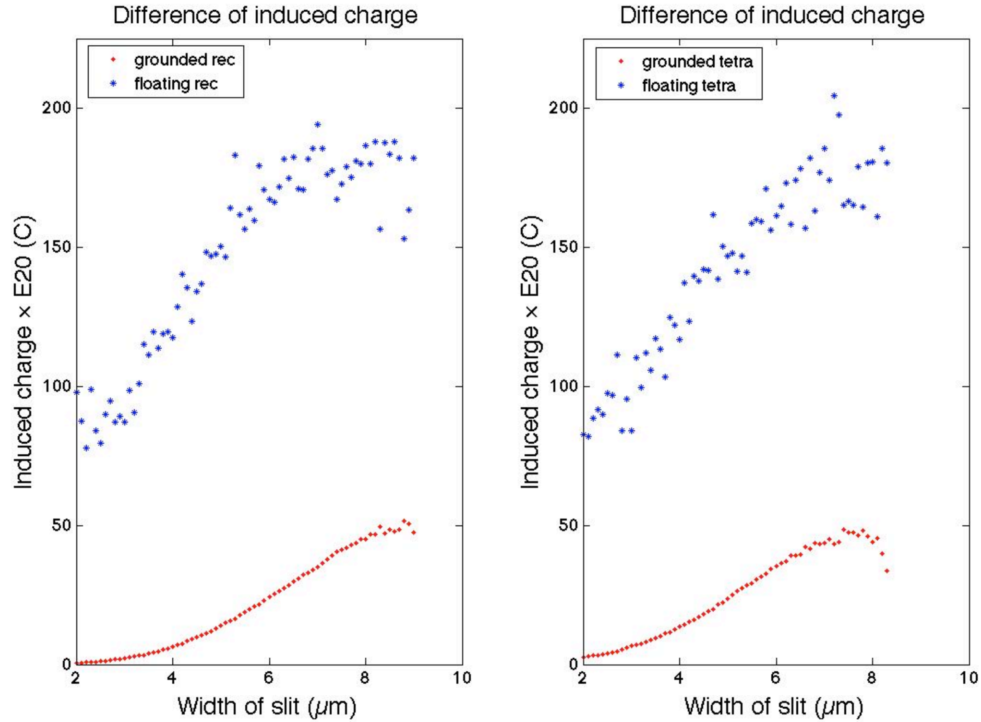

Figure 5.28. Results of different designs in terms of width of slit.

5.4.2 Electrodes Width (E_w)

Figure 5.29 is the comparison of the differences based on different width of electrodes. Both plots are the comparisons between grounded shutter design (red) and floating shutter design (blue). One can clearly see that the floating shutter designs surpass the grounded shutter designs over the whole range by approximately 4 to 5 times. While within the grounded shutter designs, the trapezoidal shutter cross-section one has a much better performance than the rectangular shutter cross-section one over the whole range. The two floating shutter designs have quite similar output. Generally, an electrode width at 3 μm could give a best result for all designs when given the width of slit at 6 μm.

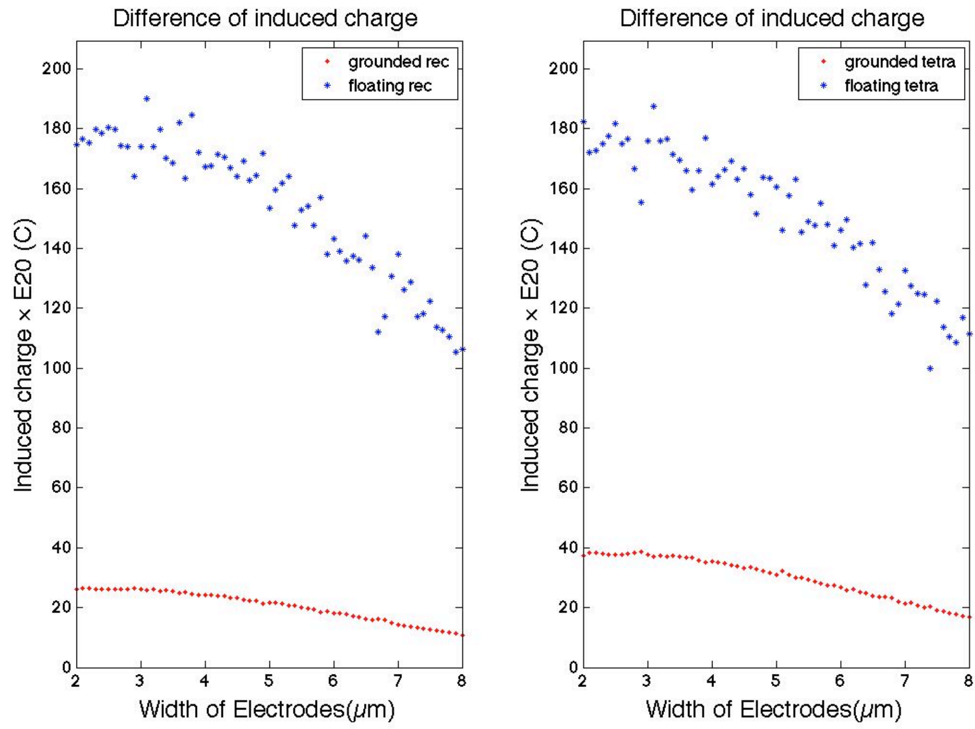

Figure 5.29. Result of different designs in terms of electrode width.

5.4.3 Shutter Thickness (t_s)

Figure 5.30 gives the output (difference) of four different designs. Both plots are the comparison between grounded shutter designs and floating shutter designs. At small shutter thickness, the grounded shutter designs have better performance. However, as the shutter gets thicker, the output of grounded shutter designs goes down while that of floating shutter goes up, and is a magnitude larger than the grounded shutter ones when the thickness reaches 6 μm. Again, comparison between plots show that the grounded shutter design with trapezoidal shutter cross-section performs better than the rectangular counterparts while the two floating shutter one have similar output. Clearly that a thin shutter will be idea for both grounded shutter designs, and a thicker shutter will be desired for floating shutter designs.

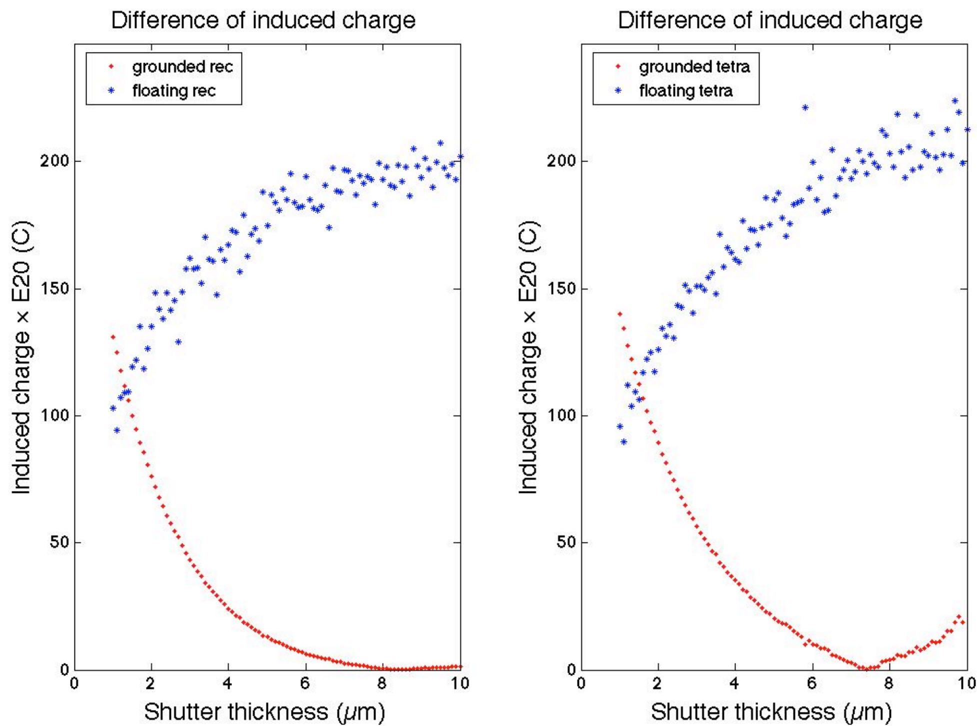

Figure 5.30. Results of different designs in terms of shutter thickness.

5.4.4 Gap between Shutter and Electrodes (G)

Figure 5.31 is the comparison of four designs over different gap between shutter and electrodes. All designs have a drop in output when the gap gets larger. However, the floating shutter designs have a greater decrease than the grounded shutter ones, the output drops from above 1000 in the first two plots to around 100 over the range, while the grounded shutter ones never exceed 100.

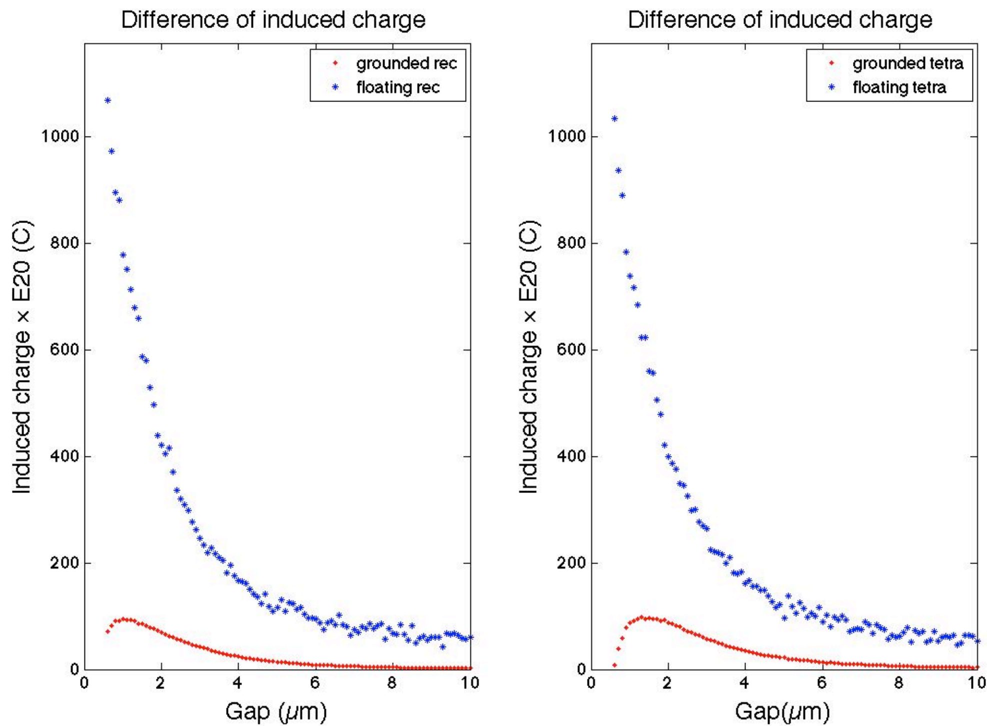

Figure 5.31. Results of different designs in terms of gap.

From all four Figures above, it is clear that with the same parameters, in most cases, the floating shutter designs have better performances and even scales the grounded shutter designs by a considerably large factor. Therefore, the floating shutter design would be suggested if the charging problem could be overcome.

5.5 Guard Ring

The guard ring here (see Figure 5.32) is designed with two main purposes.

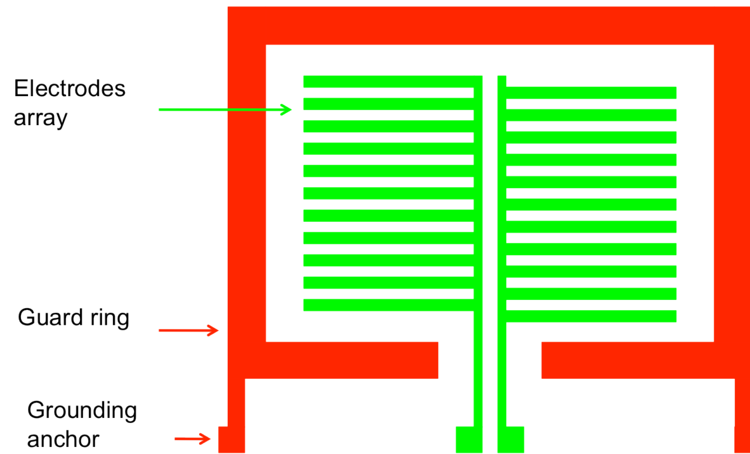

Figure 5.32. Schematic of guard ring.

First, it can stop the fringing field from coupling in at the edge of the shutter. This will be fully discussed in the incoming section 5.6. Second, it forms a shielding ground between the actuator and sensing electrodes. This issue did not exist in the previous design, for the power of the driving signal is relatively low, 75 mV in voltage and 1.8 mA in current, the interference from the driving signal is neglectable compared to the incident field. While, in the new generation of the design, a higher voltage will be required to make larger displacement, therefore greater interference from the driving signal. According to the simulations done by Mark Roy [41], the driving voltages of the candidates vary from 0.84 V to 3.2 V.

In this section, only the first phenomenon will be discussed, the second one still needs to be verified in the real test.

5.5.1 Grounded Shutter Design with Rectangular Shutter Cross-section

The Figure 5.33 gives a brief idea on how the guard ring works on the grounded shutter design with rectangular shutter cross-section. The first two plots show the amount

of induced charge on each set of electrodes. One can see a slight drop along the increasing width of guard ring. The drop comes from the blocking of the fringing field at the edge of the shutter. Since the arrays of the electrodes are set to be 30 μm away from the edge of the shutter, the amount of induced charge caused by the fringing is not large. However, it still indicates that the guard ring is working properly. And from the third and the fourth plot, it is clear that, this amount of induced charge is basically identical on both sets of the electrodes, for the difference in difference when width is 10 μm and 100 μm is less than 2. Generally, the thicker guard ring will be reasonable in this case.

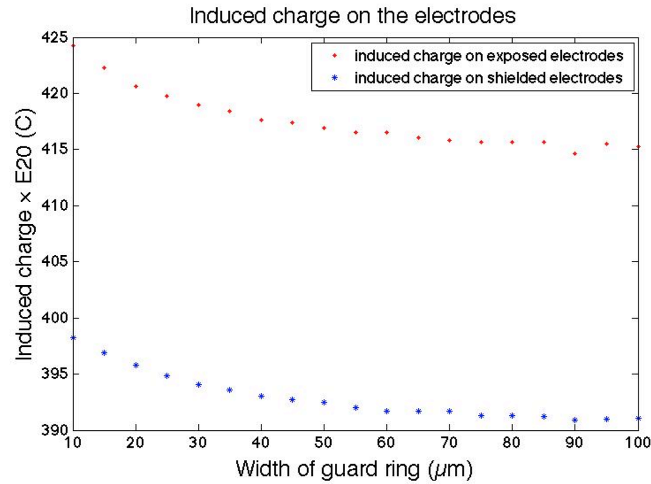

(a)

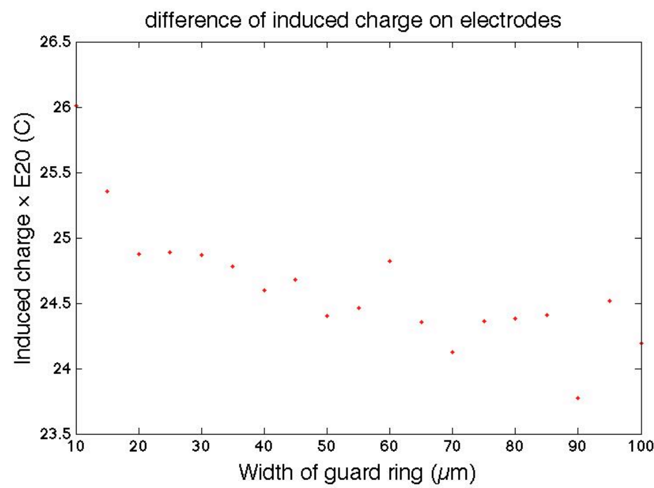

(b)

Figure 5.33. Guard ring on grounded shutter design with rectangular cross-section.

5.5.2 Grounded Shutter Design with Trapezoidal Cross-section

The Figure 5.34 shows the effect of guard ring on the grounded shutter design with trapezoidal shutter cross-section. The result is quite similar to that of the grounded

shutter design with rectangular shutter cross-section. In this case, still the thicker guard rings will be preferred.

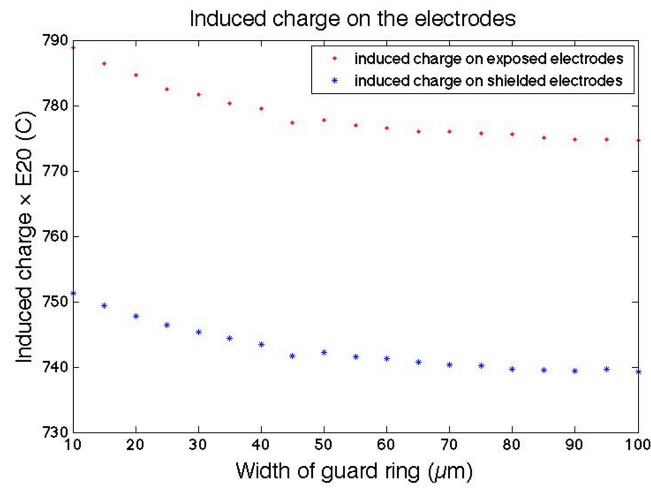

(a)

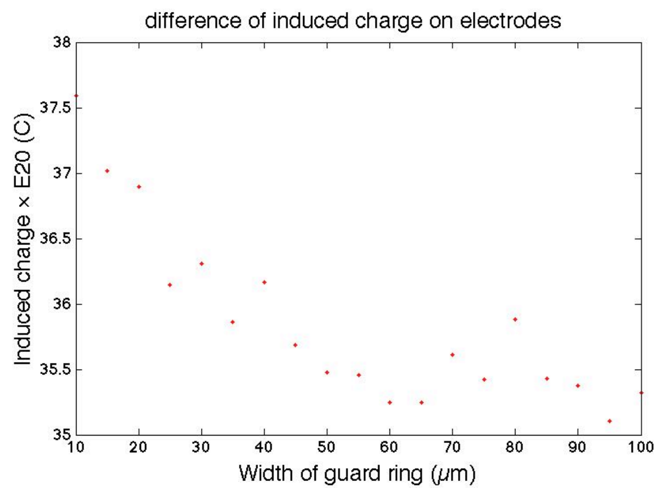

(b)

Figure 5.34. Guard ring on electrically grounded shutter design with trapezoidal cross-section.

5.5.3 Floating Shutter Design with Rectangular Cross-section

The Figure 5.35 indicates that the guard ring also works on the floating shutter design with rectangular shutter cross-section. A clear drop in amount of the induced charge on the both sets of electrodes could be observed. However, the result shows that, in Figure 5.35 (b), the difference actually increases by applying a thicker guard ring. Therefore, a thicker guard ring is preferred.

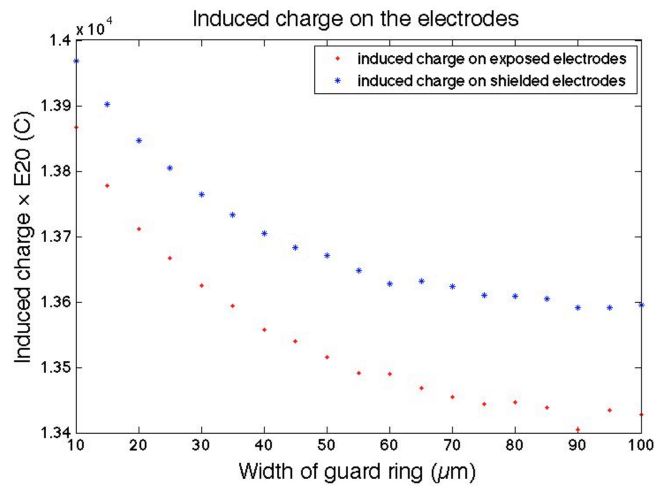

(a)

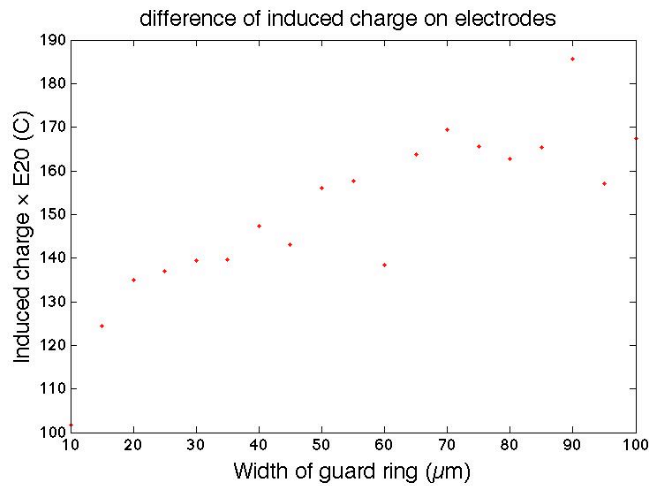

(b)

Figure 5.35. Guard ring on floating shutter design with rectangular cross-section.

5.5.4 Floating Shutter Design with Trapezoidal Cross-section

Figure 5.36 gives a similar result as that of the floating shutter with rectangular shutter cross-section. The amount of induced charge on both sets of the electrodes drops as the guard ring gets thicker, while the difference grows. As a result, a thicker guard ring is reasonable in this case.

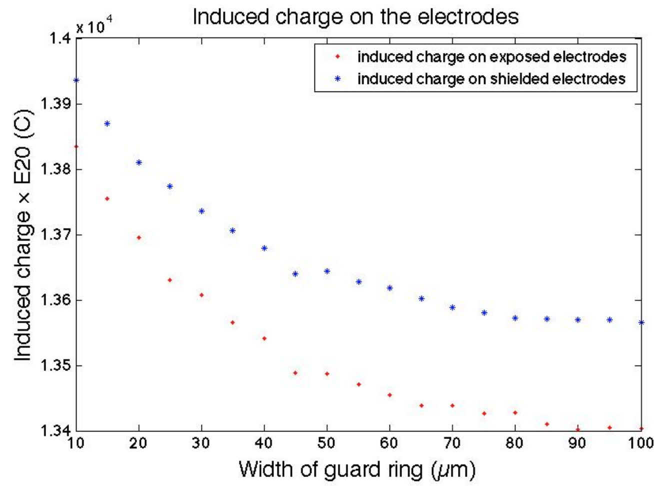

(a)

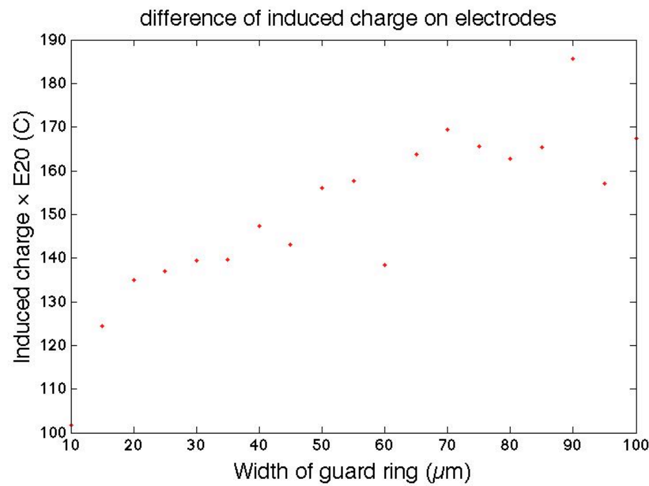

(b)

Figure 5.36. Guard ring on floating shutter design with trapezoidal cross-section.

5.5.5 Comparing between different designs

Figure 5.37 is the comparison between four different designs with same parameters. It is obvious that the a thicker guard ring, 100 μm thick in our design, especially with the floating shutter design, can result in a better output signal by keeping the interference from the fringing field at the edge of the shutter away from the electrodes.

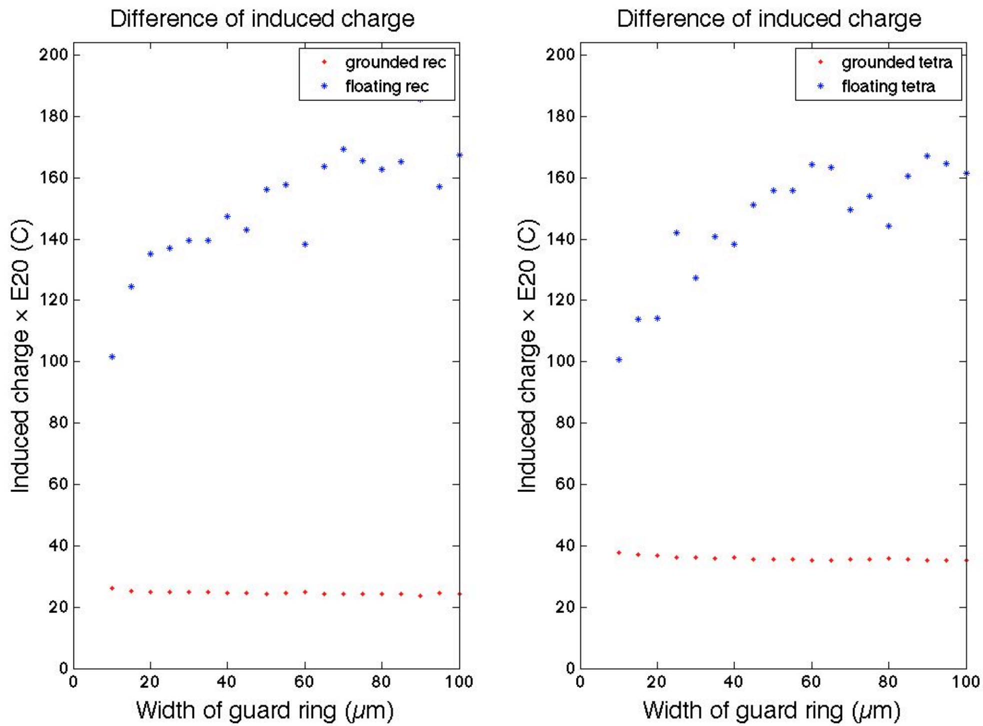

Figure 5.37. Comparing of different designs with guard ring.

5.6 Conclusion from the Simulation Results

Simulations have been done on the electrical features of the shutter designs. The results indicate that the floating shutter design surpasses the conventional ones dramatically on all aspects. Also, for each different parameter, the effect, in terms of

difference in amount of induced charge, is fully investigated and listed below. Note: the suggested dimensional value in Table 5-1 is based on a shutter with a 5 μm motion.

Table 5-1. Conclusion from the results of simulations.

Design	Parameter	Effect on difference in amount of induced charge	Suggested Value (μm)
Conventional Rectangular	S_w	Increases with the larger width of slit	7
	E_w	Decreases with larger electrode width	2
	t_s	Decreases with larger shutter thickness	4
	G	Increases initially when gap is extremely small, decreases after gap reaches 1um	2
	Guard Ring Width	No obvious change	100
Conventional Trapezoidal	S_w	Increases initially, but decreases at large width	7
	E_w	Decreases with larger electrode width	3
	t_s	Decreases with larger shutter thickness	4
	G	Increases initially when gap is extremely small, decreases after gap reaches 1.4um	2
	Guard Ring Width	No obvious change	100
Floating-Shutter Rectangular	S_w	Increases initially, the increment saturates at large width	6
	E_w	Decreases with larger electrode width	3
	t_s	Increases with larger shutter thickness	6
	G	Decreases dramatically with when gap increases	2
	Guard Ring Width	Increases with larger guard ring width	100
Floating-Shutter Trapezoidal	S_w	Increases initially, the increment saturates at large width	7
	E_w	Decreases with larger electrode width	3
	t_s	Increases with larger shutter thickness.	7
	G	Decreases dramatically with when gap increases	2
	Guard Ring Width	Increases with larger guard ring width	100

Chapter 6 Fabrication through PolyMUMPs Process

The new generation of non-resonant sensors were sent to be fabricated through the PolyMUMPs fabrication process via CMC Microsystems. Though these non-resonant sensors were not specifically designed for PolyMUMPs, it was felt that it might be worth giving it a try as the in-house fabrication was not ready during that time. A brief introduction of the fabrication process and some tests of the fabricated sensors will be presented in this chapter.

The new non-resonant sensors were simulated using COMSOL Multiphysics. Based on the original design [20], the mechanical structure of the sensor was optimized to give a 5 μm shutter displacement using genetic algorithm developed by Mark Roy [41]. The shutter slits and underlying electrode dimensions, were taken from the work of this thesis. Table 6-1 shows the main structural parameters of the new design and the original design [41].

Table 6-1. Main structure parameters of the new design and the original design

Sensor Design	Original	New Design
Actuator beam number	5	9
Actuator beam length (μm)	190	248
Actuator beam width (μm)	6	5
Actuator beam angle (μm)	4.5°	4°
Connecting beam length (μm)	95	164
Connecting beam width (μm)	5	5
Short beam length (μm)	20	54
Short beam width (μm)	3	10
Long beam length (μm)	375	1255
Long beam width (μm)	4	19
Spring number	2 × 4	3 × 4
Spring length (μm)	560	965
Spring width (μm)	20	4
Width of slit (μm)	20	4, 5, 6
Width of electrodes (μm)	20	4
Shutter displacement at 1V(μm)	~ 0.5 (non-resonant)	~ 5 (from simulation)

Figure 6.1 is the microscopic view of the part of the sensor and Figure 6.2 is the microscopic view of fabricated sensors.

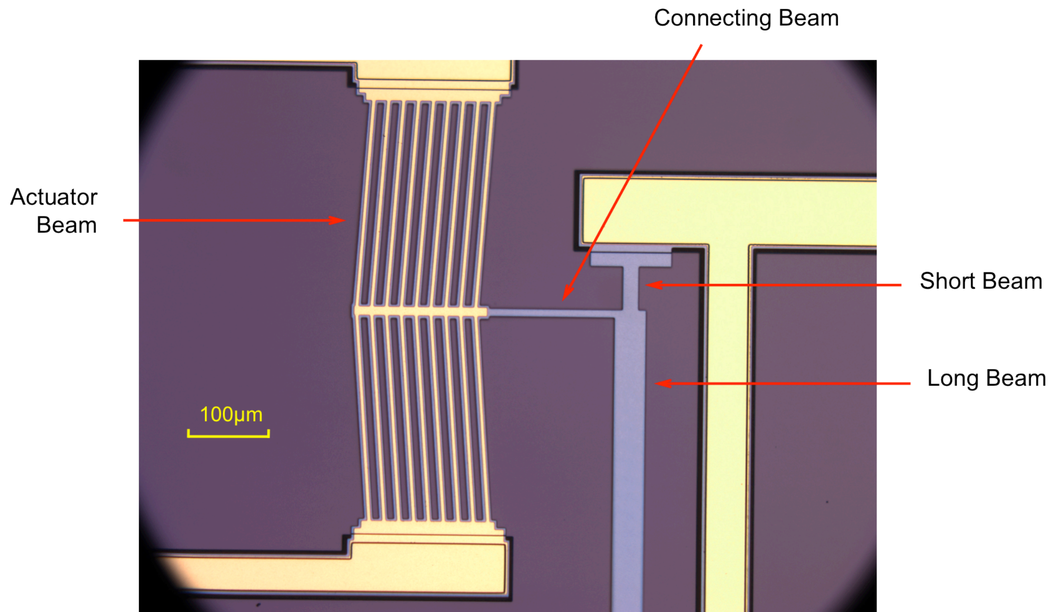

Figure 6.1. Microscopic view of the part of the sensor

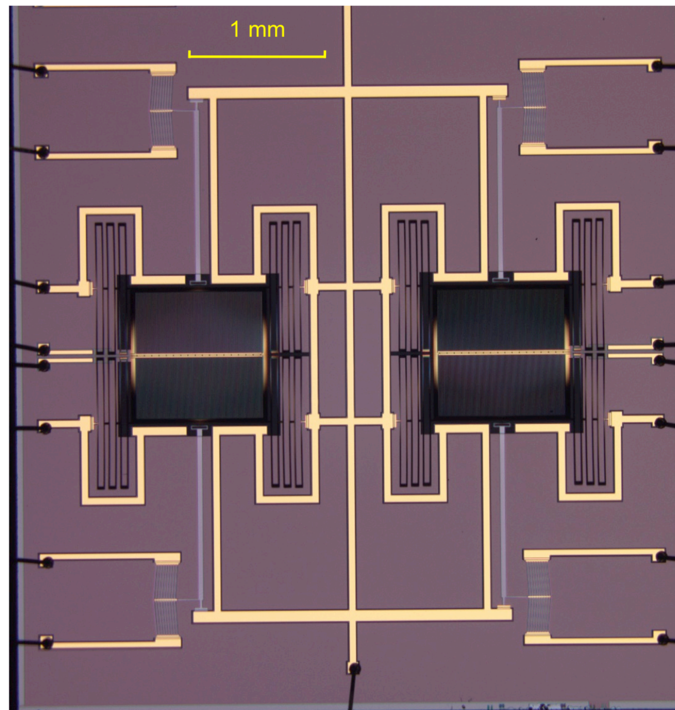

Figure 6.2. Microscopic view of the fabricated sensors

6.1 PolyMUMPs Fabrication Process

The PolyMUMPs process is now available through MEMSCAP Inc. [56]. The process steps are presented below. Figure 6.3 is the schematic view of each step.

a. A 600 nm silicon-nitride film is deposited on a 150 mm n-type silicon wafer which is heavily doped to enhance the conductivity. A 500 nm polysilicon layer, Poly 0, is then deposited on the nitride layer using LPCVD (low pressure chemical vapor deposition). This Poly 0 could be patterned using photolithography and etched in plasma etching. After the etch, a 2 μm PSG layer is deposited and patterned in a RIE and dimples are also etched into the PSG layer. This layer, known as First Oxide, works also as the sacrificial layer and will be removed at the end of the process to release the structure.
b. A 2 μm polysilicon layer, Poly 1, is deposited and patterned using a PSG mask and RIE. The PSG mask is highly doped and used as a doping source. Annealing is followed to dope the Poly 1 layer. After removal of the PSG mask, another PSG sacrificial layer, 750 nm in thickness, is deposited and patterned. This PSG player is named Second Oxide.
c. The third polysilicon layer, Poly 2, is deposited at a thickness of 1.5 μm and patterned again using a PSG mask and RIE. The PSG mask also works as the doping source. Annealing is followed to dope Poly 2 to make it conducting.
d. The final deposition layer is a 500 nm metal layer patterned with lift-off. The metal layer provides a good electrical routing and reflective surface.
e. The whole structure is merged in a 49% HF bath for 1.5 to 2 minutes to remove the sacrificial layer and release the structure. A DI bath, alcohol bath and annealing follows.

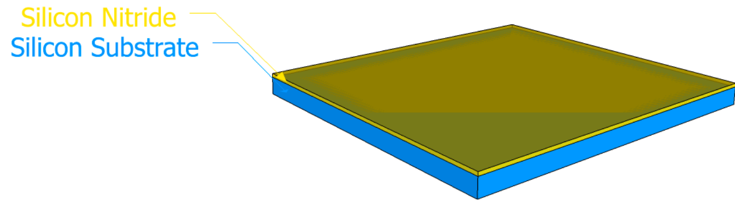

(a)

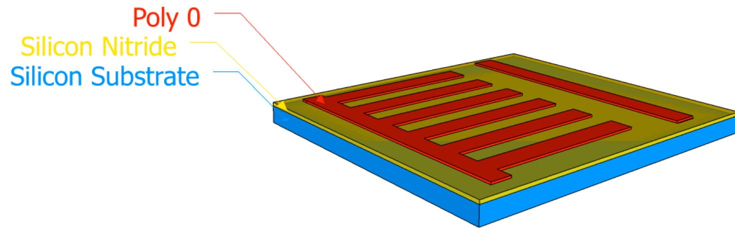

(b)

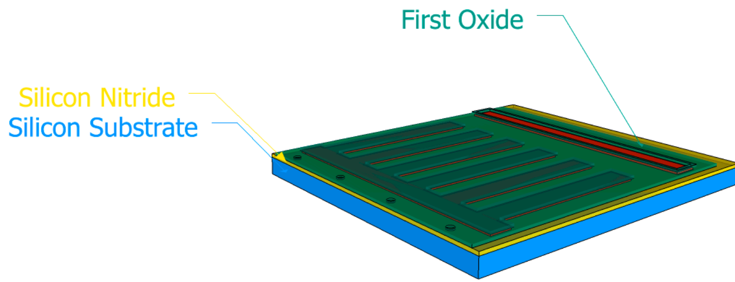

(c)

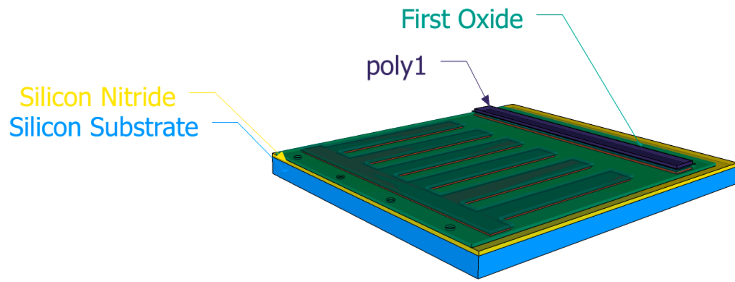

(d)

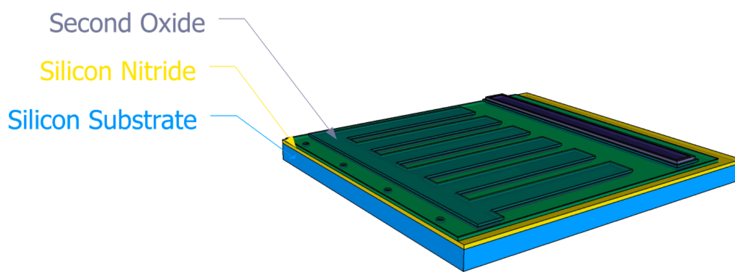

(e)

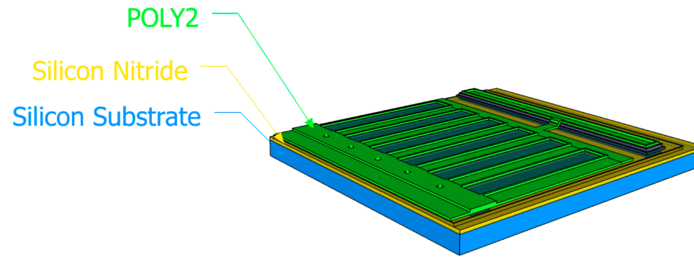

(f)

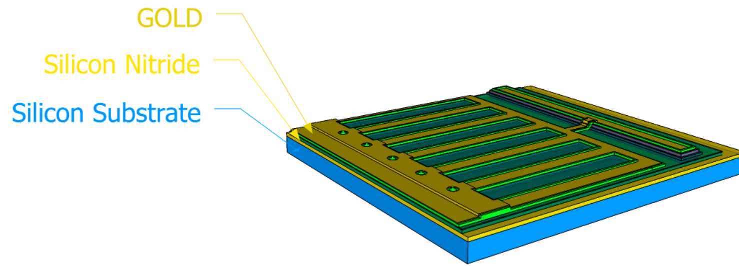

(g)

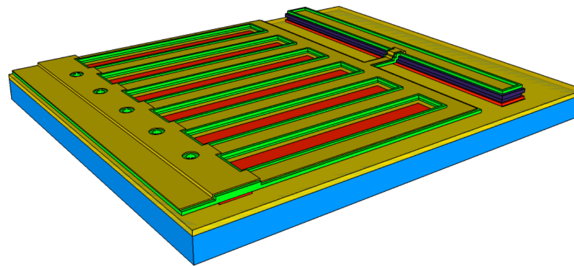

(h)

Figure 6.3 (a) Silicon nitride layer is deposited on the substrate. (b) Poly 0 is deposited and patterned. (c) First Oxide is deposited and patterned with dimples etched into the oxide. (d) Poly 1 is deposited and patterned. (e) Second Oxide is deposited and patterned. (f) Poly 2 is deposited and patterned. (g) Metal is deposited and patterned. (h) Structure released by removing the oxide layers.

6.2 Motion test of the fabricated sensors

The fabricated sensors were tested in a vacuum chamber to reduce the air damping. Figure 6.4 are the vacuum chamber, fabricated sensor with package, fixture, and the circuit used to test the sensor.

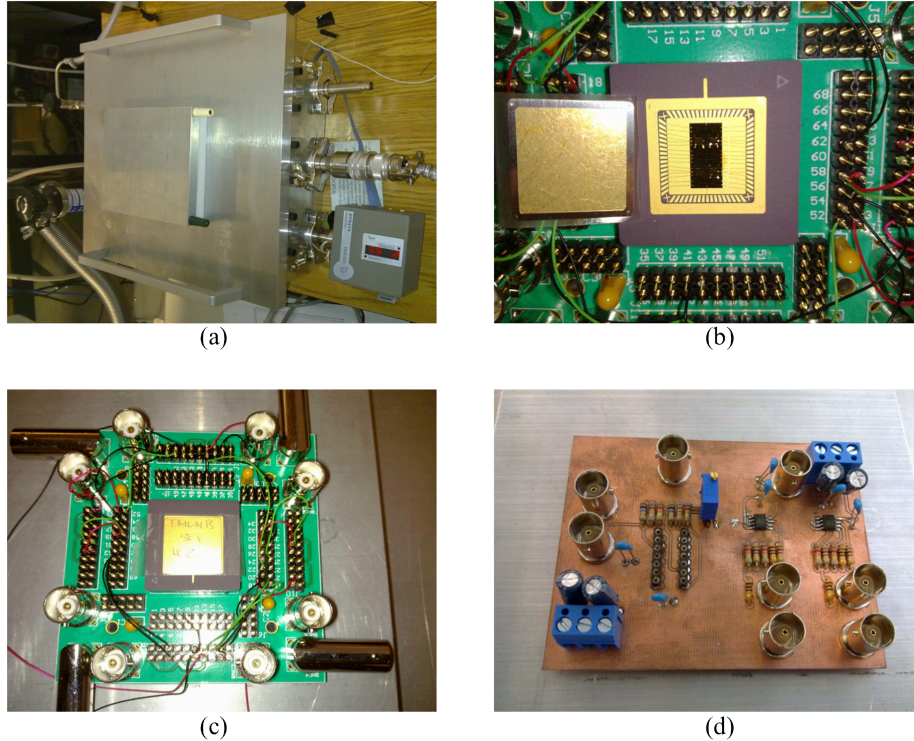

(a) (b) (c) (d)

Figure 6.4. (a) Testing chamber. (b) Sensor with package. (c) Fixture. (d) Circuit.

The sensor with its fixture and circuit board were placed in the vacuum chamber during test. The sensor was actually sitting on an aluminum support right beneath the lid of the vacuum chamber. The circuit used in the tests was developed based on the circuit design of Wijeweera [20]. The output of the sensor was connected to the signal input of a lock-in amplifier while the driving signal of the sensor was connected to the reference of the same lock-in amplifier. The reference was set at 2 times the driving signal.

In out tests, the driving signal was set to be $V_{p\text{-}p}$ = 0.7 V, f = 100 Hz. During the tests, the vacuum chamber was pumped down to 20 mTorr. In order to generate electric field that was measured, the lid of the chamber was biased at 15 V, while the other parts of the chamber were grounded, so was the aluminum support.

By applying the driving signal and the bias voltage on the lid of the vacuum chamber, a signal should have appeared. However, no obvious signal could be observed based on the reading of the lock-in amplifier. Later on, the output signal was connected to

a spectrum analyzer to measure the spectrum of the output signal. No peak could be observed at 200 Hz.

In order to figure out the problem, the operation of the sensors were examined using a Photomap 3D, (Fogale Nanotech.). The Photomap 3D is an optical interferometric sensor for 3D measurements with minimum vertical resolution smaller than 1Å [57]. Figure 6.5 shows the brief working principle of the optical interferometer.

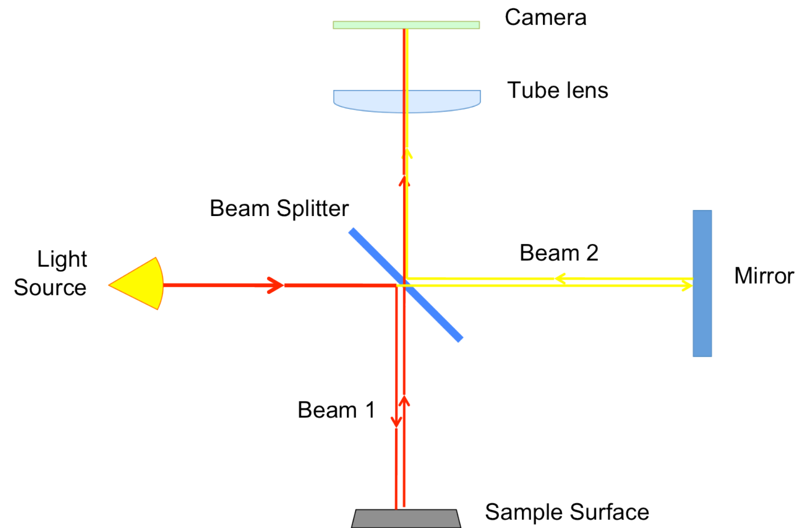

Figure 6.5.Working principle of the optical interferometer.

A beam of light is emitted by the light source and splitted into two beams, beam 1 and beam 2. While beam 1 propagates towards the sample surface and reflects back to the splitter, the beam 2 gets reflected by a mirror. Then, two beams are combined and the result image is sent to the camera through a tube lens [57]. The intensity of the combined beam is a function of the difference in distance of the two beams. As a result, interference fringes could be observed in the image.

A 0.7 V dc voltage was applied over the thermal actuator of the sensor. The sensors were originally designed to work with 1 V dc bias. However, 0.7 V dc bias was selected for precaution. With 0.7 V dc bias, the sensor which originally gives a 5 μm displacement with 1.0 V should have a 2.5 μm displacement. Snapshots were taken to

compare when no potential is applied. Pictures of several critical structures are presented below along with the measurements.

Figure 6.6 are the pictures of the connecting beam and the shutter of both situations. The yellow points in both Figure 6.6 (a) and (b) are the same point of the structure that were measured when the actuators were biased and unbiased respectively. The measurements were carried out along the red line in both plot of Figure 6.6.

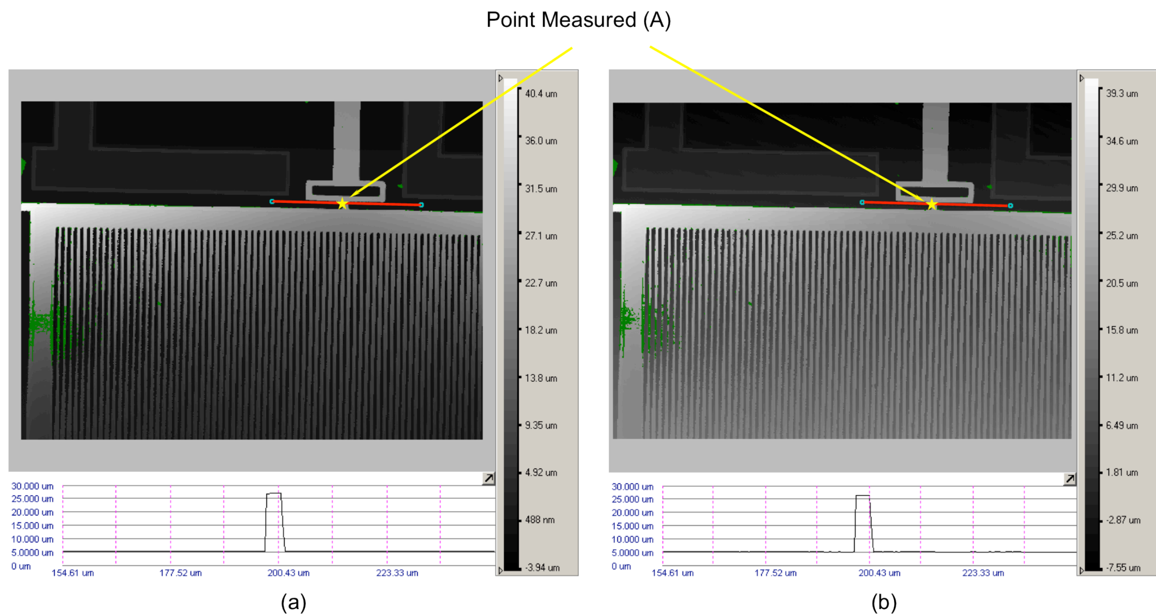

Figure 6.6. Result of the motion test on shutter and connecting beam (a) with actuator unbiased; (b) with actuator biased.

From Figure 6.6, the coordinates of the point measured in both situations could be found. When the actuator is unbiased, the coordinate of point $A_{unbiased}$ = (197.22 μm, 62.726 μm), while A_{biased} = (196.87 μm, 62.718 μm). The value of two points are the distance from the start points of the cut lines in red, which in both plots share the same coordinates. Therefore, the difference of $A_{unbiased}$ and A_{biased} indicates the lateral displacement of the shutter, which is around 0.35 μm. The vertical displacement could also be found from the data, which is around 0.435 μm.

The lateral displacement is smaller than expected. According to the simulations done by Mark Roy [41], the expected displacement should equal 2.5 µm when 0.7 V dc voltage is applied. With this shutter displacement, the shutter can not fully cover and uncover the electrodes beneath it, and the output can be greatly reduced. Further research on this issue will be presented in the following part of this chapter.

The 3-D views of the same structure were plotted in Figure 6.7. A curved shutter could be observed. This reveals a problem with the fabricated sensors. The edge of the shutter tilts greatly. Ideally, the shutter should be in plane, 2.75 µm above the Poly 0, and so 3.25 µm above the nitride layer which is the ground level in the 3-D plots. In reality, the measurement showed that the shutter deforms and the edges are about 45 µm above the ground level. This can also be a reason that why the MEFM devices failed to measure the electric field. A deformed shutter increases the gap between the shutter and the electrodes, and according to the simulations presented in Chapter 5, increasing the gap will lead to a dramatic decrease in the output signal.

To summarize, a lifted and deformed shutter and greatly reduced horizontal shutter displacement are reasons that the sensor fails to measure the electric field.

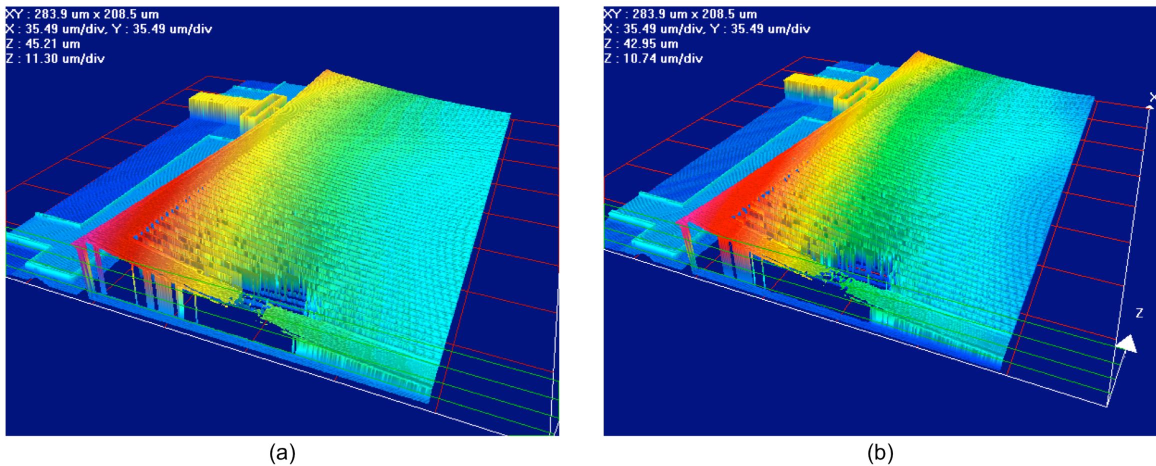

Figure 6.7. 3-D view of the shutter structure. (a) with actuator unbiased. (b) with actuator biased.

6.2.1 Reason of reduced horizontal displacement

- Effect of Intrinsic Stress

An investigation was done to see why motion so greatly reduced. Figure 6.8 shows the measurement of a thermal actuator of the fabricated sensor with voltage applied and unapplied respectively. Point B in both plots of Figure 6.8 along the red line gives the displacement of the thermal actuator.

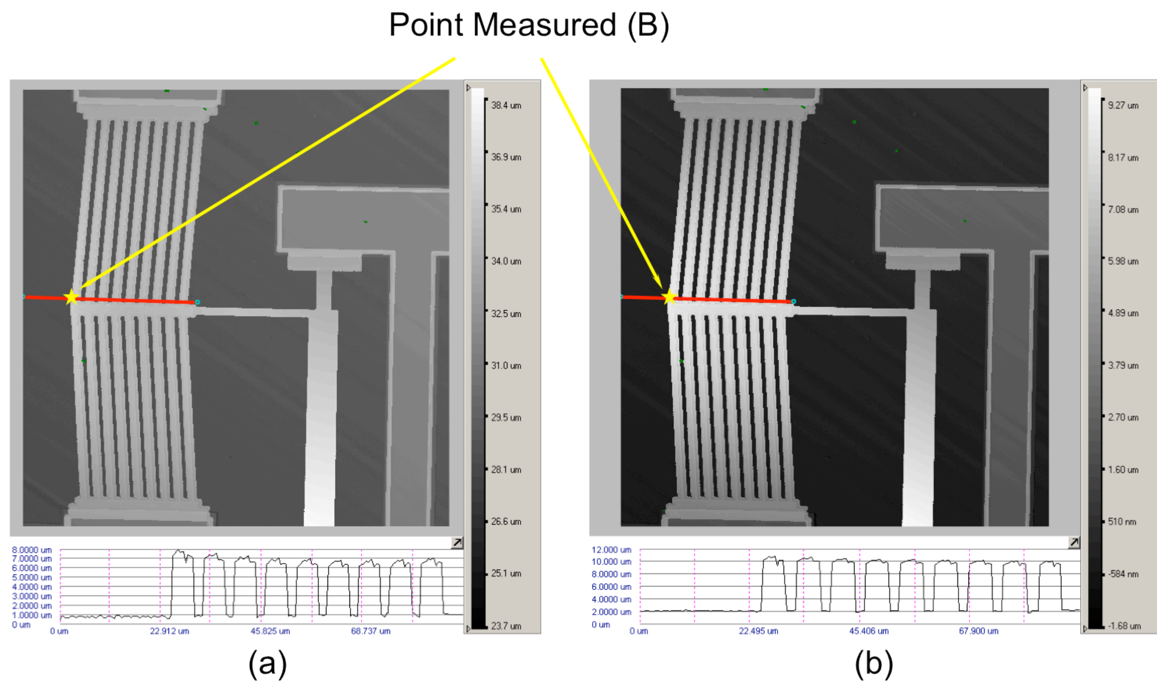

Figure 6.8. Result of the motion test on the thermal actuator. (a) when not biased. (b) when 0.7 V dc voltage applied.

In Figure 6.8, $B_{unbiased}$ = (25.168 μm, 109.81 μm) is the coordinate of the left edge of thermal actuators which is not biased. When biased, B_{biased} = (24.843 μm, 110.11 μm). The difference in the values of $B_{unbiased}$ and B_{biased} is the horizontal displacement of the thermal actuator when voltage is applied. An approximately 0.4μm horizontal displacement is observed. This is smaller than the expected displacement of the thermal actuator from the simulations. In actual operation the deformation happens more in the vertical direction instead of in the horizontal direction. From Figure 6.8, an

approximately 1.4 μm motion in the vertical direction could be observed. A much clearer 3-D view is shown in the Figure 6.9.

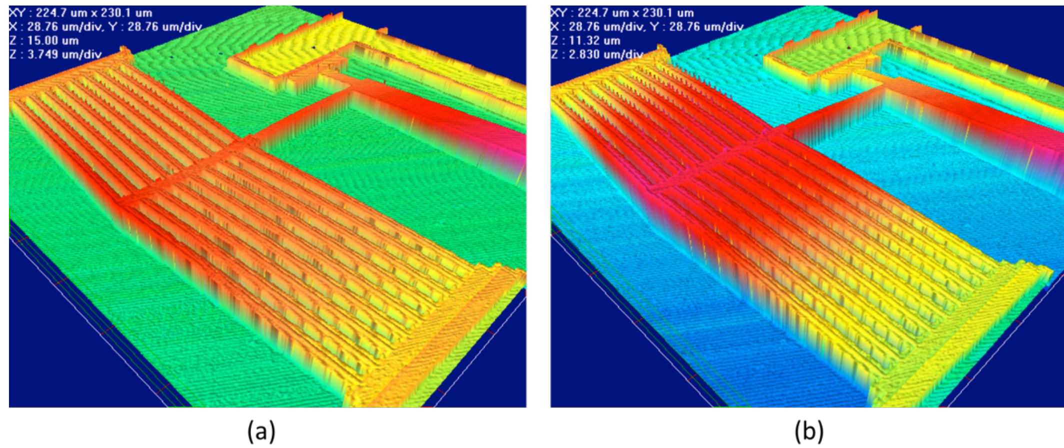

Figure 6.9. 3-D view of the actuator (a) not biased. (b) biased.

From Figure 6.9, one can see that the actuator buckles up more when voltage is applied. This explains the shrink in horizontal displacement, since the actuator tends to buckle up instead of moving horizontally. Simulations were done on this issue, and they revealed that when biased, the thermal actuator made from polysilicon and metal has approximately three times displacement in the vertical direction compared to that in the horizontal direction. This is illustrated in Figure 6.10.

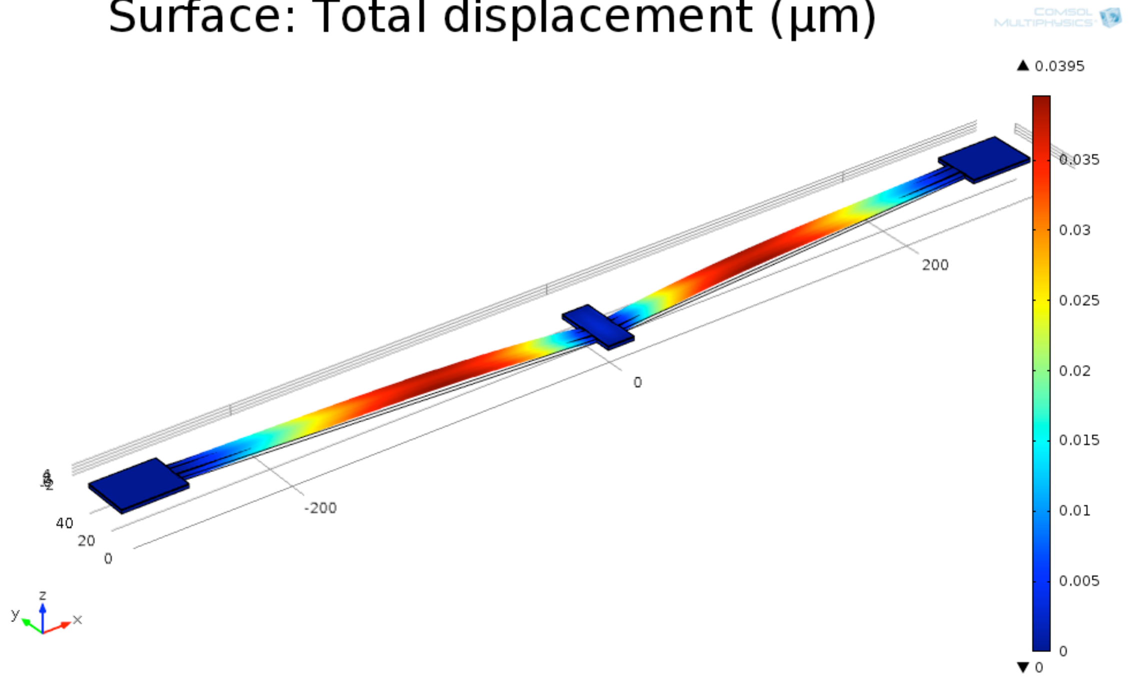

(a)

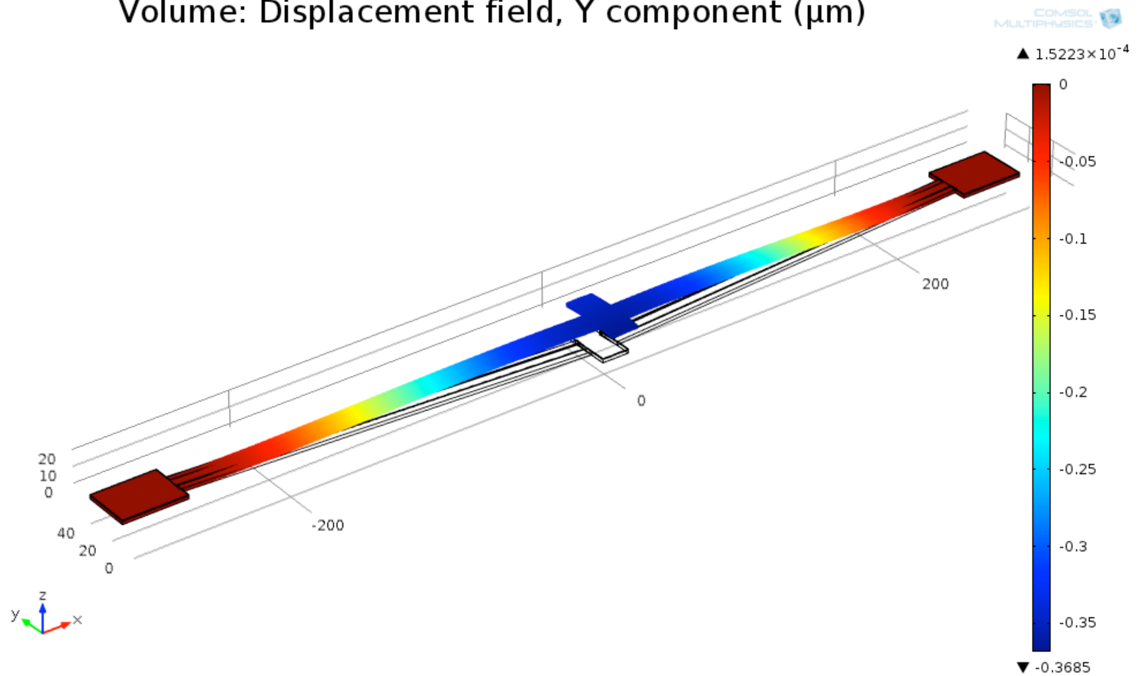

(b)

Figure 6.10. Displacement of the thermal actuator from simulations. (a) when unbiased. (b) when biased.

The intrinsic stress in polysilicon layer and metal layer also leads to the lifting of the lever and spring system, as shown in the Figure 6.11.

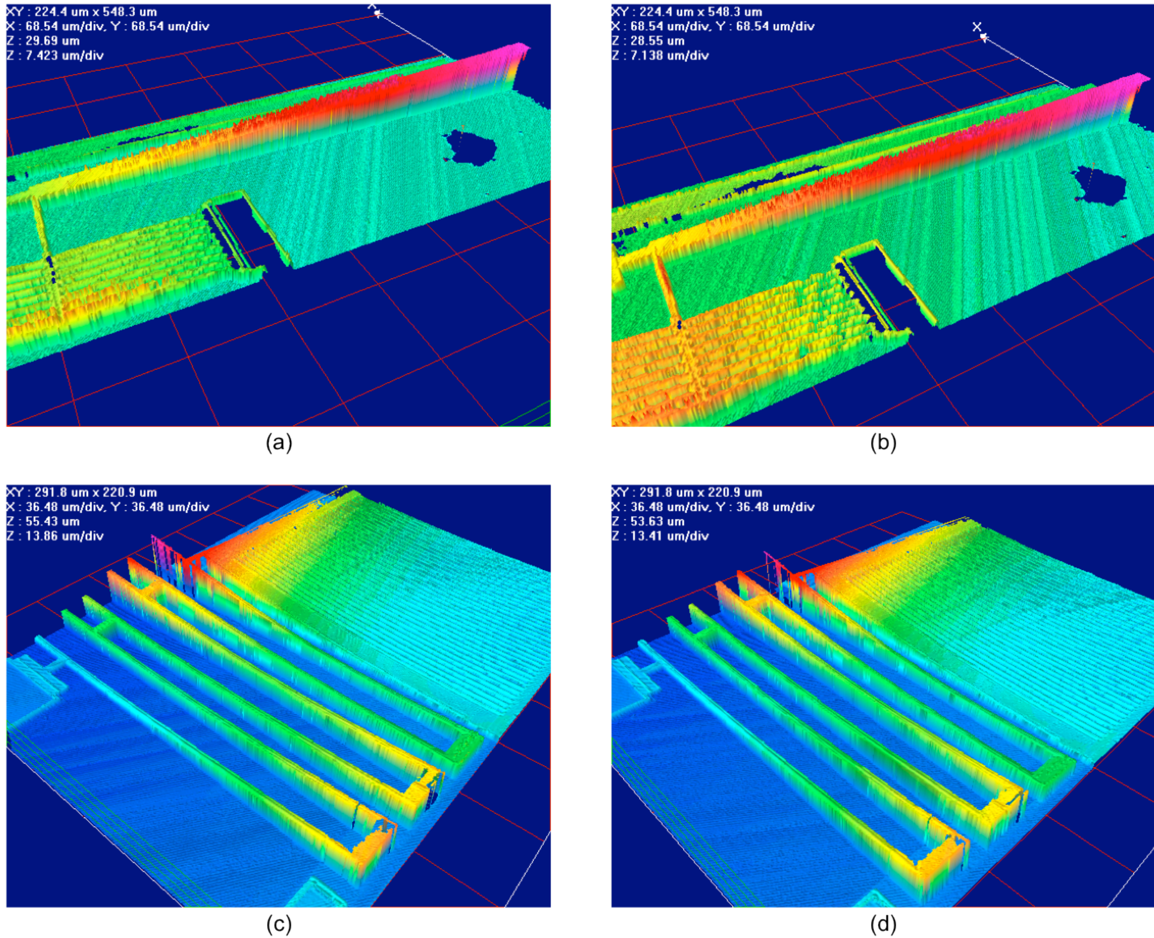

Figure 6.11. Suspension of the sensor. (a) Lever system with actuator unbiased. (b) Lever system with actuator biased. (c) Springs with actuator unbiased. (d) Springs with actuator biased.

In Figure 6.11, it is obvious that all components of the suspension system are lifted up greatly. However, no apparent curvature in shape can be observed on the lever, while bending is seen in the springs, shutter, and thermal actuators. The springs, shutter and thermal actuators are coated with metal and the lever system is left uncoated. This indicates that the deformation might be caused by stress difference between the polysilicon and metal layers. The typical intrinsic stress of the Poly 2 is -10 MPa while the typical intrinsic stress of the Metal layer is 50 MPa based on the data in the

PolyMUMPs manual [56]. It is clear that a stack of layers with sufficiently different intrinsic stress could cause deformations shown in the Figure 6.11. This deformation also changes the spring constant of the whole structure that was designed originally based on the simulations without considering the stress within layers.

Change in structure

It should be mentioned that the width of springs and lever systems were doubled compared to the original design to increase the surviving chance of the structure through the fabrication process. The connection spring at the end of the beam of the lever system provides the cantilever with some freedom of movement. This makes it valid that the cantilever could be considered as a beam spring fixed at one end. The spring constant of this kind of beam spring is given below:

$$F = E\frac{wt^3}{4L^3} \tag{6.1}$$

where E is the young's modulus, w is the width of the spring, in our case is the thickness of the cantilever, t is the thickness of the spring and is the width of the cantilever in our case, and L is the length of the spring. Doubling the width leads to a spring constant eight times larger than before. The measurements indicate that the lever system is too stiff to conduct significant displacement motion from the thermal actuator to the shutter.

Evidence that this is a problem can be seen in the photos of the sensor taken after the sensor was powered by a 0.7 V peak-to-peak ac power at 100 Hz for couple of hours. Structure failure, shown in Figure 6.12, can be detected at the connecting beam between thermal actuator and lever system.

Connecting beam of actuator and lever

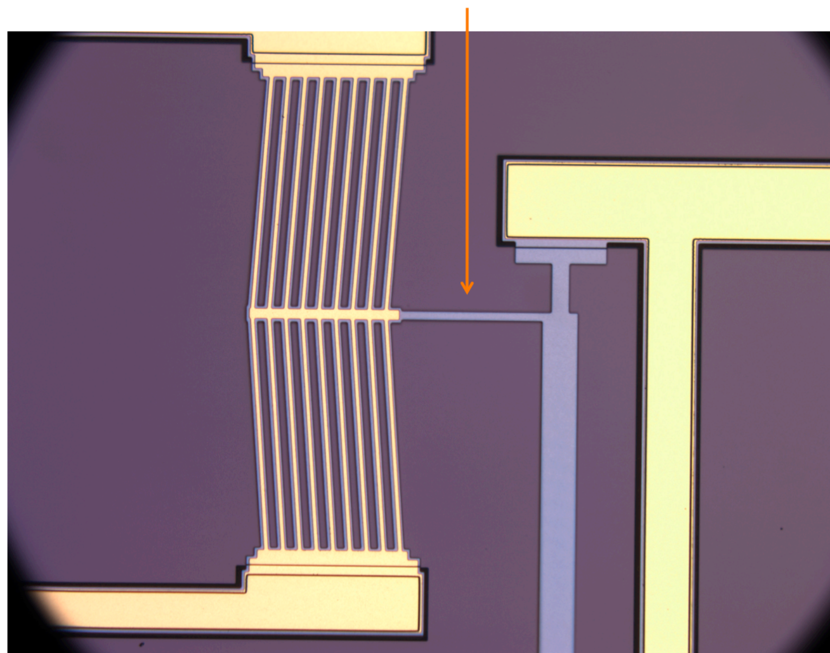

(a)

Connecting beam removed

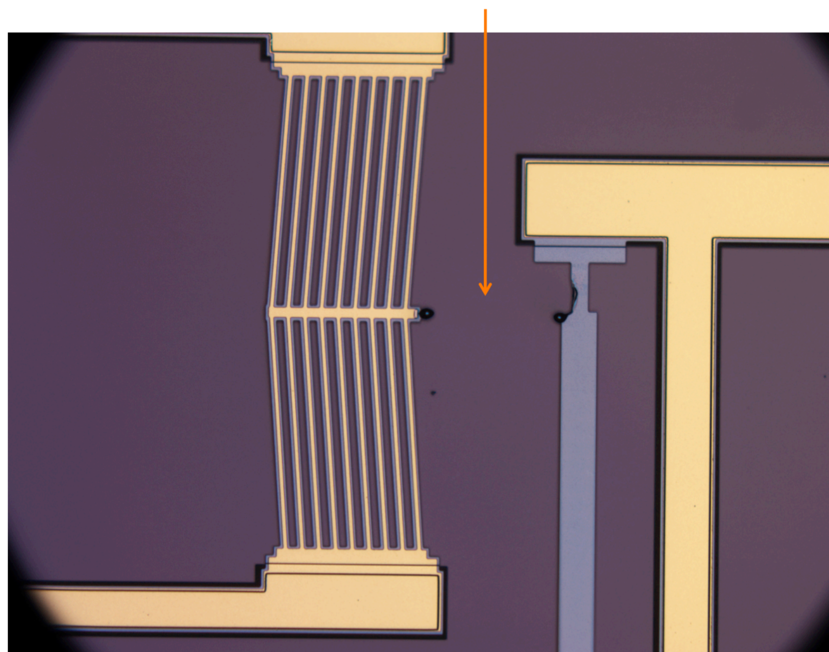

(b)

Figure 6.12. Structure of the actuator and lever under microscope. (a) before testing. (b) after testing.

The pictures are taken using an Olympus BX51 microscope with digital video camera. Comparing Figure 6.12 (a) and 6.12 (b), one can see that the connecting beam is broken while other components are generally unharmed. When biased, with the lever system too stiff, the thermal actuator loads the connecting beam and eventually causing it to fail.

6.3 Summary

The sensor designs were fabricated through the PolyMUMPs fabrication process and were tested. The results are not quite good as expected. The intrinsic stress in the polysilicon and metal layers caused the deformation of the structure. The shutter was deformed and was around 45 μm above the plane it should be in, which, as could be easily seen from the simulation on the gap between shutter and electrodes in Chapter 5, eliminated the output signal. Also a greatly reduced structure thickness, 2 μm, compared to the 10 μm thickness of the sensor of last generation, reduces the stiffness of the sensor structure in the vertical direction, make it easy to move in the vertical direction instead of lateral direction. Moreover, the change in the designs, doubling the width of beams, in order to increase the possibility of surviving further increased the stiffness in the lateral direction, keeping it from moving in the desired direction. In general, other fabrication processes based on single crystal silicon are suggested, similar to the device of Wijeweera [20], which was discussed in Chapter 3.

Chapter 7 Conclusion

7.1 What has been done

In this thesis, the modifications of the previous sensor designs are introduced. With these modifications, the drawbacks of the previous sensor designs could be overcome.

The fabrication process used to fabricate the previous sensor designs is also presented. Based on that fabrication process, a similar in-house fabrication process was investigated. The lithography and plasma etch recipe are presented in this thesis. Based on the study of the black silicon method [43], a plasma etch with three etchants (SF_6, O_2, CHF_3) was investigated and recipe was developed. From the plasma etch experiments, an approximately 0.79 anisotropy was achieved with the parameters listed in Table 7-1：

Table 7-1. Plasma etch recipe and result

Pressure (mTorr)	RIE (W)	ICP (W)	SF_6 Flow Rate (sccm)	O_2 Flow Rate (sccm)	CHF3 Flow Rate (sccm)	Undercut	Anisotropy
50	50	100	30	15	15	17%	0.79

The results and the analysis of simulations in order to optimize the structure of the shutter to give a better sensitivity are also discussed in this thesis. Four different designs of the shutter are listed and looked through in cases of four different structure parameters. For different designs, the results are presented below.

Grounded Shutter Design

Width of slit (S_w): The output increases when width of slit increases. Therefore, ideally, the width of slit should be as large as possible. However, in practice, a large width of slits can reduce the structure strength of the shutter and cause

problem in lithography and etching process. As a result, in our sensor design, a 6 μm to 7 μm width of slit are selected.

Width of electrode (E_w): According to the discussion, a width of electrode around 2 μm to 3 μm is reasonable.

Shutter thickness (t_s): Ideally, the shutter of grounded shutter sensor design should be as thin as possible. However, a sensor with a very thin shutter is hard to be fabricated and fragile. Thus, a 4 μm thick shutter is picked.

Gap between the shutter and electrodes (G): A 1 μm gap is optimal based on the simulation. But that is not achievable in the fabrication process. In our design, a 2 μm gap is selected.

Floating Shutter Design

Width of slit (S_w): A 6 μm width of slit should be selected.

Width of electrode (E_w): The output signal increases when the width of electrode decreases. However, the benefit saturates when the width of electrode is smaller than 3 μm. Therefore, a 3 μm width of electrode should be selected.

Shutter thickness (t_s): Although the output signal increases with a thicker shutter, a thicker shutter can lead to difficulties in etching, and the benefit saturates when the shutter is thicker than 6 μm. Thus, a 6 μm shutter thickness is selected.

Gap between the shutter and electrodes (G): A 2 μm gap between the shutter and the electrodes is adopted.

Grounded Shutter Design with Trapezoidal Shutter Cross-section

Width of slit (S_w): A slit with 6 μm to 7 μm in width is selected.

Width of electrode (E_w): A 3 μm width of electrode is optimal.

Shutter thickness (t_s): A 4 μm thick shutter is selected with consideration of practical fabrication.

Gap between the shutter and electrodes (G): A 2 μm gap is selected.

Floating Shutter Design with Trapezoidal Shutter Cross-section

Width of slit (S_w): A slit with 6 μm to 7 μm in width is selected.

Width of electrode (E_w): A 3 μm width of electrode is optimal.

Shutter thickness (t_s): A shutter with 6 μm to 7 μm thickness is selected with consideration of practical fabrication.

Gap between the shutter and electrodes (G): A 2 μm gap is selected.

Width Guard Ring

For all designs, a thicker guard ring is beneficial. In our designs, a guard ring with 100 μm width is selected.

The comparison between four designs indicates that the floating shutter designs surpass the grounded shutter designs greatly, approximately 4 to 5 times the output signal with the same structure parameter. While within the grounded shutter design, the design with trapezoidal shutter cross-section gives an approximately 50% better result than the one with rectangular shutter cross-section.

7.2 Future Work

The next step will be in-house fabrication and the testing of the modified sensor designs. An improved in-house fabrication process could be helpful if available. With current fabrication process, it is impossible to modify the top metal layer after the release of the structure for the sensor may not be able survive the wet etch. This could be overcome by a chlorine based plasma etch after the releasing.

As the sensor is no longer working at its resonant frequency, the vacuum package used to be inevitable may not be essential any more. A careful test of the performance of the new generation of sensor with the varying air pressure is quite necessary to verify the point. And if so, the sensor could be packaged without high vacuum or even totally get rid of the vacuum. A wider scope of application might be ensured.

A further improvement could be the integration of the sensor and the electronics. Currently, the sensor is connected to the electronics by wires. The impedance of the wires, relatively large compared to that of between pins of the package, reduces the output signal which is originally very weak. An integrated electronics could chop the impedance greatly and therefore a better performance. Moreover, an integration of the sensor and electronics could dramatically shrink the size of the total system.

Finally, an array of sensors would be handy in the real measurements. Thanks to the reduced size compared to the conventional field mill, tens or hundreds of sensors could be put together to form a sensor array that could undoubtedly improve the sensitivity and accuracy.

References

[1]. P. Sarma Maruvada, R.D. Dallaire, and R. Pedneault, 'Development of Field-Mill Instruments for Ground-Level and Above-Ground Electric Field Measurement Under HVDC Transmission Lines, IEEE Transactions on Power Apparatus and Systems, March 1983, Vol. PAS-102, Issue 3, pp. 738-744.

[2]. Isaias Ramirez-Vbzquez, Ramiro Hemhdez-Corona, and Gerardo Montoya-Tena, 'Diagnostic of nonceramic insulators aged in a salt fog chamber by using electric field sensor', Conference Record of the 2004 IEEE International Symposium on Electrical Insulation, Indianapolis, IN USA, 19-22 September 2004, pp. 471-474.

[3]. G. H. Vaillancourt, S. Carignan, and C. Jean, "Experience with the Detection of Faulty Composite Insulators on High-Voltage Power Lines by the Electric Field Measurement Method, IEEE trans. on power delivery, Apr. 1998, Vol. 13, pp. 661-666,.

[4]. Chunrong Peng, Pengfei Yang, Shiguo Liu, Haiyan Zhang, Ke Feng, and Shanhong Xia, 'Detecting internal defect of non-ceramic insulators using a novel micromachined electric field sensor', IEEE 24th International Conference on Micro Electro Mechanical Systems (MEMS), Cancun, MEXICO, January 23-27, 2011, pp 561-564.

[5]. Hitoshi Okubo, Atsushi Sawacla, Katsumi Kato, and Masayuki Hikita, 'Direct Measurement of Electric Field using Kerr Electro-Optic Method in Transformer Oil Pressboard Composite System at dc Polarity Reversal', Conference Record of the 1998 IEEE International Symposium on Electrical Insulation, Arlington, Virginia, USA, June 7-10, 1998, Vol. 2, pp. 486-489.

[6]. C. James Dahn, B. N. Reyes, Abdollah Kashani, and Jacob Finkelshtein, 'Electrostatic Hazards of Explosive Propellant And Pyrotechnic Powders', Electrical Overstress/Electrostatic Discharge Symposium Proceedings, 6-8 Oct. 1998, pp. 139-150.

[7]. G. Luttgens and S. Luttgens, 'Preventing electrostatic hazards of flexible intermediate bulk containers', Conference Record of the 2000 IEEE Industry Applications Conference, 2000, Vol. 1, pp. 666-669.

[8]. M.Glor, 'Electrostatic ignition hazards associated with FIBC filling or emptying and presently available FIBC safety design types', IEE Colloquium on Hazards in Powder Handling with FIBCs: Standards, Measurements and Case Studies (Digest No. 1997/001), 17 Apr. 1997, pp. 2/1-2/3.

[9]. BP International, 'Hazards of electricity and static electricity', Institution of Chemical Engineers, 2006.

[10]. Keith Campden, 'Electrostatics field of interest', IEE Review, 17 Oct. 1991, Vol. 37, Issue 10, pp. 335-338.

[11]. Hong-Lae Kim, Min-Gu Kim, Chungkeun Lee, Myoungho Lee, Yong-Jun Kim, 'Miniaturized One-Point Detectable Electrocardiography Sensor for Portable Physiological Monitoring Systems', IEEE Senor Journal, Jul. 2012, Vol. 12, Issue 7, pp. 2423-2424.

[12]. Koichi Shimizu, Hideto Endo, and Goro Matsumoto, 'Fundamental Study on Measurement of ELF Electric Field at Biological Body Surfaces', IEEE Transactions on Instrumentation and Measurement, Jun. 1989, Vol. 38, Issue 3, pp. 779-784.

[13]. Charles Poole and Dimitrios Trichopoulos, 'Extremely low-frequency electric and magnetic fields and cancer', Cancer Causes and Control, Jul. 1991, Vol. 2, No. 4, pp. 267-276.

[14]. J. Schuz, 'Exposure to electromagnetic fields and cancer: The epidemiological evidence', General Assembly and Scientific Symposium, 13-20 Aug. 2011, pp. 1-4.

[15]. Yi Guo-Sheng, Wang Jiang, Han Chun-Xiao, Liu Yu-Liang, Deng Bin, and Wei Xi-Le, 'Bifurcation analysis of a minimal neuron to ELF AC electric field', 30th Chinese Control Conference, 22-24 Jul. 2011, pp. 594-598.

[16]. 'ENVIRONMENTAL HEALTH CRITERIA 35: EXTREMELY LOW FREQUENCY (ELF) FIELDS', World Health Organization, Geneva, 1984

[17]. R. Vishnu, V. Anil Kumar, T.S. Sreekanth, V.N. Subi Symon, S. Murali Das, and G. Mohan Kumar, 'Formation of Thunderclouds in a Region of High Lightning Incidence, Inferred from AWS, Ceilometer and an Electric Field Mill', 7th Asia-Pacific International Conference on Lightning, Chengdu, China, 1-4 Nov. 2011, pp. 135-139.

[18]. Lorraine Raymond Barnum, Jeffrey C. Bailey, Douglas M. Mach, Michael F. Stewart, and Hugh J. Christian, 'Study Of Triggered Lightning: The Airborne Field Mill Program', 10th Annual International Geoscience and Remote Sensing Symposium, 'Remote Sensing Science for the Nineties'., 20-24 May 1990, pp. 1901-1904.

[19]. J. Singye, K. Masugata, T. Murai, I. Kitamura, and K. Kontani, 'Thunderstorm tracking system using neural networks and measured electric fields from few field mills', IEEE International Symposium on Circuits and Systems, 23-26 May 2005, Vol. 5, pp. 5126-5129.

[20]. Gayan Wijeweera, 'Design of A Micromachined Electric Field Sensor Using A Thermal Actuating Shutter', M.Sc. thesis, Department of Electrical and Computer Engineering, University of Manitoba, Winnipeg, Manitoba, 2008.

[21]. M. N. Horenstein and P. R. Stone, 'A micro-aperture electrostatic field mill based on MEMS technology,' J. Electrostat., May 2001, Vol. 51–52, pp. 515–521.

[22]. C. Peng, X. Chen, Q. Bai, L. Luo, and S. Xia, 'A novel high performance micromechanical resonant electrostatic field sensor used in atmospheric electric field detection', 19th IEEE Micro Electro Mechanical Systems Conf., Istanbul, Turkey, Jan. 2006, pp. 698–701.

[23]. P. S. Riehl, K. L. Scott, R. S. Muller, R. T. Howe, and J. A. Yasaitis, 'Electrostatic charge and field sensors based on micromechanical resonators,' IEEE J. Microelectromechan. Syst., Oct. 2003, Vol. 12, No. 5, pp. 577–589.

[24]. Xianxiang Chen, Chunrong Peng, Hu Tao, Chao Ye, Qiang Bai, Shaofeng Chen, and Shanhong Xia, 'Thermally driven micro-electrostatic fieldmeter', Sensors and Actuators A: Physical, 20 Nov. 2006, Vol. 132, Issue 2, pp. 677–682.

[25]. C. H. Hsu and R. S. Muller, 'Micromechanical Electrostatic Voltmeter', International Conference on Solid-State Sensors and Actuators, June 1991, pp. 659–662.

[26]. Mark N. Horenstain and Patrick R. Stone, 'A micro-aperture electrostatic field mill based on MEMS technology', Journal of Electrostatics, May 2001, Vol. 51-52, pp. 515-521.

[27]. 'IEEE Recommended Practice for Instrumentation: Magnetic Flux Density and Electric Field Strength Meters—10 Hz to 3 kHz', IEEE Std 1308-1994, 1995

[28]. Hamasaki, H., Gotoh, H., Katoh, M., and Takeuchi, S., 'OPSEF: An Optical Sensor for Measurement of High Electric Field Intensity,' Electronics Letters, 22 May 1980, Vol. 16, Issue 11, pp. 406–407.

[29]. K. Hidaka, 'Progress in Japan of space charge field measurement in gaseous dielectrics using a Pockels sensor', IEEE Electrical Insulation Magazine, Jan.-Feb. 1996, Vol. 12, Issue 1, pp. 17–28.

[30]. I. Zaldívar-Huerta, J. Rodríguez-Asomoza, 'Electro-Optic E-field Sensor Using an Optical Modulator', Electronics, 14th International Conference on Communications and Computers, 16-18 Feb. 2004, pp. 220-222.

[31]. Sven P. Hörnfeldt, 'DC-probes for electric field distribution measurements', IEEE Transactions on Power Delivery, Apr. 1991, Vol. 6, No.2, pp. 524-529.

[32]. K. Johansson, L. Walfridsson, U. Gäfvert, B. Källstrand, and S. Hörnfeldt, 'Probe for measurements of the DC electric field in air around high voltage apparatus', 2010 Annual Report Conference on Electrical Insulation and Dielectric Phenomena, 17-20 Oct. 2010, pp. 1-4.

[33]. Charles J. Miller, Jr., 'The Measurement of Electric Fields in Live Line Working', IEEE Transactions on Power Apparatus and System, Apr. 1967, Vol. Pas-86, Issue 4, pp. 493-498.

[34]. J.N. Chubb, 'Two new designs of field mill fieldmeter not requiring earthing of rotating chopper', IEEE Trans. Ind. Appl., Nov/Dec. 1990, Vol. 26, Issue 6, pp.1178-1181.

[35]. D. M. Taylor and P. E. Secker, 'Industrial Electrostatics: Fundamentals and Measurements', John Willey & Sons Inc., New York, 1994, ISBN-0-471-95233-8.

[36]. John Chubb Instrumentation, http://www.jci.co.uk.

[37]. Gayan Wijeweera, Behraad Bahreyni, Cyrus Shafai, Athula Rajapakse, and David R. Swatek, 'Micromachined Electric-Field Sensor to Measure AC and DC Fields in Power Systems', Power & Energy Society General Meeting, IEEE, 26-30 Jul. 2009, pp. 1.

[38]. Lejeune, L. Chérigier-Kovacic, and F. Doveil, 'Lyman-a radiation of a metastable hydrogen beam to measure electric fields', Applied Physics Letters, Oct. 2011, Vol. 99, Issue 18, pp. 181502-181502-3

[39]. Pengfei Yang, Chunrong Peng, Haiyan Zhang, Shiguo Liu, Dongming Fang, and Shanhong Xia, 'A high sensitivity SOI electric-field sensor with novel comb-shaped microelectrodes', 16th International Solid-State Sensors, Actuators and Microsystems Conference, 5-9 Jun. 2011, pp. 1034-1037.

[40]. A. Roncin, C. Shafai, and D.R. Swatek, 'Electric field sensor using electrostatic force deflection of a micro-spring supported membrane", Sensors and Actuators A: Physical, 23 Sep. 2005, Vol. 123-124, pp.179–184.

[41]. Mark Roy, 'Design Optimization of a Microelectromechanical Electric Field Sensor Using Genetic Algorithms', M.Sc. thesis, Department of Electrical and Computer Engineering, University of Manitoba, Winnipeg, Manitoba.

[42]. 'Introduction to MicraGEM: A Silicon-on-Insulator Based Micromachining Process', 3rd ed., Canadian Microelectronics Corporation, December 2004.

[43]. Marc J. Madou, 'Fundamentals of Microfabrication The Science of Miniaturization' 2 ed., CRC Press LLC, 2002

[44]. M. Elwenspoek, H. Jansen, 'Silicon Micromachining', Cambridge University Press, 1998.

[45]. Henri Jansen, Meint de Boer, Rob Legtenberg, Miko Elwenspoek, 'The black silicon method: a universal method for determining the parameter setting of a

fluorine-based reactive ion etcher in deep silicon trench etching with profile control', J. Micromech. Microeng., Jun. 2005, Vol. 5, Issue 2, pp.115-120.

[46]. Riccardo d'Agostino, Daniel L. Flamm, 'Plasma etching of Si and SiO2 in SF6–O2 mixtures', J. Appl. Phys., Jan. 1981, Vol. 52, Issue 1, pp. 162-167.

[47]. Yeong-Jyh Lii, Jacob Jorné, Kenneth C. Cadien, and Joseph E. Schoenholtz Jr., 'Plasma Etching of Silicon in SF6 Experimental and Reactor Modeling Studies', J. Electrochem. Soc., 1990, Vol. 137, pp. 3633.

[48]. Rob Legtenberg, Henri Jansen, Meint de Boer, and Miko Elwenspoe, 'Anisotrapic Reactive Ion Etching of Silicon Using SF6/O2/CHF3 Gas Mixtures', J. Electrochem. Soc., June 1995, Vol. 142, No. 6, pp. 2020-2028.

[49]. Gottlieb S. Oehrlein, Steve W. Robey, and J. Lennart Lindström, 'Surface processes in CF4/O2 reactive etching of silicon', Appl. Phys. Lett., Apr. 1988, Vol. 52, Issue 14, pp. 1170-1172.

[50]. P. M. Kopalidis and J. Jorné, 'Modeling and Experimental Studies of a Reactive Ion Etcher Using SF6/02 Chemistry', J. Electrochem. Soc., Oct. 1993 Vol. 140, No. 10, pp. 3037-3045.

[51]. Henri Jansen, Meint de Boer, Johannes Burger, Rob Legtenberg, and Miko Elwenspoek, 'The blacksiliconmethod II:The effect of maskmaterial and loading on the reactiveionetching of deepsilicontrenches', Microelectronic Engineering, Feb. 1995, Vol. 27, Issue 1-4, pp. 475-480.

[52]. Peter J. Gilgunn and Gary K. Fedder, 'Mechanisms of Process-Induced Heating of MEMS Structures During Plasma Release Etch', 2010 IEEE 23rd International Conference on Micro Electro Mechanical Systems, 24-28 Jan. 2010, pp. 320-323.

[53]. Hongwei Qu and Huikai Xie, 'Process Development for CMOS-MEMS Sensors With Robust Electrically Isolated Bulk Silicon Microstructures', Journal of Microelectromechanical Systems, October 2007, Vol. 16, No. 5, pp. 1152-1161.

[54]. Chao Gong, Shanhong Xia, Kai Deng, Qiang Bai, Shaofeng Chen, 'Design and Simulation of Miniature Vibrating Electric Field Sensors', Proceedings of IEEE Sensors, 24-27 Oct. 2004, Vol. 3, pp.1589-1592.

[55]. COMSOL Multiphysics 4.2, COMSOL, inc., 1998 - 2011.

[56]. Jim Carter, Allen Cowen, Busbee Hardy, Ramaswamy Mahadevan, Mark Stonefield, Steve Wilcenski, 'PolyMUMPs Design Handbook', Copyright © 1992-2005 by MEMSCAP.

[57]. 'General user manual: PhotoMap 3D / Microsurf 3D / ZoomSurf 3D / CyberSurf 3D Optical profiler', Fogale Nanotech., 2005.

Appendix A: Code of COMSOL with MATLAB Interface

1. Main

```
%------------------------- Param generation --------------------------

slit_wid_b= (2:0.1:9);
elec_wid_b= (2:0.1:8);
sht_thick_b= (1:0.1:10);
gap_b= (0.5:0.1:10);
gr_wid_b= (10:10:100);
iso_b = [0,0.6,0.8]
slits_num= 15 ;

obj=[];
step=1;

sn=slits_num;

for i=1:length(slit_wid_b)
    sw=slit_wid_b(i);
    for j=1:length(elec_wid_b)
        ew=elec_wid_b(j);
        for k=1:length(sht_thick_b)
            st=sht_thick_b(k);
                    for l=1:length(gap_b)
                g=gap_b(l);
                        for m=1:length(iso_b)
                                            iso=iso_b(m)
                    for m=1:length(gr_wid_b)
                        gr=gr_wid_b(m);
                                                    obj(step,1:7)=[sw,st,ew,g,iso,gr,sn];
                                        step=step+1;
                                        end
                end
            end
        end
    end
end

% ---------------------- loop of simulation -------------------------

simu_loop(obj);
simu_loop_fs(obj);
```

2. simu_loop

```
function simu_loop(obj)
import com.comsol.model.*
import com.comsol.model.util.*

for i=1:length(obj)
        model = ModelUtil.create('Model');

        model.modelPath('C:\Users\umzhou73\Desktop\matlab');

        model.modelNode.create('mod1');

        std=model.study.create('std1');
```

```
        sol=model.sol.create('sol1');
        g=model.geom.create('geom1', 2);

        es=model.physics.create('es', 'Electrostatics', 'geom1');


        model.study('std1').feature.create('stat', 'Stationary');

        model.geom('geom1').lengthUnit([native2unicode(hex2dec('00b5'),'Cp1252') 'm']);

    model.geom('geom1').scaleUnitValue(true);

%---------------------- parameter settings --------------------------

slit_wid = obj(i,1);                          % width of slits
sht_thick = obj(i,2);                         % shutter thickness
elec_wid = obj(i,3);                          % width of electrodes
gr_wid = obj(i,6);                            % width of guard ring
gap = obj(i,4);                               % gap
bn = obj(i,7)-1;                              % number of shutter blocks
iso = obj(i,5);

elec_thick = 0.5;                             % electrodes thickness
block_px_1=-30-bn*10;                         % start position of block array 1
block_px_2= 30+slit_wid;                      % start position of block array 2
elec_px_1 = block_px_1-slit_wid/2-elec_wid/2;      % start position of electro expose
elec_px_2 = 25+slit_wid/2-elec_wid/2;              % start position of electro shielded
gr_px_1 = -160-(bn+1)*10;                     % position of guard ring 1
gr_px_2 = 30+(bn+1)*10+30;                    % position of guard ring 2
isotropic = sht_thick*iso;                    % isotropic width

model.param.set('bn',bn);                     % set block number as a param
model.param.set('sn',bn+1);                   % set slits number as a param

%------------------------ generate geom -------------------------------

r1=g.feature.create('air_1', 'Rectangle');
r1.set('size', [640, 100]);
r1.set('base', 'center');

p1=g.feature.create('sht_2', 'Polygon');              % center block
p1.set('x', [-30+isotropic, -30, 30, 30-isotropic]);
p1.set('y', [sht_thick,0,0,sht_thick]);

p2=g.feature.create('p2', 'Polygon');                 % block 1
p2.set('x', [block_px_1+isotropic, block_px_1, block_px_1+10-slit_wid, block_px_1+10-slit_wid-isotropic] );
p2.set('y', [sht_thick, 0,0,sht_thick]);

arr1=g.feature.create('sht_arr1', 'Array');           % block array 1
arr1.selection('input').set({'p2'});
arr1.setIndex('fullsize', 'bn', 0);
arr1.setIndex('displ', '10', 0);

p3=g.feature.create('sht_1', 'Polygon');              % left block
p3.set('x', [gr_px_1+90+isotropic, gr_px_1+90, block_px_1-slit_wid, block_px_1-slit_wid-isotropic]);
p3.set('y', [sht_thick, 0,0,sht_thick]);

p4=g.feature.create('p4', 'Polygon');                 % block 2
p4.set('x', [block_px_2+isotropic, block_px_2, block_px_2+10-slit_wid, block_px_2+10-slit_wid-isotropic]);
p4.set('y', [sht_thick,0,0,sht_thick]);

arr2=g.feature.create('sht_arr2', 'Array');           % block arry2
```

```
arr2.selection('input').set({'p4'});
arr2.setIndex('fullsize', 'bn', 0);
arr2.setIndex('displ', '10', 0);

p5=g.feature.create('sht_3', 'Polygon');                  % right block
p5.set('x', [30+bn*10+slit_wid+isotropic, 30+bn*10+slit_wid, gr_px_2+10, gr_px_2+10-isotropic]);
p5.set('y', [sht_thick,0,0,sht_thick]);

r7=g.feature.create('elec_e', 'Rectangle');
r7.set('size', [elec_wid, elec_thick]);
r7.set('pos', [elec_px_1, -gap-elec_thick]);

arr3=g.feature.create('elec_e_arr','Array');          % exposed electrodes
arr3.selection('input').set({'elec_e'});
arr3.setIndex('fullsize','sn', 0);
arr3.setIndex('displ','10', 0);

r8=g.feature.create('elec_s', 'Rectangle');
r8.set('size', [elec_wid, elec_thick]);
r8.set('pos', [elec_px_2, -gap-elec_thick]);

arr4=g.feature.create('elec_s_arr','Array');          % shielded electrodes
arr4.selection('input').set({'elec_s'});
arr4.setIndex('fullsize','sn', 0);
arr4.setIndex('displ','10', 0);

r9=g.feature.create('gr_1', 'Rectangle');             % gr1
r9.set('size', [gr_wid , 2*elec_thick]);
r9.set('pos', [gr_px_1,-gap-elec_thick]);

r10=g.feature.create('gr_2', 'Rectangle');            % gr2
r10.set('size', [gr_wid, 2*elec_thick]);
r10.set('pos', [gr_px_2,-gap-elec_thick]);

r10=g.feature.create('substrate', 'Rectangle');       % substrate
r10.set('size', [330+(bn+1)*20, 20]);
r10.set('pos', [gr_px_1-5, -gap-elec_thick-20]);

r12=g.feature.create('air_2','Rectangle');            % artificial air
r12.setIndex('size','640', 0);
r12.setIndex('size','100', 1);
r12.set('pos',[-320,50]);

r13=g.feature.create('r13','Rectangle');              % dense meshing area
r13.set('size', [330+(bn+1)*20 , gap+elec_thick+sht_thick]);
r13.set('pos', [gr_px_1-5 , -gap-elec_thick]);

copy1=g.feature.create('copy1', 'Copy');
copy1.selection('input').set({'sht_1','sht_2','sht_3','sht_arr1','sht_arr2', 'elec_e_arr','elec_s_arr','gr_1','gr_2'});

dif3=g.feature.create('air_3', 'Difference');         % air_shutter_electrodes
dif3.selection('input').set('r13');
dif3.selection('input2').set('copy1');


model.geom('geom1').run;



%--------------- geom analysis and selection settings --------------------

[domains boundaries boundariescrd interiorBoundaries] = geomAnalyze(model.geom('geom1'));
```

```
% boundary selection
sht_boundaries = [];
sht_top_boundaries = [];
elec_e_boundaries=[];
elec_s_boundaries=[];
gr_boundaries=[];
air_boundaries = [];
source_boundaries = [];
sub_boundaries = [];
grounding_boundaries=[];
si_domains = [];
pyrex_domains = [];
air_domains = [];
air_a_domains = [];
gold_domains = [];
air_3_domains = [];
air_1_domains = [];

sht_boundaries = [findStrc('sht_1',boundaries,1) findStrc('sht_2',boundaries,1) findStrc('sht_3',boundaries,1)
findStrc('sht_arr1',boundaries,1) findStrc('sht_arr2',boundaries,1)];

k=1;
for j=1:length(sht_boundaries)
   if single(boundariescrd(sht_boundaries(j),2)) == single(sht_thick) && single(boundariescrd(sht_boundaries(j),4)) ==
single(sht_thick);
      sht_top_boundaries(k)=sht_boundaries(j);
      k=k+1;
   end
end

elec_e_boundaries=[findStrc('elec_e',boundaries,1)];

elec_s_boundaries=[findStrc('elec_s',boundaries,1)];

gr_boundaries=[findStrc('gr_1',boundaries,1) findStrc('gr_2',boundaries,1)];

air_boundaries = [findStrc('air_1',boundaries,1) findStrc('air_2',boundaries,1)];


k=1;
for j=1:length(air_boundaries)
   if boundariescrd(air_boundaries(j),2) == 150 && boundariescrd(air_boundaries(j),4) == 150;
      source_boundaries(k)=air_boundaries(j);
      k=k+1;
   end
end


sub_boundaries = [findStrc('substrate',boundaries,1) findStrc('air_1',boundaries,1)];
k=1;
for j=1:length(sub_boundaries)
   if (single(boundariescrd(sub_boundaries(j),2)) == single(-gap-elec_thick-20) &&
single(boundariescrd(sub_boundaries(j),4)) == single(-gap-elec_thick-20)) ||
(single(boundariescrd(sub_boundaries(j),2) == -50 && single(boundariescrd(sub_boundaries(j),4)) == -50));
      grounding_boundaries(k)=sub_boundaries(j);
      k=k+1;
   end
end

% domains selection
```

```
si_domains = [findStr('sht', domains)];
pyrex_domains = [findStr('substrate', domains)];
air_domains = [findStr('air_1', domains) findStr('air_3', domains)];
air_a_domains = [findStr('air_2', domains)];
gold_domains = [findStr('elec_e', domains) findStr('elec_s', domains) findStr('gr_1', domains) findStr('gr_2', domains)];
air_3_domains = [findStr('air_3', domains)];
air_1_domains = [findStr('air_1', domains)];


%-------------------  material settings-----------------------

model.material.create('mat1');
model.material('mat1').name('Air');
model.material('mat1').materialModel('def').set('relpermeability', '1');
model.material('mat1').materialModel('def').set('relpermittivity', '1');
model.material('mat1').materialModel('def').set('dynamicviscosity', 'eta(T[1/K])[Pa*s]');
model.material('mat1').materialModel('def').set('ratioofspecificheat', '1.4');
model.material('mat1').materialModel('def').set('electricconductivity', '0[S/m]');
model.material('mat1').materialModel('def').set('heatcapacity', 'Cp(T[1/K])[J/(kg*K)]');
model.material('mat1').materialModel('def').set('density', 'rho(pA[1/Pa],T[1/K])[kg/m^3]');
model.material('mat1').materialModel('def').set('thermalconductivity', 'k(T[1/K])[W/(m*K)]');
model.material('mat1').materialModel('def').set('soundspeed', 'cs(T[1/K])[m/s]');
model.material('mat1').materialModel('def').func.create('eta', 'Piecewise');
model.material('mat1').materialModel('def').func('eta').set('funcname', 'eta');
model.material('mat1').materialModel('def').func('eta').set('arg', 'T');
model.material('mat1').materialModel('def').func('eta').set('extrap', 'constant');
model.material('mat1').materialModel('def').func('eta').set('pieces', {'200.0' '1600.0' '-8.38278E-7+8.35717342E-8*T^1-
7.69429583E-11*T^2+4.6437266E-14*T^3-1.06585607E-17*T^4'});
model.material('mat1').materialModel('def').func.create('Cp', 'Piecewise');
model.material('mat1').materialModel('def').func('Cp').set('funcname', 'Cp');
model.material('mat1').materialModel('def').func('Cp').set('arg', 'T');
model.material('mat1').materialModel('def').func('Cp').set('extrap', 'constant');
model.material('mat1').materialModel('def').func('Cp').set('pieces', {'200.0' '1600.0' '1047.63657-
0.372589265*T^1+9.45304214E-4*T^2-6.02409443E-7*T^3+1.2858961E-10*T^4'});
model.material('mat1').materialModel('def').func.create('rho', 'Analytic');
model.material('mat1').materialModel('def').func('rho').set('funcname', 'rho');
model.material('mat1').materialModel('def').func('rho').set('args', {'pA' 'T'});
model.material('mat1').materialModel('def').func('rho').set('expr', 'pA*0.02897/8.314/T');
model.material('mat1').materialModel('def').func('rho').set('dermethod', 'manual');
model.material('mat1').materialModel('def').func('rho').set('argders', {'pA' 'd(pA*0.02897/8.314/T,pA)'; 'T'
'd(pA*0.02897/8.314/T,T)'});
model.material('mat1').materialModel('def').func.create('k', 'Piecewise');
model.material('mat1').materialModel('def').func('k').set('funcname', 'k');
model.material('mat1').materialModel('def').func('k').set('arg', 'T');
model.material('mat1').materialModel('def').func('k').set('extrap', 'constant');
model.material('mat1').materialModel('def').func('k').set('pieces', {'200.0' '1600.0' '-0.00227583562+1.15480022E-
4*T^1-7.90252856E-8*T^2+4.11702505E-11*T^3-7.43864331E-15*T^4'});
model.material('mat1').materialModel('def').func.create('cs', 'Analytic');
model.material('mat1').materialModel('def').func('cs').set('funcname', 'cs');
model.material('mat1').materialModel('def').func('cs').set('args', {'T'});
model.material('mat1').materialModel('def').func('cs').set('expr', 'sqrt(1.4*287*T)');
model.material('mat1').materialModel('def').func('cs').set('dermethod', 'manual');
model.material('mat1').materialModel('def').func('cs').set('argders', {'T' 'd(sqrt(1.4*287*T),T)'});
model.material('mat1').materialModel('def').addInput('temperature');
model.material('mat1').materialModel('def').addInput('pressure');
model.material('mat1').selection.set(air_domains);

model.material.create('mat2');
model.material('mat2').name('Au');
model.material('mat2').materialModel('def').set('electricconductivity', '45.6e6[S/m]');
model.material('mat2').materialModel('def').set('thermalexpansioncoefficient', '14.2e-6[1/K]');
model.material('mat2').materialModel('def').set('heatcapacity', '129[J/(kg*K)]');
```

```
model.material('mat2').materialModel('def').set('density', '19300[kg/m^3]');
model.material('mat2').materialModel('def').set('thermalconductivity', '317[W/(m*K)]');
model.material('mat2').materialModel.create('Enu', 'Young''s modulus and Poisson''s ratio');
model.material('mat2').materialModel('Enu').set('poissonsratio', '0.44');
model.material('mat2').materialModel('Enu').set('youngsmodulus', '70e9[Pa]');
model.material('mat2').materialModel('def').set('relpermittivity', {'6.7'});
model.material('mat2').selection.set(gold_domains);

model.material.create('mat3');
model.material('mat3').name('Au (2)');
model.material('mat3').materialModel('def').set('electricconductivity', '45.6e6[S/m]');
model.material('mat3').materialModel('def').set('thermalexpansioncoefficient', '14.2e-6[1/K]');
model.material('mat3').materialModel('def').set('heatcapacity', '129[J/(kg*K)]');
model.material('mat3').materialModel('def').set('density', '19300[kg/m^3]');
model.material('mat3').materialModel('def').set('thermalconductivity', '317[W/(m*K)]');
model.material('mat3').materialModel.create('Enu', 'Young''s modulus and Poisson''s ratio');
model.material('mat3').materialModel('Enu').set('poissonsratio', '0.44');
model.material('mat3').materialModel('Enu').set('youngsmodulus', '70e9[Pa]');
model.material('mat3').selection.geom('geom1',1);
model.material('mat3').selection.set(sht_top_boundaries);

model.material.create('mat4');
model.material('mat4').name('Silicon (single-crystal)');
model.material('mat4').materialModel('def').set('density', '2330[kg/m^3]');
model.material('mat4').materialModel.create('Anisotropic', 'Anisotropic');
model.material('mat4').materialModel('Anisotropic').set('D', {'166[GPa]' '64[GPa]' '166[GPa]' '64[GPa]' '64[GPa]'
'166[GPa]' '0[GPa]' '0[GPa]' '0[GPa]' '80[GPa]' '0[GPa]' '0[GPa]' '0[GPa]' '0[GPa]' '80[GPa]' '0[GPa]' '0[GPa]' '0[GPa]'
'0[GPa]' '0[GPa]' '80[GPa]'});
model.material('mat4').materialModel('def').set('relpermittivity', {'11.67'});
model.material('mat4').selection.set(si_domains);

model.material.create('mat5');
model.material('mat5').name('Pyrex');
model.material('mat5').materialModel('def').set('relpermittivity', {'4.7'});
model.material('mat5').materialModel('def').set('electricconductivity', {'1.25e-13'});
model.material('mat5').selection.set(pyrex_domains);

model.material.create('mat6');
model.material('mat6').name('Air (2)');
model.material('mat6').materialModel('def').set('relpermeability', '1');
model.material('mat6').materialModel('def').set('relpermittivity', '1');
model.material('mat6').materialModel('def').set('dynamicviscosity', 'eta(T[1/K])[Pa*s]');
model.material('mat6').materialModel('def').set('ratioofspecificheat', '1.4');
model.material('mat6').materialModel('def').set('electricconductivity', '0[S/m]');
model.material('mat6').materialModel('def').set('heatcapacity', 'Cp(T[1/K])[J/(kg*K)]');
model.material('mat6').materialModel('def').set('density', 'rho(pA[1/Pa],T[1/K])[kg/m^3]');
model.material('mat6').materialModel('def').set('thermalconductivity', 'k(T[1/K])[W/(m*K)]');
model.material('mat6').materialModel('def').set('soundspeed', 'cs(T[1/K])[m/s]');
model.material('mat6').materialModel('def').func.create('eta', 'Piecewise');
model.material('mat6').materialModel('def').func('eta').set('funcname', 'eta');
model.material('mat6').materialModel('def').func('eta').set('arg', 'T');
model.material('mat6').materialModel('def').func('eta').set('extrap', 'constant');
model.material('mat6').materialModel('def').func('eta').set('pieces', {'200.0' '1600.0' '-8.38278E-7+8.35717342E-8*T^1-
7.69429583E-11*T^2+4.6437266E-14*T^3-1.06585607E-17*T^4'});
model.material('mat6').materialModel('def').func.create('Cp', 'Piecewise');
model.material('mat6').materialModel('def').func('Cp').set('funcname', 'Cp');
model.material('mat6').materialModel('def').func('Cp').set('arg', 'T');
model.material('mat6').materialModel('def').func('Cp').set('extrap', 'constant');
model.material('mat6').materialModel('def').func('Cp').set('pieces', {'200.0' '1600.0' '1047.63657-
0.372589265*T^1+9.45304214E-4*T^2-6.02409443E-7*T^3+1.2858961E-10*T^4'});
model.material('mat6').materialModel('def').func.create('rho', 'Analytic');
model.material('mat6').materialModel('def').func('rho').set('funcname', 'rho');
```

```
model.material('mat6').materialModel('def').func('rho').set('args', {'pA' 'T'});
model.material('mat6').materialModel('def').func('rho').set('expr', 'pA*0.02897/8.314/T');
model.material('mat6').materialModel('def').func('rho').set('dermethod', 'manual');
model.material('mat6').materialModel('def').func('rho').set('argders', {'pA' 'd(pA*0.02897/8.314/T,pA)'; 'T'
'd(pA*0.02897/8.314/T,T)'});
model.material('mat6').materialModel('def').func.create('k', 'Piecewise');
model.material('mat6').materialModel('def').func('k').set('funcname', 'k');
model.material('mat6').materialModel('def').func('k').set('arg', 'T');
model.material('mat6').materialModel('def').func('k').set('extrap', 'constant');
model.material('mat6').materialModel('def').func('k').set('pieces', {'200.0' '1600.0' '-0.00227583562+1.15480022E-
4*T^1-7.90252856E-8*T^2+4.11702505E-11*T^3-7.43864331E-15*T^4'});
model.material('mat6').materialModel('def').func.create('cs', 'Analytic');
model.material('mat6').materialModel('def').func('cs').set('funcname', 'cs');
model.material('mat6').materialModel('def').func('cs').set('args', {'T'});
model.material('mat6').materialModel('def').func('cs').set('expr', 'sqrt(1.4*287*T)');
model.material('mat6').materialModel('def').func('cs').set('dermethod', 'manual');
model.material('mat6').materialModel('def').func('cs').set('argders', {'T' 'd(sqrt(1.4*287*T),T)'});
model.material('mat6').materialModel('def').addInput('temperature');
model.material('mat6').materialModel('def').addInput('pressure');
model.material('mat6').materialModel('def').set('relpermittivity', {'1e-5'});
model.material('mat6').selection.set(air_a_domains);


%------------------- physics settings ----------------------------------

model.physics('es').feature.create('pot1', 'ElectricPotential', 1);
model.physics('es').feature('pot1').set('V0', 1, '1');
model.physics('es').feature('pot1').selection.set(source_boundaries);

model.physics('es').feature.create('gnd1', 'Ground', 1);
model.physics('es').feature('gnd1').selection.set(grounding_boundaries);

model.physics('es').feature.create('gnd2', 'Ground', 1);
model.physics('es').feature('gnd2').selection.set(gr_boundaries);

model.physics('es').feature.create('gnd3', 'Ground', 1);
model.physics('es').feature('gnd3').selection.set(elec_e_boundaries);

model.physics('es').feature.create('gnd4', 'Ground', 1);
model.physics('es').feature('gnd4').selection.set(elec_s_boundaries);

model.physics('es').feature.create('gnd5', 'Ground', 1);
model.physics('es').feature('gnd5').selection.set(sht_top_boundaries);


%----------------- meshing settings ------------------------------------

mesh1=model.mesh.create('mesh1', 'geom1');

model.mesh('mesh1').feature.create('ftri1', 'FreeTri');
model.mesh('mesh1').feature('ftri1').selection.geom('geom1', 2);
model.mesh('mesh1').feature('ftri1').selection.set(air_3_domains);
model.mesh('mesh1').feature('ftri1').feature.create('size1', 'Size');
model.mesh('mesh1').feature('ftri1').feature('size1').set('custom', 'on');
model.mesh('mesh1').feature('ftri1').feature('size1').set('hmaxactive', 'on');
model.mesh('mesh1').feature('ftri1').feature('size1').set('hmax', '1');
model.mesh('mesh1').feature('ftri1').feature('size1').set('hminactive', 'on');
model.mesh('mesh1').feature('ftri1').feature('size1').set('hmin', '0.1');
model.mesh('mesh1').feature('ftri1').feature('size1').set('hgradactive', 'on');
model.mesh('mesh1').feature('ftri1').feature('size1').set('hgrad', '1.3');

model.mesh('mesh1').feature.create('ftri2', 'FreeTri');
```

```
model.mesh('mesh1').feature('ftri2').selection.geom('geom1', 2);
model.mesh('mesh1').feature('ftri2').selection.set([gold_domains si_domains]);
model.mesh('mesh1').feature('ftri2').feature.create('size1', 'Size');
model.mesh('mesh1').feature('ftri2').feature('size1').set('custom', 'on');
model.mesh('mesh1').feature('ftri2').feature('size1').set('hmaxactive', 'on');
model.mesh('mesh1').feature('ftri2').feature('size1').set('hmax', '1');
model.mesh('mesh1').feature('ftri2').feature('size1').set('hminactive', 'on');
model.mesh('mesh1').feature('ftri2').feature('size1').set('hmin', '0.1');
model.mesh('mesh1').feature('ftri2').feature('size1').set('hgradactive', 'on');
model.mesh('mesh1').feature('ftri2').feature('size1').set('hgrad', '1.3');

model.mesh('mesh1').feature.create('ftri3', 'FreeTri');
model.mesh('mesh1').feature('ftri3').selection.geom('geom1', 2);
model.mesh('mesh1').feature('ftri3').selection.set([air_1_domains pyrex_domains]);
model.mesh('mesh1').feature('ftri3').feature.create('size1', 'Size');
model.mesh('mesh1').feature('ftri3').feature('size1').set('custom', 'on');
model.mesh('mesh1').feature('ftri3').feature('size1').set('hmaxactive', 'on');
model.mesh('mesh1').feature('ftri3').feature('size1').set('hmax', '5');
model.mesh('mesh1').feature('ftri3').feature('size1').set('hminactive', 'on');
model.mesh('mesh1').feature('ftri3').feature('size1').set('hmin', '0.5');
model.mesh('mesh1').feature('ftri3').feature('size1').set('hgradactive', 'on');
model.mesh('mesh1').feature('ftri3').feature('size1').set('hgrad', '2');

model.mesh('mesh1').feature.create('ref1', 'Refine');
model.mesh('mesh1').feature('ref1').set('boxcoord', 'on');
model.mesh('mesh1').feature('ref1').set('xmin', '-595');
model.mesh('mesh1').feature('ref1').set('xmax', '595');
model.mesh('mesh1').feature('ref1').set('ymin' , -gap-elec_thick-5);
model.mesh('mesh1').feature('ref1').set('ymax', sht_thick+10);
model.mesh('mesh1').feature('ref1').set('numrefine', '3');

model.mesh('mesh1').feature.create('ftri4', 'FreeTri');
model.mesh('mesh1').feature('ftri4').selection.geom('geom1', 2);
model.mesh('mesh1').feature('ftri4').selection.set(air_a_domains);
model.mesh('mesh1').feature('ftri4').feature.create('size1', 'Size');
model.mesh('mesh1').feature('ftri4').feature('size1').set('hauto', '3');

model.mesh('mesh1').run;


%-------------------- study settings ----------------------------------

model.sol('sol1').study('std1');
model.sol('sol1').feature.create('st1', 'StudyStep');
model.sol('sol1').feature('st1').set('study', 'std1');
model.sol('sol1').feature('st1').set('studystep', 'stat');
model.sol('sol1').feature.create('v1', 'Variables');
model.sol('sol1').feature.create('s1', 'Stationary');
model.sol('sol1').feature('s1').feature.create('fc1', 'FullyCoupled');
model.sol('sol1').feature('s1').feature.remove('fcDef');
model.sol('sol1').attach('std1');
model.sol('sol1').runAll;

%------------------------- save data ------------------------------------

[IC1 unit]=mphint(model,'es.nD','edim',1,'selection', [elec_e_boundaries]);
[IC2 unit]=mphint(model,'es.nD','edim',1,'selection', [elec_s_boundaries]);
IC_d=(IC1-IC2)*1e20;

D(i,1:10)=[slit_wid, sht_thick, elec_wid, gr_wid, gap, bn, iso, IC1*1e20, IC2*1e20, IC_d];

save sim2d_march_2012 D;
```

```
%-------------------- clear structure ----------------------------------

    model.param.remove('bn');
    model.param.remove('sn');
    model.mesh.remove('mesh1');
    sol.feature.remove('st1');
    sol.feature.remove('v1');
    sol.feature.remove('s1');
    model.geom.remove('geom1');
    model.physics.remove('es');
    std.feature.remove('stat');
    IC1=0;
    IC2=0;
    IC_d=0;
    step=i;
    clear model;

end
```

3. simu_loop_fs

```
function simu_loop_fs(obj)
import com.comsol.model.*
import com.comsol.model.util.*

for i=1:length(obj)
        model = ModelUtil.create('Model');

        model.modelPath('C:\Users\umzhou73\Desktop\matlab');

        model.modelNode.create('mod1');

        std=model.study.create('std1');
        sol=model.sol.create('sol1');
        g=model.geom.create('geom1', 2);

        es=model.physics.create('es', 'Electrostatics', 'geom1');


        model.study('std1').feature.create('stat', 'Stationary');

        model.geom('geom1').lengthUnit([native2unicode(hex2dec('00b5'),'Cp1252') 'm']);

    model.geom('geom1').scaleUnitValue(true);

%---------------------- parameter settings --------------------------

slit_wid = obj(i,1);                          % width of slits
sht_thick = obj(i,2);                         % shutter thickness
elec_wid = obj(i,3);                          % width of electrodes
gr_wid = obj(i,6);                            % width of guard ring
gap = obj(i,4);                               % gap
bn = obj(i,7)-1;                              % number of shutter blocks
iso = obj(i,5);

elec_thick = 0.5;                             % electrodes thickness
block_px_1=-30-bn*10;                         % start position of block array 1
block_px_2= 30+slit_wid;                      % start position of block array 2
elec_px_1 = block_px_1-slit_wid/2-elec_wid/2;       % start position of electro expose
elec_px_2 = 25+slit_wid/2-elec_wid/2;               % start position of electro shielded
gr_px_1 = -160-(bn+1)*10;                     % position of guard ring 1
gr_px_2 = 30+(bn+1)*10+30;                    % position of guard ring 2
```

```
isotropic = sht_thick*iso;                          % isotropic width

model.param.set('bn',bn);                           % set block number as a param
model.param.set('sn',bn+1);                          % set slits number as a param

%------------------------ generate geom -------------------------------

r1=g.feature.create('air_1', 'Rectangle');
r1.set('size', [640, 100]);
r1.set('base', 'center');

p1=g.feature.create('sht_2', 'Polygon');                  % center block
p1.set('x', [-30+isotropic, -30, 30, 30-isotropic]);
p1.set('y', [sht_thick,0,0,sht_thick]);

p2=g.feature.create('p2', 'Polygon');                    % block 1
p2.set('x', [block_px_1+isotropic, block_px_1, block_px_1+10-slit_wid, block_px_1+10-slit_wid-isotropic] );
p2.set('y', [sht_thick, 0,0,sht_thick]);

arr1=g.feature.create('sht_arr1', 'Array');              % block array 1
arr1.selection('input').set({'p2'});
arr1.setIndex('fullsize', 'bn', 0);
arr1.setIndex('displ', '10', 0);

p3=g.feature.create('sht_1', 'Polygon');                 % left block
p3.set('x', [gr_px_1+90+isotropic, gr_px_1+90, block_px_1-slit_wid, block_px_1-slit_wid-isotropic]);
p3.set('y', [sht_thick, 0,0,sht_thick]);

p4=g.feature.create('p4', 'Polygon');                    % block 2
p4.set('x', [block_px_2+isotropic, block_px_2, block_px_2+10-slit_wid, block_px_2+10-slit_wid-isotropic]);
p4.set('y', [sht_thick,0,0,sht_thick]);

arr2=g.feature.create('sht_arr2', 'Array');              % block arry2
arr2.selection('input').set({'p4'});
arr2.setIndex('fullsize', 'bn', 0);
arr2.setIndex('displ', '10', 0);

p5=g.feature.create('sht_3', 'Polygon');                 % right block
p5.set('x', [30+bn*10+slit_wid+isotropic, 30+bn*10+slit_wid, gr_px_2+10, gr_px_2+10-isotropic]);
p5.set('y', [sht_thick,0,0,sht_thick]);

r7=g.feature.create('elec_e', 'Rectangle');
r7.set('size', [elec_wid, elec_thick]);
r7.set('pos', [elec_px_1, -gap-elec_thick]);

arr3=g.feature.create('elec_e_arr','Array');           % exposed electrodes
arr3.selection('input').set({'elec_e'});
arr3.setIndex('fullsize','sn', 0);
arr3.setIndex('displ','10', 0);

r8=g.feature.create('elec_s', 'Rectangle');
r8.set('size', [elec_wid, elec_thick]);
r8.set('pos', [elec_px_2, -gap-elec_thick]);

arr4=g.feature.create('elec_s_arr','Array');           % shielded electrodes
arr4.selection('input').set({'elec_s'});
arr4.setIndex('fullsize','sn', 0);
arr4.setIndex('displ','10', 0);

r9=g.feature.create('gr_1', 'Rectangle');             % gr1
r9.set('size', [gr_wid , 2*elec_thick]);
r9.set('pos', [gr_px_1,-gap-elec_thick]);
```

```
r10=g.feature.create('gr_2', 'Rectangle');              % gr2
r10.set('size', [gr_wid, 2*elec_thick]);
r10.set('pos', [gr_px_2,-gap-elec_thick]);

r10=g.feature.create('substrate', 'Rectangle');        % substrate
r10.set('size', [330+(bn+1)*20, 20]);
r10.set('pos', [gr_px_1-5, -gap-elec_thick-20]);

r12=g.feature.create('air_2','Rectangle');             % artificial air
r12.setIndex('size','640', 0);
r12.setIndex('size','100', 1);
r12.set('pos',[-320,50]);

r13=g.feature.create('r13','Rectangle');               % dense meshing area
r13.set('size', [330+(bn+1)*20 , gap+elec_thick+sht_thick]);
r13.set('pos', [gr_px_1-5 , -gap-elec_thick]);

copy1=g.feature.create('copy1', 'Copy');
copy1.selection('input').set({'sht_1','sht_2','sht_3','sht_arr1','sht_arr2', 'elec_e_arr','elec_s_arr','gr_1','gr_2'});

dif3=g.feature.create('air_3', 'Difference');          % air_shutter_electrodes
dif3.selection('input').set('r13');
dif3.selection('input2').set('copy1');


model.geom('geom1').run;



%--------------- geom analysis and selection settings --------------------

[domains boundaries boundariescrd interiorBoundaries] = geomAnalyze(model.geom('geom1'));

% boundary selection
sht_boundaries = [];
sht_top_boundaries = [];
elec_e_boundaries=[];
elec_s_boundaries=[];
gr_boundaries=[];
air_boundaries = [];
source_boundaries = [];
sub_boundaries = [];
grounding_boundaries=[];
si_domains = [];
pyrex_domains = [];
air_domains = [];
air_a_domains = [];
gold_domains = [];
air_3_domains = [];
air_1_domains = [];

sht_boundaries = [findStrc('sht_1',boundaries,1) findStrc('sht_2',boundaries,1) findStrc('sht_3',boundaries,1)
findStrc('sht_arr1',boundaries,1) findStrc('sht_arr2',boundaries,1)];

k=1;
for j=1:length(sht_boundaries)
  if single(boundariescrd(sht_boundaries(j),2)) == single(sht_thick) && single(boundariescrd(sht_boundaries(j),4)) ==
single(sht_thick);
     sht_top_boundaries(k)=sht_boundaries(j);
     k=k+1;
  end
```

```
end

elec_e_boundaries=[findStrc('elec_e',boundaries,1)];

elec_s_boundaries=[findStrc('elec_s',boundaries,1)];

gr_boundaries=[findStrc('gr_1',boundaries,1) findStrc('gr_2',boundaries,1)];

air_boundaries = [findStrc('air_1',boundaries,1) findStrc('air_2',boundaries,1)];


k=1;
for j=1:length(air_boundaries)
   if boundariescrd(air_boundaries(j),2) == 150 && boundariescrd(air_boundaries(j),4) == 150;
     source_boundaries(k)=air_boundaries(j);
     k=k+1;
   end
end


sub_boundaries = [findStrc('substrate',boundaries,1) findStrc('air_1',boundaries,1)];
k=1;
for j=1:length(sub_boundaries)
   if (single(boundariescrd(sub_boundaries(j),2)) == single(-gap-elec_thick-20) &&
single(boundariescrd(sub_boundaries(j),4)) == single(-gap-elec_thick-20)) ||
(single(boundariescrd(sub_boundaries(j),2) == -50 && single(boundariescrd(sub_boundaries(j),4)) == -50));
     grounding_boundaries(k)=sub_boundaries(j);
     k=k+1;
   end
end

% domains selection

si_domains = [findStr('sht', domains)];
pyrex_domains = [findStr('substrate', domains)];
air_domains = [findStr('air_1', domains) findStr('air_3', domains)];
air_a_domains = [findStr('air_2', domains)];
gold_domains = [findStr('elec_e', domains) findStr('elec_s', domains) findStr('gr_1', domains) findStr('gr_2', domains)];
air_3_domains = [findStr('air_3', domains)];
air_1_domains = [findStr('air_1', domains)];


%-------------------  material settings----------------------

model.material.create('mat1');
model.material('mat1').name('Air');
model.material('mat1').materialModel('def').set('relpermeability', '1');
model.material('mat1').materialModel('def').set('relpermittivity', '1');
model.material('mat1').materialModel('def').set('dynamicviscosity', 'eta(T[1/K])[Pa*s]');
model.material('mat1').materialModel('def').set('ratioofspecificheat', '1.4');
model.material('mat1').materialModel('def').set('electricconductivity', '0[S/m]');
model.material('mat1').materialModel('def').set('heatcapacity', 'Cp(T[1/K])[J/(kg*K)]');
model.material('mat1').materialModel('def').set('density', 'rho(pA[1/Pa],T[1/K])[kg/m^3]');
model.material('mat1').materialModel('def').set('thermalconductivity', 'k(T[1/K])[W/(m*K)]');
model.material('mat1').materialModel('def').set('soundspeed', 'cs(T[1/K])[m/s]');
model.material('mat1').materialModel('def').func.create('eta', 'Piecewise');
model.material('mat1').materialModel('def').func('eta').set('funcname', 'eta');
model.material('mat1').materialModel('def').func('eta').set('arg', 'T');
model.material('mat1').materialModel('def').func('eta').set('extrap', 'constant');
model.material('mat1').materialModel('def').func('eta').set('pieces', {'200.0' '1600.0' '-8.38278E-7+8.35717342E-8*T^1-
7.69429583E-11*T^2+4.6437266E-14*T^3-1.06585607E-17*T^4'});
model.material('mat1').materialModel('def').func.create('Cp', 'Piecewise');
```

```
model.material('mat1').materialModel('def').func('Cp').set('funcname', 'Cp');
model.material('mat1').materialModel('def').func('Cp').set('arg', 'T');
model.material('mat1').materialModel('def').func('Cp').set('extrap', 'constant');
model.material('mat1').materialModel('def').func('Cp').set('pieces', {'200.0' '1600.0' '1047.63657-
0.372589265*T^1+9.45304214E-4*T^2-6.02409443E-7*T^3+1.2858961E-10*T^4'});
model.material('mat1').materialModel('def').func.create('rho', 'Analytic');
model.material('mat1').materialModel('def').func('rho').set('funcname', 'rho');
model.material('mat1').materialModel('def').func('rho').set('args', {'pA' 'T'});
model.material('mat1').materialModel('def').func('rho').set('expr', 'pA*0.02897/8.314/T');
model.material('mat1').materialModel('def').func('rho').set('dermethod', 'manual');
model.material('mat1').materialModel('def').func('rho').set('argders', {'pA' 'd(pA*0.02897/8.314/T,pA)'; 'T'
'd(pA*0.02897/8.314/T,T)'});
model.material('mat1').materialModel('def').func.create('k', 'Piecewise');
model.material('mat1').materialModel('def').func('k').set('funcname', 'k');
model.material('mat1').materialModel('def').func('k').set('arg', 'T');
model.material('mat1').materialModel('def').func('k').set('extrap', 'constant');
model.material('mat1').materialModel('def').func('k').set('pieces', {'200.0' '1600.0' '-0.00227583562+1.15480022E-
4*T^1-7.90252856E-8*T^2+4.11702505E-11*T^3-7.43864331E-15*T^4'});
model.material('mat1').materialModel('def').func.create('cs', 'Analytic');
model.material('mat1').materialModel('def').func('cs').set('funcname', 'cs');
model.material('mat1').materialModel('def').func('cs').set('args', {'T'});
model.material('mat1').materialModel('def').func('cs').set('expr', 'sqrt(1.4*287*T)');
model.material('mat1').materialModel('def').func('cs').set('dermethod', 'manual');
model.material('mat1').materialModel('def').func('cs').set('argders', {'T' 'd(sqrt(1.4*287*T),T)'});
model.material('mat1').materialModel('def').addInput('temperature');
model.material('mat1').materialModel('def').addInput('pressure');
model.material('mat1').selection.set(air_domains);

model.material.create('mat2');
model.material('mat2').name('Au');
model.material('mat2').materialModel('def').set('electricconductivity', '45.6e6[S/m]');
model.material('mat2').materialModel('def').set('thermalexpansioncoefficient', '14.2e-6[1/K]');
model.material('mat2').materialModel('def').set('heatcapacity', '129[J/(kg*K)]');
model.material('mat2').materialModel('def').set('density', '19300[kg/m^3]');
model.material('mat2').materialModel('def').set('thermalconductivity', '317[W/(m*K)]');
model.material('mat2').materialModel.create('Enu', 'Young''s modulus and Poisson''s ratio');
model.material('mat2').materialModel('Enu').set('poissonsratio', '0.44');
model.material('mat2').materialModel('Enu').set('youngsmodulus', '70e9[Pa]');
model.material('mat2').materialModel('def').set('relpermittivity', {'6.7'});
model.material('mat2').selection.set(gold_domains);

model.material.create('mat3');
model.material('mat3').name('Au (2)');
model.material('mat3').materialModel('def').set('electricconductivity', '45.6e6[S/m]');
model.material('mat3').materialModel('def').set('thermalexpansioncoefficient', '14.2e-6[1/K]');
model.material('mat3').materialModel('def').set('heatcapacity', '129[J/(kg*K)]');
model.material('mat3').materialModel('def').set('density', '19300[kg/m^3]');
model.material('mat3').materialModel('def').set('thermalconductivity', '317[W/(m*K)]');
model.material('mat3').materialModel.create('Enu', 'Young''s modulus and Poisson''s ratio');
model.material('mat3').materialModel('Enu').set('poissonsratio', '0.44');
model.material('mat3').materialModel('Enu').set('youngsmodulus', '70e9[Pa]');
model.material('mat3').selection.geom('geom1',1);
model.material('mat3').selection.set(sht_top_boundaries);

model.material.create('mat4');
model.material('mat4').name('Silicon (single-crystal)');
model.material('mat4').materialModel('def').set('density', '2330[kg/m^3]');
model.material('mat4').materialModel.create('Anisotropic', 'Anisotropic');
model.material('mat4').materialModel('Anisotropic').set('D', {'166[GPa]' '64[GPa]' '166[GPa]' '64[GPa]' '64[GPa]'
'166[GPa]' '0[GPa]' '0[GPa]' '0[GPa]' '80[GPa]' '0[GPa]' '0[GPa]' '0[GPa]' '0[GPa]' '80[GPa]' '0[GPa]' '0[GPa]' '0[GPa]'
'0[GPa]' '0[GPa]' '80[GPa]'});
model.material('mat4').materialModel('def').set('relpermittivity', {'11.67'});
```

```
model.material('mat4').selection.set(si_domains);

model.material.create('mat5');
model.material('mat5').name('Pyrex');
model.material('mat5').materialModel('def').set('relpermittivity', {'4.7'});
model.material('mat5').materialModel('def').set('electricconductivity', {'1.25e-13'});
model.material('mat5').selection.set(pyrex_domains);

model.material.create('mat6');
model.material('mat6').name('Air (2)');
model.material('mat6').materialModel('def').set('relpermeability', '1');
model.material('mat6').materialModel('def').set('relpermittivity', '1');
model.material('mat6').materialModel('def').set('dynamicviscosity', 'eta(T[1/K])[Pa*s]');
model.material('mat6').materialModel('def').set('ratioofspecificheat', '1.4');
model.material('mat6').materialModel('def').set('electricconductivity', '0[S/m]');
model.material('mat6').materialModel('def').set('heatcapacity', 'Cp(T[1/K])[J/(kg*K)]');
model.material('mat6').materialModel('def').set('density', 'rho(pA[1/Pa],T[1/K])[kg/m^3]');
model.material('mat6').materialModel('def').set('thermalconductivity', 'k(T[1/K])[W/(m*K)]');
model.material('mat6').materialModel('def').set('soundspeed', 'cs(T[1/K])[m/s]');
model.material('mat6').materialModel('def').func.create('eta', 'Piecewise');
model.material('mat6').materialModel('def').func('eta').set('funcname', 'eta');
model.material('mat6').materialModel('def').func('eta').set('arg', 'T');
model.material('mat6').materialModel('def').func('eta').set('extrap', 'constant');
model.material('mat6').materialModel('def').func('eta').set('pieces', {'200.0' '1600.0' '-8.38278E-7+8.35717342E-8*T^1-
7.69429583E-11*T^2+4.6437266E-14*T^3-1.06585607E-17*T^4'});
model.material('mat6').materialModel('def').func.create('Cp', 'Piecewise');
model.material('mat6').materialModel('def').func('Cp').set('funcname', 'Cp');
model.material('mat6').materialModel('def').func('Cp').set('arg', 'T');
model.material('mat6').materialModel('def').func('Cp').set('extrap', 'constant');
model.material('mat6').materialModel('def').func('Cp').set('pieces', {'200.0' '1600.0' '1047.63657-
0.372589265*T^1+9.45304214E-4*T^2-6.02409443E-7*T^3+1.2858961E-10*T^4'});
model.material('mat6').materialModel('def').func.create('rho', 'Analytic');
model.material('mat6').materialModel('def').func('rho').set('funcname', 'rho');
model.material('mat6').materialModel('def').func('rho').set('args', {'pA' 'T'});
model.material('mat6').materialModel('def').func('rho').set('expr', 'pA*0.02897/8.314/T');
model.material('mat6').materialModel('def').func('rho').set('dermethod', 'manual');
model.material('mat6').materialModel('def').func('rho').set('argders', {'pA' 'd(pA*0.02897/8.314/T,pA)'; 'T'
'd(pA*0.02897/8.314/T,T)'});
model.material('mat6').materialModel('def').func.create('k', 'Piecewise');
model.material('mat6').materialModel('def').func('k').set('funcname', 'k');
model.material('mat6').materialModel('def').func('k').set('arg', 'T');
model.material('mat6').materialModel('def').func('k').set('extrap', 'constant');
model.material('mat6').materialModel('def').func('k').set('pieces', {'200.0' '1600.0' '-0.00227583562+1.15480022E-
4*T^1-7.90252856E-8*T^2+4.11702505E-11*T^3-7.43864331E-15*T^4'});
model.material('mat6').materialModel('def').func.create('cs', 'Analytic');
model.material('mat6').materialModel('def').func('cs').set('funcname', 'cs');
model.material('mat6').materialModel('def').func('cs').set('args', {'T'});
model.material('mat6').materialModel('def').func('cs').set('expr', 'sqrt(1.4*287*T)');
model.material('mat6').materialModel('def').func('cs').set('dermethod', 'manual');
model.material('mat6').materialModel('def').func('cs').set('argders', {'T' 'd(sqrt(1.4*287*T),T)'});
model.material('mat6').materialModel('def').addInput('temperature');
model.material('mat6').materialModel('def').addInput('pressure');
model.material('mat6').materialModel('def').set('relpermittivity', {'1e-5'});
model.material('mat6').selection.set(air_a_domains);


%-------------------- physics settings -----------------------------------

model.physics('es').feature.create('pot1', 'ElectricPotential', 1);
model.physics('es').feature('pot1').set('V0', 1, '1');
model.physics('es').feature('pot1').selection.set(source_boundaries);
```

```
model.physics('es').feature.create('gnd1', 'Ground', 1);
model.physics('es').feature('gnd1').selection.set(grounding_boundaries);

model.physics('es').feature.create('gnd2', 'Ground', 1);
model.physics('es').feature('gnd2').selection.set(gr_boundaries);

model.physics('es').feature.create('gnd3', 'Ground', 1);
model.physics('es').feature('gnd3').selection.set(elec_e_boundaries);

model.physics('es').feature.create('gnd4', 'Ground', 1);
model.physics('es').feature('gnd4').selection.set(elec_s_boundaries);

% model.physics('es').feature.create('gnd5', 'Ground', 1);
% model.physics('es').feature('gnd5').selection.set(sht_top_boundaries);


%----------------- meshing settings ------------------------------------

mesh1=model.mesh.create('mesh1', 'geom1');

model.mesh('mesh1').feature.create('ftri1', 'FreeTri');
model.mesh('mesh1').feature('ftri1').selection.geom('geom1', 2);
model.mesh('mesh1').feature('ftri1').selection.set(air_3_domains);
model.mesh('mesh1').feature('ftri1').feature.create('size1', 'Size');
model.mesh('mesh1').feature('ftri1').feature('size1').set('custom', 'on');
model.mesh('mesh1').feature('ftri1').feature('size1').set('hmaxactive', 'on');
model.mesh('mesh1').feature('ftri1').feature('size1').set('hmax', '1');
model.mesh('mesh1').feature('ftri1').feature('size1').set('hminactive', 'on');
model.mesh('mesh1').feature('ftri1').feature('size1').set('hmin', '0.1');
model.mesh('mesh1').feature('ftri1').feature('size1').set('hgradactive', 'on');
model.mesh('mesh1').feature('ftri1').feature('size1').set('hgrad', '1.3');

model.mesh('mesh1').feature.create('ftri2', 'FreeTri');
model.mesh('mesh1').feature('ftri2').selection.geom('geom1', 2);
model.mesh('mesh1').feature('ftri2').selection.set([gold_domains si_domains]);
model.mesh('mesh1').feature('ftri2').feature.create('size1', 'Size');
model.mesh('mesh1').feature('ftri2').feature('size1').set('custom', 'on');
model.mesh('mesh1').feature('ftri2').feature('size1').set('hmaxactive', 'on');
model.mesh('mesh1').feature('ftri2').feature('size1').set('hmax', '1');
model.mesh('mesh1').feature('ftri2').feature('size1').set('hminactive', 'on');
model.mesh('mesh1').feature('ftri2').feature('size1').set('hmin', '0.1');
model.mesh('mesh1').feature('ftri2').feature('size1').set('hgradactive', 'on');
model.mesh('mesh1').feature('ftri2').feature('size1').set('hgrad', '1.3');

model.mesh('mesh1').feature.create('ftri3', 'FreeTri');
model.mesh('mesh1').feature('ftri3').selection.geom('geom1', 2);
model.mesh('mesh1').feature('ftri3').selection.set([air_1_domains pyrex_domains]);
model.mesh('mesh1').feature('ftri3').feature.create('size1', 'Size');
model.mesh('mesh1').feature('ftri3').feature('size1').set('custom', 'on');
model.mesh('mesh1').feature('ftri3').feature('size1').set('hmaxactive', 'on');
model.mesh('mesh1').feature('ftri3').feature('size1').set('hmax', '5');
model.mesh('mesh1').feature('ftri3').feature('size1').set('hminactive', 'on');
model.mesh('mesh1').feature('ftri3').feature('size1').set('hmin', '0.5');
model.mesh('mesh1').feature('ftri3').feature('size1').set('hgradactive', 'on');
model.mesh('mesh1').feature('ftri3').feature('size1').set('hgrad', '2');

model.mesh('mesh1').feature.create('ref1', 'Refine');
model.mesh('mesh1').feature('ref1').set('boxcoord', 'on');
model.mesh('mesh1').feature('ref1').set('xmin', '-595');
model.mesh('mesh1').feature('ref1').set('xmax', '595');
model.mesh('mesh1').feature('ref1').set('ymin' , -gap-elec_thick-5);
model.mesh('mesh1').feature('ref1').set('ymax', sht_thick+10);
```

```
model.mesh('mesh1').feature('ref1').set('numrefine', '3');

model.mesh('mesh1').feature.create('ftri4', 'FreeTri');
model.mesh('mesh1').feature('ftri4').selection.geom('geom1', 2);
model.mesh('mesh1').feature('ftri4').selection.set(air_a_domains);
model.mesh('mesh1').feature('ftri4').feature.create('size1', 'Size');
model.mesh('mesh1').feature('ftri4').feature('size1').set('hauto', '3');

model.mesh('mesh1').run;


%-------------------- study settings ----------------------------------

model.sol('sol1').study('std1');
model.sol('sol1').feature.create('st1', 'StudyStep');
model.sol('sol1').feature('st1').set('study', 'std1');
model.sol('sol1').feature('st1').set('studystep', 'stat');
model.sol('sol1').feature.create('v1', 'Variables');
model.sol('sol1').feature.create('s1', 'Stationary');
model.sol('sol1').feature('s1').feature.create('fc1', 'FullyCoupled');
model.sol('sol1').feature('s1').feature.remove('fcDef');
model.sol('sol1').attach('std1');
model.sol('sol1').runAll;

%------------------------- save data ------------------------------------

[IC1 unit]=mphint(model,'es.nD','edim',1,'selection', [elec_e_boundaries]);
[IC2 unit]=mphint(model,'es.nD','edim',1,'selection', [elec_s_boundaries]);
IC_d=(IC1-IC2)*1e20;

Dfs(i,1:10)=[slit_wid, sht_thick, elec_wid, gr_wid, gap, bn, iso, IC1*1e20, IC2*1e20, IC_d];

save sim2d_march_2012_fs Dfs;

%-------------------- clear structure ----------------------------------

    model.param.remove('bn');
    model.param.remove('sn');
    model.mesh.remove('mesh1');
    sol.feature.remove('st1');
    sol.feature.remove('v1');
    sol.feature.remove('s1');
    model.geom.remove('geom1');
    model.physics.remove('es');
    std.feature.remove('stat');
    IC1=0;
    IC2=0;
    IC_d=0;
    step=i;
    clear model;

end
```

4. GeomAnalyze

```
function [domains boundaries boundariescrd interiorBoundaries] = geomAnalyze(geom)

    objects = geom.objectNames();


    objCoords = zeros(objects.length,2);
    for i=1:objects.length
```

```
    obj = geom.object(objects(i));
        coords = obj.getVertexCoord;

    firstCoord = coords(:,1);
    for j=2:length(coords)
      if coords(1,j) < firstCoord(1) || (coords(1,j) == firstCoord(1) && coords(2,j) < firstCoord(2))
        firstCoord = coords(:,j);
      end
    end
    objCoords(i,1)= firstCoord(1);
    objCoords(i,2)= firstCoord(2);

  end

  taken = zeros(1,objects.length);
  clear domains;
  for k=1:objects.length

    selectedCoord = 0;
    selectedIndex = 0;
    for i=1:length(objCoords)
      if taken(i)==0
        if selectedIndex == 0 || objCoords(i,1) < selectedCoord(1) || (objCoords(i,1) == selectedCoord(1) &&
objCoords(i,2) < selectedCoord(2))
          selectedCoord = objCoords(i,:);
          selectedIndex = i;
        end
      end
    end

    taken(selectedIndex) = 1;
    domains(k) = objects(selectedIndex);
  end

  clear boundaryCoords boundaries; k=1;
  for i=1:domains.length
    obj = geom.object(domains(i));
        edges = obj.getEdge;
    edges = edges(1:2,:);
    vertices = obj.getVertex;

    for j = 1:length(edges)
        boundaryCoords(1,k) = vertices(1,edges(1,j)); %coords of the start point of the edge
        boundaryCoords(2,k) = vertices(2,edges(1,j));
        boundaryCoords(3,k) = vertices(1,edges(2,j)); %coords of the end point of the edge
        boundaryCoords(4,k) = vertices(2,edges(2,j));
        boundaryCoords(5,k) = i;            %the domain the edge belongs to
        k=k+1;                    % k is the index of the edge
    end
  end

  a=geom.feature.create('all','Union');
  a.selection('input').set( geom.objectNames) ;
  a.set('keep','on');
  geom.run;


  finalEdges = geom.object('all').getEdge;
  finalVertices = geom.object('all').getVertex;

  interiorBoundaries = zeros(1,length(finalEdges));
  boundariescrd=zeros(length(finalEdges),4);
```

```
    for i=1:length(finalEdges)
        k=0;
            vertA = finalVertices(1:2, finalEdges(1,i) );
        vertB = finalVertices(1:2, finalEdges(2,i) );
        vertA = round(vertA.*10^10)./10^10;
        vertB = round(vertB.*10^10)./10^10;

        boundaryCoords = round(boundaryCoords.*10^10)./10^10;

        interior = 0;
        Candidate = [];

boundariescrd(i,:)=[finalVertices(1,finalEdges(1,i)),finalVertices(2,finalEdges(1,i)),finalVertices(1,
finalEdges(2,i)),finalVertices(2, finalEdges(2,i))];
        likelyPerc = 0;


        for j=1:length(boundaryCoords)
            ol =
overlapLength([boundaryCoords(1,j),boundaryCoords(2,j)],[boundaryCoords(3,j),boundaryCoords(4,j)],[vertA(1),vert
A(2)],[vertB(1),vertB(2)]);
            if ol ~= 0
                k=k+1;
                interior = (likelyPerc > 0);
                        likelyPerc=ol;
                            Candidate(k,1)=j;
                    Candidate(k,2)=likelyPerc;

                        end

        end



        if (Candidate(1,1) == 0)
            fprintf('couldnt find boundary for %d\n',i);
        else
                for sp = 1:k
            boundaries{i,2*sp-1}= domains( boundaryCoords(5,Candidate(sp,1)) );
            boundaries{i,2*sp} = Candidate(sp,2);
           end



            if (interior ~= 0)
                interiorBoundaries(i) = 1;
            end
        end
    end
    geom.feature().remove('all');
    geom.run;

    end
```

5. overlapLength

```
function ol=overlapLength(x1,y1,x2,y2)

    ol=0;
%     if length(x1) == 1
%
```

```
%         max1 = max(x1,y1);
%         min1 = min(x1,y1);
%         max2 = max(x2,y2);
%         min2 = min(x2,y2);
%
%         if (min1 >= max2) || (min2 >= max1)  %case1
%             l=0;
%         elseif (max2 > min1 && min1 > min2) %case2
%             l= max2-min1;
%         elseif max2 > min1 && min2 >= min1 && max2 <= max1 %case4
%             l = max2 - min2;
%         elseif max1 > min2 && min1 >= min2 && max1 <= max2 % case5
%             l= max1-min1;
%         elseif max2 >= max1 && min1 < min2 %case3
%             l = max1 - min2;
%         end
%
%         return;
%
%     else
%
%         if x1(1) == x1(2) && x2(1) == x2(2) && x1(1) == x2(1)
%             l=overlapLength(y1(1),y1(2),y2(1),y2(2));
%             return;
%         elseif y1(1) == y1(2) && y2(1) == y2(2) && y1(1) == y2(1)
%             l=overlapLength(x1(1),x1(2),x2(1),x2(2));
%             return;
%         elseif x1(1) ~= x1(2) && x2(1) ~= x2(2)
%
%             m(1) = (y1(2)-y1(1))/(x1(2)-x1(1));
%             b(1) = y1(1) - m(1)*x1(1);
%             m(2) = (y1(2)-y1(1))/(x1(2)-x1(1));
%             b(2) = y2(1) - m(2)*x2(1);
%
%             m= round(m.*10^7)./10^7;
%             b= round(b.*10^7)./10^7;
%
%
%             if (m(1) == m(2) && b(1) == b(2))
%
%                 x0 = -b(1)/m(1);
%
%                 hyp1(1) = sqrt( y1(1)^2 + (x1(1)-x0)^2);
%                 hyp1(2) = sqrt( y1(2)^2 + (x1(2)-x0)^2);
%                 hyp2(1) = sqrt( y2(1)^2 + (x2(1)-x0)^2);
%                 hyp2(2) = sqrt( y2(2)^2 + (x2(2)-x0)^2);
%
%                 l = overlapLength(hyp1(1),hyp1(2),hyp2(1),hyp2(2));
%                 return;
%             end
%         end
%
%
%     end

if x1(1)==x2(1) && x1(2)==x2(2) && y1(1)==y2(1) && y1(2)==y2(2)
    ol=1;

return;

else
    k1=(y1(2)-x1(2))/(y1(1)-x1(1));
```

```
    k2=(y2(2)-x2(2))/(y2(1)-x2(1));
    k3=(y2(2)-x1(2))/(y2(1)-x1(1));
    k4=(y1(2)-x2(2))/(y1(1)-x2(1));
    d1=sqrt((y1(2)-x1(2))^2+(y1(1)-x1(1))^2);
    d2=sqrt((y2(2)-x2(2))^2+(y2(1)-x2(1))^2);
    d3=sqrt(((y1(1)+x1(1))/2-(y2(1)+x2(1))/2)^2+((y1(2)+x1(2))/2-((y2(2)+x2(2))/2))^2);


    if k1==k2 && k2==k3 && k3==k1 && k4==k1

        if d3 < (d1+d2)/2
                ol = min(d1,d2)/max(d1,d2);
        elseif d3 >= (d1+d2)/2
                ol = 0;
        end
    else
            ol = 0;
    end

end
end
```

6. findStr

```
function x = findStr(str, list)

    x=[]; k=1;
    for i=1:length(list)
        if strncmp(str,list(i),length(str))==1;
            x(k)=i;
            k=k+1;
        end

    end

end
```

7. findStrc

```
function x = findStrc(str, cell, p)

    x=[]; k=1;
    for i=1:size(cell,1)
        for j=1:size(cell,2)
        if (strncmp(str,cell{i,j},length(str))==1)&& (cell{i,j+1}==p)
            x(k)=i;
            k=k+1;
        end
        end
    end
end
```

Appendix B: Plasma Etch Attempts

Etch #	1	2	3	4	5	6	7	8	9	10	11	12
Pressure (mTorr)	50	50	50	50	50	50	100	100	50	50	50	50
RIE (W)	75	75	50	50	50	50	50	50	100	50	50	70
ICP (W)	100	100	100	100	100	100	100	100	100	100	100	300
Time (s)	600	600	600	600	600	600	600	600	600	600	600	600
CF_4 (sccm)	0	0	0	0	0	45	0	0	45	0	0	45
SF_6 (sccm)	30	30	30	30	30	0	30	30	0	30	30	0
O_2 (sccm)	15	15	15	15	0	5	15	15	5	15	15	5
CHF_3(sccm)	0	10	0	10	0	0	10	20	0	15	20	0
Depth (μm)	9.56	15.16	6.58	7.83	16.06	1.128	6.528	8.458	1.795	14.35	15.45	3.965
Etch-rate (μm/min)	0.956	1.516	0.658	0.783	1.606	0.1128	0.6528	0.8458	0.1795	1.435	1.545	0.3965
In Table 3-1												
W_{mask} (μm)	16	22	14	14	9	8	6	14	6	7	8	6
undercut	0	0	0	0	72%	44%	46%	24%	84%	17%	26%	63%
W_{bottom} (μm)	4	2	5	4			4	12		6	4	
slope angle	58°	51°	56°	57°			58°	71°		78	68°	
anisotropy	0.37	0.34	0.32	0.36			0.39	0.66		0.79	0.61	
Other Data, not in Table 3-1												
W_{mask} (μm)	12	15	14	15	26	8	5.5	7	7	8	6	9
undercut	0	0	0	0	53%	133%	11%	29%	84%	21%	32%	63%
W_{bottom} (μm)	~1	~0	6	5			0	6		6	4	
slope angle	58°	N/A	56°	57°			N/A	71°		74°	68°	
anisotropy	0.37	N/A	0.39	0.36			N/A	0.66		0.71	0.61	
W_{mask} (μm)	12	17	14	23		9	7	8	7.5	11	13.5	
undercut	0	0	0	3%		89%	46%	24%	70%	21%	40%	
W_{bottom} (μm)	~1	~1	~4	12			5	6		10	14	
slope angle	54°	51°	53°	55°			58°	71°		76°	68°	
anisotropy	0.37	0.34	0.24	0.32			0.39	0.66		0.75	0.61	
W_{mask} (μm)	17	20	22	29		10	10	26	10.5	14	24	
undercut	0.25	0	0	3%		44%	46%	23%	70%	21%	32%	
W_{bottom} (μm)	~5	~1	12	17			7	22		12	22	
slope angle	58°	51°	53°	53°			55°	65°		74°	68°	
anisotropy	0.37	0.34	0.24	0.24			0.35	0.53		0.71	0.61	
W_{mask} (μm)	32	20	32	34		12	11			22		
undercut	0	0	0	0		89%	38%			24%		
W_{bottom} (μm)	18	~1	22	22			7			20		
slope angle	54°	51°	53°	53°			55°			72°		
anisotropy	0.37	0.34	0.24	0.24			0.35			0.66		
W_{mask} (μm)	36	22				16.5	15			24		
undercut	3%	0				89%	38%			31%		
W_{bottom} (μm)	22	2					11			24		
slope angle	54°	51°					55°			72°		
anisotropy	0.37	0.34					0.35			0.66		
W_{mask} (μm)										26		
undercut										28%		
W_{bottom} (μm)										25		
slope angle										72°		
anisotropy										0.66		

Appendix C: Measurements of Motion Test on Sensors Fabricated Through PolyMUMPs

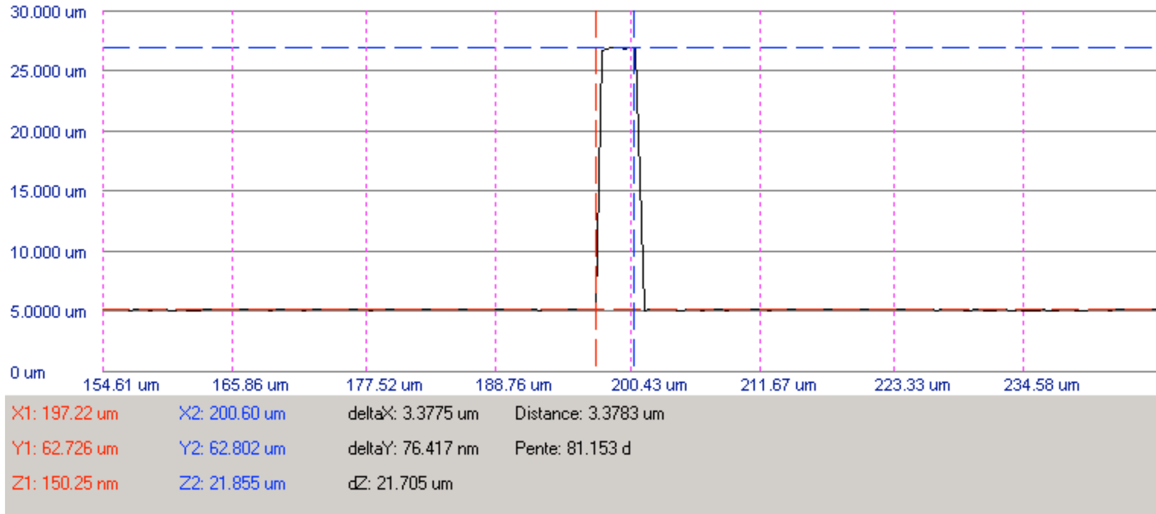

(a) Measurement of the connecting beam with actuator unbiased.

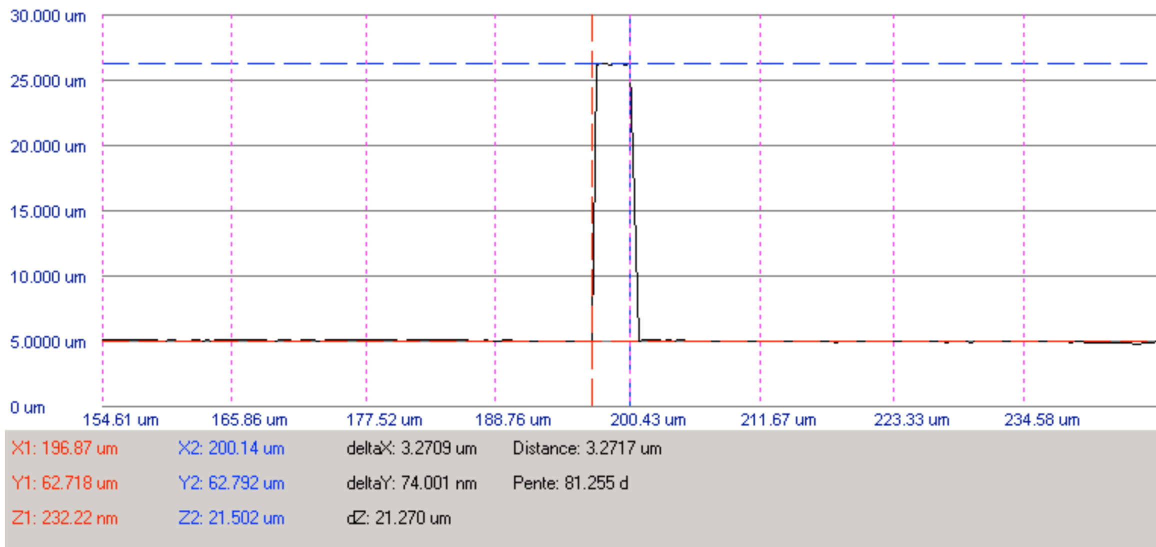

(b) Measurement of the connecting beam with actuator biased.

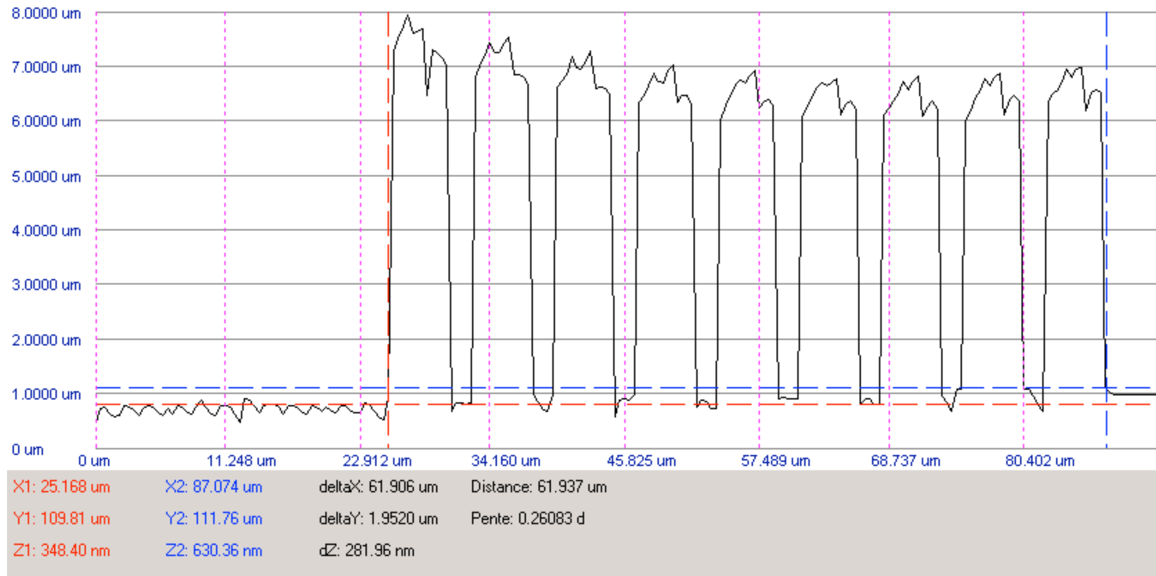

(a) Measurement of the thermal actuator when unbiased.

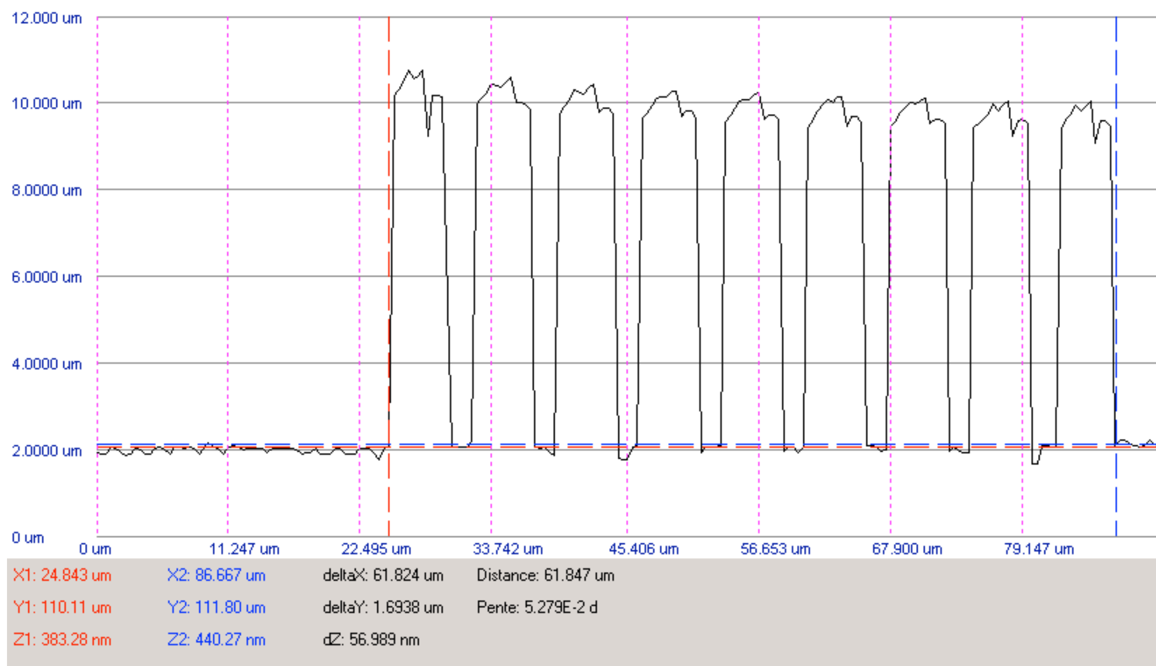

(b) Measurement of the thermal when biased.